



Department of Chemistry and Catalysis Research Center
Chair of Technical Electrochemistry

Towards the Scalable Synthesis of PGM-free Catalysts for Oxygen Reduction Reaction

Burak Koyutürk

Vollständiger Abdruck der von der Fakultät für Chemie der Technischen Universität München zur Erlangung des akademischen Grades eines

Doktors der Naturwissenschaften (Dr. rer. nat.)

genehmigten Dissertation.

Vorsitzende(r): Prof. Dr. Tom Nilges

Prüfer der Dissertation:

1. Prof. Dr. Hubert A. Gasteiger
2. Prof. Dr. Klaus Köhler

Diese Dissertation wurde am 12.08.2020 bei der Technischen Universität München eingereicht und durch die Fakultät für Chemie am 03.09.2020 angenommen.

Abstract

The commercialization of fuel cells depends upon the developments in the components of fuel cells stacks, particularly the cathode catalyst which has a major contribution to both the performance and the cost of the stack. In this thesis, the replacement of the conventional fuel cell cathode catalyst, Pt, with platinum-group-free catalyst was targeted in two aspects. First, the test of a novel synthesis method, *Active Site Imprinting*, was transferred to a scalable material. The structure-activity relationship was shown using both surface-sensitive and bulk characterization methods as well as imaging techniques. The activity was tested in both thin film rotating disk and 5 cm² single cell. Test results showed that high activity towards oxygen reduction reaction was achieved with *Active Site Imprinting* method. Second, the adaptation of chemical activation process to conductive carbon synthesis was investigated. The mechanistic study revealed the resemblance of a commercial chemical activation process to sol-gel type process particularly at high solvent content. This finding provides a higher degree of control on porosity developments during the synthesis of carbons. Furthermore, the high temperature synthesis carried out by employing H₃PO₄, taking the advantage of the results obtained from mechanistic study. The synthesis yielded to hierarchical pore structure and N-P doped conductive carbons. The metal-free synthesis opens a new path for the future synthesis of inexpensive platinum-metal-group free (PGM-free) catalysts and conductive supports.

Die Kommerzialisierung von Brennstoffzellen ist von der Entwicklung einzelner Komponenten sogenannter Brennstoffzellenstapel abhängig. Von besonderer Relevanz sind die Kosten des Kathodenkatalysators, der einen wesentlichen Beitrag zu der Leistungsfähigkeit des Stapels hat. In dieser Arbeit wurde der Ersatz des herkömmlichen Brennstoffzellenkathodenkatalysators Pt durch einen platingruppenfreien Katalysator in zweierlei Hinsicht angestrebt. Zunächst wurde eine neuartige Synthesemethode, die sogenannte „Active Site Imprinting-Methode“, auf ein größerskalig herstellbares Material übertragen. Die Struktur-Aktivitäts-Relation wurde sowohl unter Verwendung von kombinierten oberflächensensitiven und Bulk-Methoden, als auch unter Verwendung von Bildgebungstechniken untersucht. Die katalytische Aktivität wurde sowohl in einer rotierenden Scheibenelektrode, als auch in einer 5 cm² großen Brennstoffzellen-Einzelzelle getestet. Die Testergebnisse zeigten, dass mit der Active Site Imprinting-Methode eine hohe Aktivität in der Sauerstoffreduktionsreaktion erreicht wurde. Zweitens wurde die Modifikation eines kommerziellen Verfahrens zur Herstellung von Aktivkohle hin zu Herstellung von leitfähigen Kohlenstoffmaterialien untersucht. Die mechanistische Studie ergab die Äquivalenz des kommerziellen Verfahrens zu dem sogenannten Sol-Gel-Verfahren, insbesondere bei Einsatz eines hohen Lösungsmittelgehalts. Diese Einsicht ermöglicht ein höheres Maß an Kontrolle in der Generierung von Porosität, während der Synthese von Kohlenstoffen. Darüber hinaus wurde die Hochtemperatursynthese unter Verwendung von H₃PO₄ durchgeführt, wobei die Erkenntnisse der mechanistischen Untersuchung genutzt wurden. Die Synthese ergab eine hierarchische Porenstruktur und N-P-dotierte leitfähige Kohlenstoffe. Die metallfreie Synthese eröffnet einen neuen Weg für die zukünftige Synthese kostengünstiger platingruppenfreier Katalysatoren und leitfähiger Trägermaterialien.

Acknowledgments

I would like to thank, first of all, my supervisor Dr. Tim-Patrick Fellingner for giving me this opportunity and guiding me during my PhD. His continuous support and experiences helped me not only in chemistry but also in the other parts of academic life, which I am sure that I will run into in the future.

I am grateful to meet Prof. Dr. Hubert Gasteiger, taking his lectures, learning electrochemistry from him and I would like to thank him for changing my opinion about science. I was inspired by his experience and passion towards working and learning. I would also like to thank for hosting our group at TEC and incredible generosity.

I would like to thank Prof. Piotr Zelenay for hosting me in his group at Los Alamos National Laboratory and his support and hospitality from the beginning of my stay to the last day.

I have felt many supports from many people during my PhD. I would like to start with Davide Menga who I started my PhD with. Thanks to his friendship and joy of living, the hard times of PhD became less effective. Ceren, Mohammad and Yan-Sheng are acknowledged for being with me all the time, sharing this beautiful experience at TEC right next to me. I would like to thank also Alex, Anne, Paulette, Long, Nicole, Anna Freiberg, Michele, Timon, Leonardo and Heiko for being more than a colleague to me and not refraining their support. I would like to mention some former members' names here, Gregor, Maximillian, Pankaj and Daniel for their efforts for the group. I believe that being a group is not only working together but also putting effort to help each other. Also, Bianca, Siddarth and Ulises from Los Alamos National Laboratory are acknowledged for sharing their experiences with me and helping me during my stay at LANL.

My friends from my master study; iğdem, Pelin, İlknur, Vahid, Özge Akarçay and Benay are acknowledged as I always felt their support from thousands of kilometers away. Also, Tolga, Ahmet, Kutay, Burak, Hasan, Mert and Muslum are greatly acknowledged for their supports and understanding. I may have missed some of the important moments in last three years but they always tolerated my absence.

I would like to thank my father and sister for their patience in last 3 years. I am aware that they did not reflect their own problems and hid most of the times as they wanted me to focus.

Lastly, I would like to thank my girlfriend, Melike. You have always motivated me since the day we met, shared your experience and your time.

Contents

Abstract.....	VI
Acknowledgments.....	VIII
List of Acronyms	VII
1. Motivation and Background	1
1.1 Oxygen Reduction Electrochemistry	3
1.2 Scalable Synthesis of PGM-free Catalysts	6
1.3 PGM-free ORR Electrocatalysts	11
2. Active Site Imprinting Method.....	15
2.1 Introduction	15
2.2 Scalable and Highly Active PGM-free Catalysts	17
3. Heteroatom Doped Porous Carbons	37
3.1 Introduction	37
3.1.1 Sol-Gel Process	38
3.2 Results	40
3.2.1. Porosity Development with Brønsted acids	40
3.2.2. High Temperature Synthesis	53
4. Conclusion.....	71
5. Outlook	73
6. Experimental Methods.....	75
6.1 Synthesis of the Materials	75
6.2 Characterization Techniques	77
7. Bibliography	81
Appendix.....	93

List of Acronyms

Abbreviation	Description
AFCs	Alkaline Fuel Cells
AC	Activated Carbon
AR-STEM	Atomic Resolution Scanning Transmission Electron Microscopy
BET	Brunauer – Emmett – Teller
BEVs	Battery electric vehicles
CE	Counter electrode
CV	Cyclic Voltammetry
FCEVs	Fuel cell electric vehicles
HOR	Hydrogen oxidation reaction
HFR	High Frequency Resistance
HRSEM	High Resolution Scanning Electron Microscope
HRTEM	High Resolution Transmission Electron Microscopy
IL	Ionic Liquid
LSV	Linear Scanning Voltammetry

Mg-DA	Magnesium iminodiacetic acid
MEA	Membrane Electrode Assembly
MOCP	Magnesium based metal-organic coordination polymer
MOFs	Metal organic frameworks
OCV	Open circuit voltage
ORR	Oxygen reduction reaction
PANI	Polyaniline
PEMFCs	Proton Exchange Membrane Fuel Cells
PGM-free	Platinum-metal-group-free
PSD	Pore Size Distribution
PTFE	Polytetrafluoroethylene
PXRD	Powder X-ray Diffraction
QSDFT	Quenched Solid Density Functional Theory
RDE	Rotating Disc Electrode
RE	Reference electrode
SEM	Scanning Electron Microscopy
SHE	Standard Hydrogen Electrode
S_{meso}	Mesopore surface area

S_{micro}	Micropore surface area
SSA	Specific surface area
TEM	Transmission Electron Microscopy
TG-MS	Thermogravimetric analysis coupled by mass spectrometer
TPV	Total pore volume
UCC	Union Carbide Corporation
WE	Working electrode
XPS	X-ray Photoelectron Spectroscopy
ZIF-8	Zeolitic Imidazolate Framework-8

1. Motivation and Background

The accumulation of the greenhouse gases in the atmosphere has been increasing drastically since the beginning of industrialization. The growing population increased the emission of these gases and the concentration in the atmosphere from 280 to 380 ppmv (part per million volume) from 1800s to 2007.¹ Although there are a number of contributors to greenhouse gases, the transportation and electricity production were reported to have the biggest share of CO₂ emission in 2017 with more than 70% of total global emission.² Therefore, the adaption of the clean technologies became crucial particularly in transportation and electricity generation.

Proton Exchange Membrane Fuel Cells (PEMFCs) were nominated as one of the best candidates as a replacement of combustion engines due to the clean working principle together with batteries. The reaction of hydrogen with air (oxygen) results in formation of water as product whereas burning fossil fuels causes formation of carbon dioxide, carbon monoxide etc. thus, increasing the greenhouse gas effects in the atmosphere. Recently, fuel cell electric vehicles (FCEVs) have become popular in mobility not only because of cleanliness but also their solution to fast fueling and long range driving compared to battery electric vehicles (BEVs). Today, the commercial FCEVs have approximately refueling time < 5 min and driving range > 590 km.³ However, the transition from diesel/gasoline to fuel cell in the transportation is still an ongoing process, which reflects to the sales of the biggest companies in this field. For instance, Toyota Mirai sales in last 5 years indicate an average number of 4 vehicles sold per day.⁴ While the private industry is struggling with the commercialization, the adaptation of public transportation, especially buses, is supported by European and government funded projects. One case study in London for fuel cell buses discloses the milestone of 30,000 hours of continuous operation of eight buses without replacement or repairs.⁵

Despite the remarkable technical advantages gained recently and the attempts for the adoption of FCEVs in the transportation, further commercialization is limited due to high cost of FCEVs and low abundance of the catalyst which is at the core of the fuel cell stack as well as design of the other components of the FCEVs and infrastructure of fueling stations. A cost analysis reveals that almost the half of the system cost is originated from the fuel cell stack in which the catalyst (Pt) makes up 41% of the stack cost.⁶ Therefore, reduction or completely replacement of Pt plays a significant role for the future of FCEVs. The reduction of Pt amount can be accomplished by improving the activity of the catalysts, thus operating the stack with less Pt, whereas replacement of Pt is projected by using platinum-metal-group-free (PGM-free) catalysts.

Apart from the transportation, the electricity generation strategies are changing due to a heavy impact of fossil fuel-based electricity. Beside a number of consequences of fossil fuels including health problems, agricultural damage etc., only the environmental damage cost caused by fossil fired power plants in EU-15 countries amount to 70 billion \$ in 1990.⁷ This impact changes the direction of the countries for electricity generation. For instance, Germany targets a share of electricity from renewable sources of at least 80% in 2050 and develops strategies accordingly.⁸ At this juncture, hydrogen energy becomes a core argument especially in the summits organized for highly industrialized countries to reach these targets.¹

Alkaline fuel cells (AFCs) are promising solutions especially for stationary energy applications. AFCs have big advantages in terms of operational conditions such as low temperature operation and long operation life.⁹ AFCs also yield the highest voltage of all the fuel cell systems. However, the biggest advantage might be considered as the wide range of catalyst that can be used in the stack. Unlike, PEMFCs, AFC stacks are not limited to platinum group metals.

PGM-free catalysts are considered as one of the best candidates for replacement of Pt in the fuel cell stack due to the recent improvements in this field. Today, small portable devices with PGM-free catalysts are being produced, however for the automotive applications further criteria must be fulfilled. At this juncture, the catalyst must meet the feasibility and scalability criteria for the future applicability which will be covered in Chapter 1 of this thesis. Moreover, the activity improvement is still needed due to the limitations regarding the volume of the catalyst layer. As more active sites (higher loading) lead to bigger volume, this problem was often addressed by increasing the active site density of the catalyst, thus obtaining the same activity with less catalyst. A promising approach, ‘novel active site imprinting method’¹⁰ from scalable perspective will be discussed in Chapter 2.

1.1 Oxygen Reduction Electrochemistry

The conversion of the energy stored in the molecules to electrical energy simply follows the thermodynamics. In the case of oxygen reduction reaction (ORR), Gibbs free energy change of the reaction, $\Delta_R G$, is the maximum energy that can be obtained as electrical energy. In H₂/O₂ fuel cell, $\Delta_R G$ can be calculated using the formation energies of H₂O, H₂ and O₂ as shown in *Equation 1*.

$$\Delta_R G = \Delta_f G_{H_2O} - [\Delta_f G_{H_2} + 0.5 \times \Delta_f G_{O_2}] \quad \text{Equation 1}$$

$\Delta_R G$ is directly related to reversible potential as described in *Equation 2*. The direct reduction of oxygen to water has reversible potential of 1.23 V (T=25 °C, p(H₂)=101 kPa, p(O₂)=101 kPa) which is a function of temperature and activity (concentration) of oxidized and reduced species

in the reaction. Also, the thermodynamic efficiency for H₂/O₂ fuel cell is notably high (83%) indicating a big advantage of fuel cells apart from clean energy. However, this simple theory turns into cat’s cradle when it comes to practice as voltage losses occur during the operation (Figure 1.1.2).

$$E_{rev} = -\frac{\Delta_{RG}}{nxF} \quad \text{Equation 2}$$

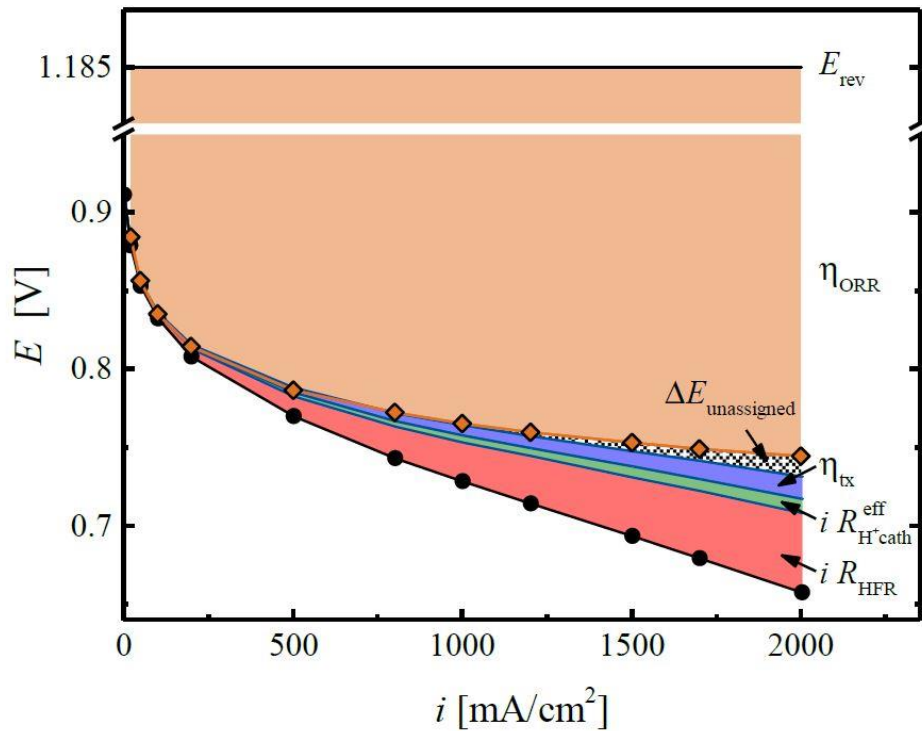


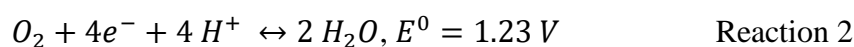
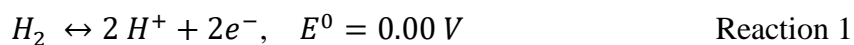
Figure 1.1.2: Origin of the voltage losses in fuel cell stack.¹¹

The overall cell voltage (E_{cell}) can be calculated taking into all voltage losses into account as indicated in *Equation 3*. Improving the cell voltage can be achieved by reduction of these losses originated from such as resistance of membrane and contact of fuel cell components ($R_{membrane}$, $R_{contact}$), overpotentials for hydrogen oxidation reaction (HOR) and (ORR) (η_{HOR} , η_{ORR}),

resistance of proton transport in the catalyst layer ($R_{H^+, cath}$) and transport of reactants through the catalyst layer to the active sites (η_{tx}).

$$E_{cell} = E_{rev} - i (R_{membrane} + R_{contact}) - \eta_{HOR} - |\eta_{ORR}| - i (R_{H^+, cath}^{eff}) - \eta_{tx} \quad \text{Equation 3}$$

$R_{membrane}$ and $R_{contact}$ are caused by fuel cell components such as membrane, gas diffusion layers and flow fields which mainly play an important role at high current density as the contribution of these terms to total loss is calculated by multiplying by current ($i (R_{membrane} + R_{contact})$). HOR on the anode side of FC is a fast reaction while ORR is much more sluggish. HOR in the anode follows Reaction 1 and brings about negligible voltage loss even at high current density (~ 12 mV loss at 0.93 A/cm²)¹² while ORR is considered as a big burden due to high overpotential and kinetic losses. The sluggish kinetics and high over potential for ORR can be overcome using more active catalysts in the cathode compartment. Volcano plot found based on Sabatier Principle reveals platinum as the most active element for ORR.¹³ However, the limitations mentioned earlier motivates to search for an alternative catalysts such as PGM-free catalysts. $R_{H^+, cath}$ is originated from the transport of protons in the cathode catalyst layer and η_{tx} is the transport of mainly O_2 in the cathode which can be reduced by modification of some intrinsic properties of the catalyst such as porosity, particle size and morphology.



The ORR activities of the catalysts can be tested by different setups using the same electrochemical principle. Thin film Rotating Disc Electrode (RDE) is the most common setup that is used for the screening of the activity of the catalysts with small amounts (microgram

scale). A regular RDE setup is depicted in Figure S1.1.1. The setup consists of working electrode (WE), reference electrode (RE) and counter electrode (CE). As oxygen reduction takes place in cathode, WE can be considered as cathode and the potential is applied to WE with respect to RE. The most common reference electrodes are standard hydrogen electrode (SHE), calomel and silver/silver chloride. CE is employed in order to close the electrical circuit, thus electrically conductive and chemically stable (in respective electrolyte) electrode is needed. While the ionic conductivity is provided by conductive electrolyte (ionically conductive and electronically non-conductive), the electrons flow through an external circuit. In this thesis, two different cells were used to acquire the electrochemical data for acidic and alkaline media and the equipment and the chemicals were given in Chapter 6.2.

The activity can also be tested in fuel cell test station that has closer conditions to the real application. The electrodes can be fabricated via various routes based on the coating of the ink on different substrates and as expected higher amount of catalyst is needed for fuel cell tests (mg scale). The electrodes (cathode and anode) and membrane are used to prepare membrane electrode assembly (MEA). The membranes are usually made of perfluorinated polymers containing ionic groups. MEA is combined with the other components of the stack such as gas diffusion layers and bipolar plates and subjected to test in fuel cell test station. An illustration of fuel cell stack can be seen in Figure S1.1.2.

1.2 Scalable Synthesis of PGM-free Catalysts

As the transition in the electrical mobility requires mass production of fuel cell components such as bipolar plates, membranes, gas diffusion layers etc., the contribution of the catalyst to

the total fuel cell stack cost is expected to increase. An increase in the production volume of fuel cell stacks from 1,000 to 500,000 units/year causes rise in the share of catalyst cost in the total cost from 21% to 41%.¹⁴ Therefore, catalyst production becomes more important with increasing market volume of fuel cells.

In PGM-free case, the catalyst production differs from Pt catalysts as the PGM-free catalysts are often synthesized from carbon, nitrogen and metal precursors. Thus, a comprehensive industry and scalable process are necessary for mass production of PGM-free catalysts. Today, the most important manufacturer of PGM-free catalysts, Nisshinbo (Japan) has very complicated synthesis method with multistep heat treatments, acidic work up and ball milling steps for the synthesis of their PGM-free catalysts “carbon alloy”.¹⁵ In fact, Nisshinbo supplies catalysts to Ballard Power Systems for the production of portable fuel cell stacks (FCgen-stacks) as a global supplier of carbon plates for fuel cell stacks.¹⁶ For low power systems such as 30-40 W portable items, this synthesis method is still manageable to provide materials in gram scale. Another company, Pajarito Powder (USA) has again sales in the scale of grams (5-10 g). However, even during the transition state, especially for the manufacturing of FCEVs, the global market will need much more catalyst. Currently, three FCEVs producers attained a place in market and BMW, Daimler, General Motors, have plans to bring FCEVs to market soon.¹⁷ Assuming that the replacement of $0.1 \text{ mg}_{\text{Pt}}/\text{cm}^2$ with $2 \text{ mg}/\text{cm}^2$ carbon-based catalyst is accomplished, $200 \text{ g}_{\text{PGM-free}}/\text{vehicle}$ will be needed based on the targets and a demand for production of PGM-free catalysts with 100 tons/year will be created for 500,000 vehicles/year. Under the assumption of this accomplishment, the catalyst will also be used in the fuel cell applications other than FCEVs. Consequently, catalyst materials in the scale of hundreds of

tons will be needed in the near future and green synthesis will be one of the most important parts of the process together with sustainability.

Due to the concerns about utilization of hazardous chemicals such as hydrofluoric acid, silica templating is not a favorable synthesis method despite a high control on porosity development. A well-established carbon black industry is able to produce conductive carbons, however, the lack of technology for introduction of surface functional groups as well as narrow variation of characteristic properties such as pore size, particle size and surface area points out a limited freedom in terms of synthesis.

While state-of-the-art methods employ bottom-up synthetic approaches using iron, nitrogen and carbon precursors and subsequent heat treatment, the complications result from thermodynamic limitations are paid few attention. The heat-treatment of iron precursors causes the formation of side phases such as metallic iron and iron carbide particularly at high temperature. Furthermore, a number of parameters in the synthesis such as temperature, heating ramp, dwelling time, ratio of precursors, ball-milling conditions etc. create a huge database that has to be processed in order to gain a better understanding. The optimization of those parameters are often called active site engineering.¹⁸ Such a big load can be managed by employment of high-throughput combinatorial methods and machine learning based approaches.¹⁹ However, the effect of final structure cannot be studied as the isolation of active sites is not possible. Therefore, a new approach is needed to form more uniform sites in the final structure.

In 2018, Mehmood et al. introduced a novel approach named *Active Site Imprinting* addressing this particular issue in PGM-free catalyst synthesis¹⁰ The formation of Me-N₄ sites (Me: Mg) and exchanging this metal at low temperature with Fe resulted in a material without metallic

iron and carbide as well as high ORR activity. In 2019, Menga et al. extended this study by imprinting the active site with Zn and exchanging with Fe again relatively low temperature.²⁰ Although, *Active Site Imprinting* results in more uniform sites and the imprinting with Mg still outperforms Zn, the scalable synthesis stays as a big bottleneck for Mg-imprinted catalysts.

In Chapter 2, the development of a scalable synthesis for PGM-free will be covered using *Active Site Imprinting* method. The carbonization of metal-organic coordination polymer will be used for *Active Site Imprinting* method and the structure-activity relationship will be investigated. Although the synthesis method provides high yield and activity, it requires a new industry or adaptation of existing industries for the production of hundreds of tons catalyst.

Unlike the other industries such as carbon plate manufacturing and carbon black industry, there is certain industry more prone to adaptation to the carbon-based catalyst synthesis. One important example is Activated Carbon (AC) industry which has a market estimation of \$5305 million by 2020.²¹ Indeed, physical activation process was used by Union Carbide Corporation (UCC) in the synthesis of catalysts and supports for AFCs in 1960s.⁹ Besides, the deep know-how since the first reported industrial AC in 1911,²² can also be used for the synthesis as PGM-free synthesis requires a variety of carbon precursors such as agricultural waste, polymer and molecular carbon precursors, tailoring of porosity and a wide range of temperature treatments. Moreover, the surface modification studies and affinity towards heavy metal adsorption make ACs a perfect candidate for ORR catalyst.²³⁻²⁵

Activated carbons are commonly microporous materials that can be used in gas storage/separation, water purification, medicine, cosmetic and in many other applications.²² Activation process was described in different ways in the literature due to several synthesis methods. The synthesis methods include heat treatments at various temperatures in the presence

of activating agents that act on pore formation. These methods are classified in the literature according to the agent used in the activation process as physical (gas phase agents, CO₂, steam, N₂/O₂) and chemical activation (chemical agents, KOH, H₃PO₄, H₂SO₄, etc.).²⁶ Looking at the several ways of activation, the term can be described in general as making porous structures with large surface area.

In conventional chemical activation process, the impregnation of a chemical activating agent into a carbon precursor, heat treatment and washing steps lead to porous structure. This conventional method of porosity generation is limited by the temperature, concentration of the chemical and impregnation ratio.²⁷ However, there is still a debate about the mechanism of chemical activation in activated carbon community. Although, the mechanism has been reported as leaching of the precursor, it has also been shown many times that the increasing impregnation ratio (excess chemical activating agent) leads to the reduction in the surface area but increasing pore volume.²⁸⁻²⁹ In 2004, Molina-Sabio mentioned this behavior as the contraction inhibiting effect of the chemical agent in the precursor along the heat treatment but there has been no detailed study since then.³⁰ Also, such a behavior observed for ZnCl₂ created new type of synthesis for carbons before as molten ZnCl₂ acts as template in the synthesis.³¹

According to the previous findings in the conventional chemical activation process, we investigated the pore formation process with the following hypotheses:

- Brønsted acids act as template in the synthesis of active carbons
- Excess amount of Brønsted acids changes the mechanism in which the carbon precursors are dispersed in acid
- High temperature synthesis can be achieved by less volatile (water-free) acids

In Chapter 3, mechanistic investigation of porous carbons synthesized with Brønsted acids will be covered according to our hypotheses mentioned above and the role of this mechanism in electrochemistry (ORR) will be explained.

1.3 PGM-free ORR Electrocatalysts

The motivation behind the current researches for reduction or completely replacement of Pt is based upon the feasibility concerns of FCEVs and limits due to the low abundance of Pt. In order to reach decent power in a fuel cell stack, large amount of platinum is required which poses a problem for the commercialization of FCEVs. Although the low abundance of platinum has always been considered as big issue, recent developments particularly in recycling process suggest that the global estimated amount of Pt reserves seems satisfactory for 2.5 billion FCEVs if used entirely for FCEVs.³ However, even today Pt is used also for jewellery, electrical and electronic parts, dental and medical applications and for other catalytic applications. Considering the industrial uses other than FCEVs, the reserves will be a major bottleneck in the future. Furthermore, it is worth noticing that the total amount of platinum supplied from mined and recycled sources is 606.5 tons per year (showing a stable trend for last 8 years) indicating that we need 123 years to produce 2.5 billion FCEVs with 30 g Pt per vehicle.³² Assuming that the utilization of Pt solely in FCEVs is not possible, this will eventually affect the price of Pt in the future as Pt price shows high volatility. The yearly Pt price between September 2000 and June 2020 is depicted in Figure 1.3.2 (by averaging the monthly prices reported by Johnson Matthey)³³ and the fluctuation between 533 \$/oz and 1725 \$/oz indicates the sensitivity of Pt price.

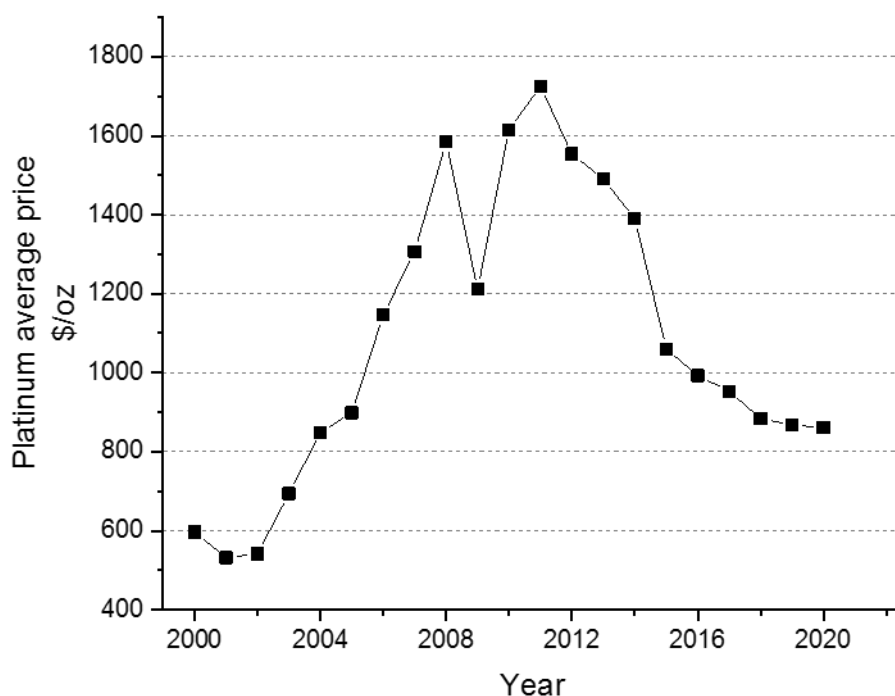


Figure 1.3.1: Pt price averaged for years using the data from Johnson Matthey.³³

Looking at the statistics and projections, Department of Energy (DOE) has set the target for platinum amount as 0.125 mg PGM/cm² in both electrodes (total) for 2020 and General Motors targets a total platinum amount per FCEV as 10 g.³⁴⁻³⁵ While targets are defined based on the system cost and feasibility studies, annual production rate of Pt is still a limiting factor and even if the targets are reached, additional 40 years is required for production of 2.5 billion FCEVs. In this context, completely replacement of Pt with scalable and inexpensive catalyst at least in the cathode part is crucial.

The pioneering work in PGM-free catalysts is widely accepted as 1964, when Jasinski found out the activity of Cobalt phthalocyanine in alkaline medium.³⁶ Since then, important achievements were obtained in the synthesis routes and performance by many research

groups.³⁷⁻³⁹ Unfortunately, it took a long time to be considered as an alternative catalysts that can be really used in the fuel cell stack. Early projections did not involve PGM-free catalysts due to the low activity compared to Pt.⁴⁰⁻⁴¹ However, the breakthrough in 2009³⁹ was strong enough to broaden the perspective. Following that, Gasteiger and Markovic gave a wide coverage to PGM-free catalysts in a perspective paper and ended with: “*Despite a number of remaining challenges, these recent successes bring us closer to completing our quest to put PEM fuel cell technology on the road.*”⁴²

Significant improvements have been made after Lefevre’s finding.⁴³⁻⁴⁵ In 2017, Banham and Ye reviewed these improvements and concluded as: “*PGM-free catalysts are now close to meeting the requirements for portable power applications.*”⁴⁶ In the light of these developments, Ballard Power Systems announced the first commercial portable PEMFC product that utilizes PGM-free in the cathode.¹⁶ Overall, PGM-free catalysts made indelible impression particularly in last 10 years such that the number of articles including the keywords *PGM-free or non-precious metal and oxygen reduction reaction* increase drastically (Figure 1.3.2).⁴⁷

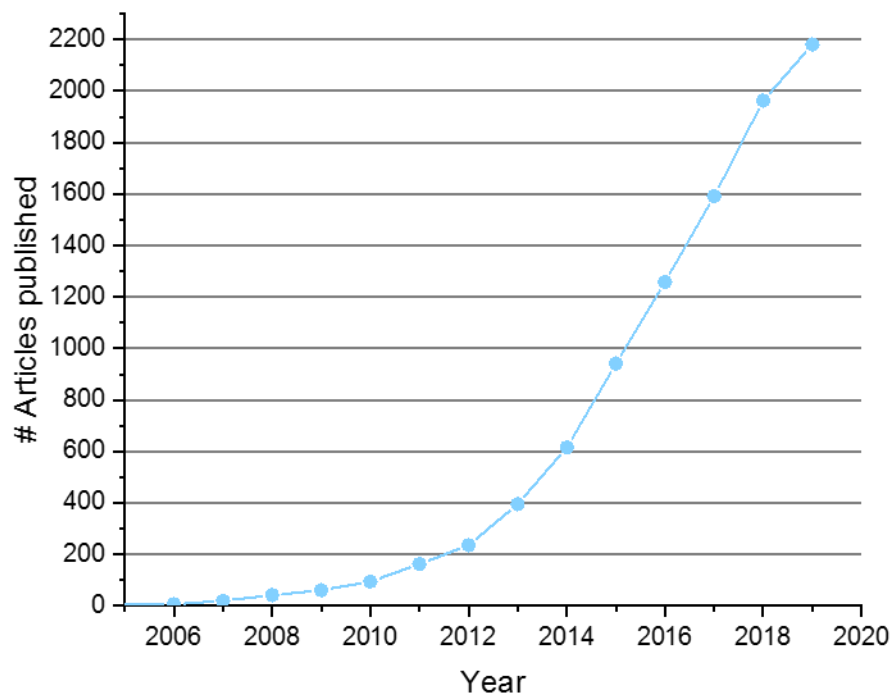


Figure 1.3.2: Number of articles including the PGM-free related keywords published in last 14 years (searched on May 2020).⁴⁷

2. Active Site Imprinting Method

2.1 Introduction

The typical synthesis of PGM-free catalysts involves multiple steps namely heat treatment of carbon, nitrogen and metal precursors ball milling, acid etching and another heat treatment (Figure 2.1.1).⁴⁸ A porous structure is either created in-situ by pyrolysis of carbon precursors via different methods such as templating⁴⁹⁻⁵⁰ or introduced by a well-defined support at the beginning of the synthesis.^{39, 51} The porosity of the final catalyst is significant in terms of mass transport, accessibility of active sites and volumetric activity. Therefore, tunability of the porosity is desired in the synthetic routes. Templating methods have the advantage over the commercial carbons (Ketjenblack, Vulcan, Black Pearls, Carbon Nanotubes) as the higher degree of tunability is possible. As the carbon matrix hosts the active sites, porosity can be considered as one of the limiting factor for activity.

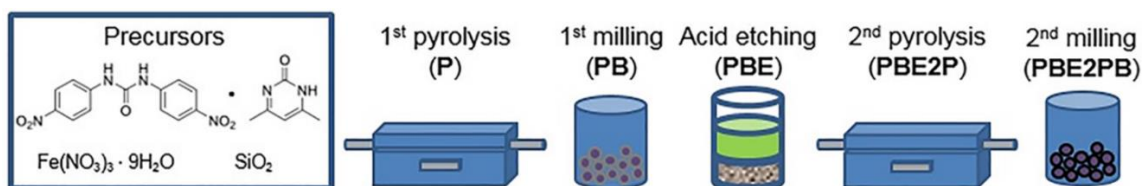


Figure 2.1.1: Typical synthesis steps of PGM-free catalysts. Reprinted with permission from ref 48. Copyright (2020) American Chemical Society.

Another limiting factor is the number of active sites for PGM-free catalysts. Although the number of active sites can be increased by higher catalyst loadings, the loading is limited by the dimensions of the electrodes as higher loadings cause thicker catalyst layers. Instead of the number of active sites, the active site density is desired to be increased. Therefore, the selection of nitrogen precursors play an important role. Recently, metal organic frameworks (MOFs)

based precursors attracted enough attention to be used in the synthesis as a carbon and nitrogen precursors.⁵²⁻⁵⁴ The porosity is obtained by the MOFs well-defined porous structure, despite the changes during the pyrolysis step and nitrogen is provided by again the chemical structure of MOFs. The most popular MOF used recently is Zeolitic Imidazolate Framework-8 (ZIF-8) due to its high nitrogen content and high porosity. The utilization of ZIF-8 results in the high activity of PGM-free catalyst.⁴⁵

The metal precursors play another big role as they provide the metal and complete the active site formation. So far, the active metals for ORR were found as Fe, Co and Mn. Also the lowest ORR overpotential for PGM-free catalysts (in graphene with N₄ coordination) was reported as Fe, using density functional theory (DFT) calculations.⁵⁵ Unfortunately, experimentally systematical investigation is not possible as many side phases are formed in the synthesis, particularly during pyrolysis step.

While the traditional synthesis methods provide good activity, a new approach was introduced in 2018 by Mehmood et al.¹⁰ Unlike the typical PGM-free synthesis, Fe/Co precursors were not subjected to heat treatment as formation of carbide and metallic species is thermodynamically favorable at high temperature. Instead, magnesium was used to imprint the active sites and MgN₄ pocket was formed with heat treatment. Fe was introduced at low temperature (80 °C) at which the metallic Fe and carbide formation is not favorable. The exchange of Mg with Fe resulted square planar FeN₄ pocket that is free of any metallic Fe and Fe carbide species. In another study, Menga et al. studied active site imprinting with Zn, improving the ion exchange process.²⁰ The coordination of Fe³⁺ increased the activity by 383 mV at halfwave potential and the concept was proven by using identical location atomic resolution transmission electron microscopy as well as in-situ electrochemical flow cell coupled to inductively coupled mass

spectroscopy. These two works opened a frontier for the synthesis of PGM-free catalysts. In Chapter 2.2, the synthesis of scalable and highly active ORR catalyst will be covered.

2.2 Scalable and Highly Active PGM-free Catalysts

The promising approach introduced by our group as active site imprinting method requires a imprinted nitrogen doped carbon support which fulfills certain criteria such as enough porosity and suitable structure that hosts Me-N₄ moieties. These criteria were met by synthesis of carbon with salt melt method. The salt melt acts as both porogen and metal precursor to form MeN₄ sites. In the first study, MeN₄ sites were formed on carbon using adenine and MgCl₂.6H₂O.¹⁰ Despite the high activity and low Tafel slope, the scalability was not sufficiently good for industrial scale synthesis. The extension of the method to Zn-imprinted catalyst resulted in atomically dispersed Fe-N-C that is free of metallic iron and iron carbide.²⁰ Furthermore, a deeper analysis of the active sites were carried out by Mössbauer experiment conducted at liquid Helium temperature for more accurate analysis of the active sites. Although, Mg still outperforms Zn imprinting, the scalable synthesis is a big bottleneck for the industrial scale synthesis. In this thesis, a scalable synthesis for *Active Site Imprinting* method is developed.

The potential platform material was synthesized by Eisenberg's group. Nitrogen doped carbon prepared from well-defined magnesium based metal-organic coordination polymer (MOCP) showed high specific surface area (SSA). Thus, these materials show big potential to be a platform material for the active site imprinting to achieve FeN₄ groups in case the Mg is imprinting the nitrogen doped carbon.

The synthesis of the MOCP itself uses inexpensive off the shelf reagents. It combines a metal cation and a nitrogen containing ligand. The different types of the ligand enable flexibility of MgN_x coordination which also allows room for further control on the synthesis. Therefore, this feasible and scalable synthesis makes MOCP an excellent platform for active site imprinting method.

In this study, we extend the active site imprinting method to Mg-imprinted, scalable and highly active ORR catalyst. Hierarchical pore systems were obtained by heat treatment of magnesium iminodiacetic acid metal organic coordination polymer (Mg-IDA MOCP) and high surface area catalysts were synthesized ($>1100\text{ m}^2/\text{g}$) by exchanging Mg with Fe (transmetallation) at $80\text{ }^\circ\text{C}$. The formation of active sites at such low temperature resulted in atomically dispersed highly active catalyst despite the low amount of iron (wt.%). Our findings show that the active site imprinting method introduces active sites that are efficiently utilized in ORR.

The metal-organic coordination polymer Mg-IDA (magnesium diaminoacetate) was chosen as a precursor towards active-site imprinted nitrogen doped carbons. Mg-IDA has a high N/C ratio and despite the high oxygen content it was previously shown that basic N-sites are commonly present in the final carbon product.

Mg-IDA was prepared via precipitation from magnesium carbonate and Iminodiacetic acid with a yield of 50%. The obtained precipitate was dried and pyrolyzed at four different temperatures; 800, 850, 900 and $950\text{ }^\circ\text{C}$ in flowing argon, and fine black powders were obtained. These carbons are composed of magnesium oxide particles encapsulated by NDC. The magnesium oxide is removed with a hydrochloric acid wash, leaving behind high SSA porous carbon and MgN_4 sites or vacant MN_4 sites. The carbons were investigated by high resolution scanning electron microscope (HRSEM) before and after transmetallation.

The Mg/NCs were then coordinated with Fe(II) ions with a FeCl₂ solution in methanol under reflux at 80 °C. Acidic work-up and drying gave the PGM-free electrocatalysts powders [Fe(NC_800)], [Fe(NC_850)], [Fe(NC_900)] and [Fe(NC_950)].

The gas sorption experiments provide information about the pore structure and the surface area of the materials by means of the theories developed for the physisorption phenomenon. The effect of iron coordination on the materials porosity was evaluated using N₂ gas sorption porosimetry. Similarities in terms of the shapes of the isotherms before and after coordination reveal that the coordination process is conservative towards the general morphology of the materials, i.e. the Mg/NC backbones remain mechanically stable (Figure 2.2.1). For all isotherms, steep increases in gas uptake are observed at low p/p_0 values, indicating the presence of micropores (< 2 nm).⁵⁶ The slope after the steep increase at relatively higher p/p_0 values shows the 1) multilayer adsorption on the external surface and 2) an uptake by mesopores (2 nm < d < 50 nm) in the range where desorption hysteresis is observed. At very high p/p_0 values, the uptake values reach to a plateau. All the isotherms present very similar shape (type IVa classification of micro- and mesoporous carbons)⁵⁶, despite the change in the uptake values. Also the characteristic hysteresis (H4) for micro- and mesoporous carbons with dominating microporosity is observed in each sample with a step-down closure at 0.4 p/p_0 indicating the connectivity of mesopores via small “bottle-neck” pores (cavitation/blocking effect).⁵⁶⁻⁵⁷ The pore size distribution (PSD) graphs derived from the adsorption branch of the isotherms using a quenched-solid DFT model for slit, cylindrical, sphere pores show three distinct peaks appearing at ~ 1.0, 3.5 and 6.5 nm for each sample. For [Fe(N/C_800)], [Fe(N/C_850)] and [Fe(N/C_950)] the characteristic pore sizes remain unchanged after Fe ion coordination (Figure S2.2.1). However, a vertical offset towards smaller gravimetric gas uptakes is observed for

those samples, indicating of the increased specific weight connected to the coordination of Fe. Surprisingly, [Fe(N/C_900)] is an exception of this trend and instead an increased gas uptake is observed after coordination.

Apparent SSA determination according to BET theory reveals high surface area and large total pore volume (TPV) for all samples, revealing the materials to be promising electrocatalysts from a morphological perspective (Table 1). The samples synthesized at entire range of temperature (800-950 °C) exhibit SSA above 1100 m² g⁻¹, which arises mainly due to the presence of mesopores. Therefore, these catalysts appear promising especially for the mass transport, but also in terms of catalyst layer density. Iron coordination causes a decrease in the micropore surface area (S_{micro}) in all samples indicating that Fe is coordinated in the structure as acidic work-up is carried out after the process whereas the S_{meso} varies depending on the synthesis temperature.

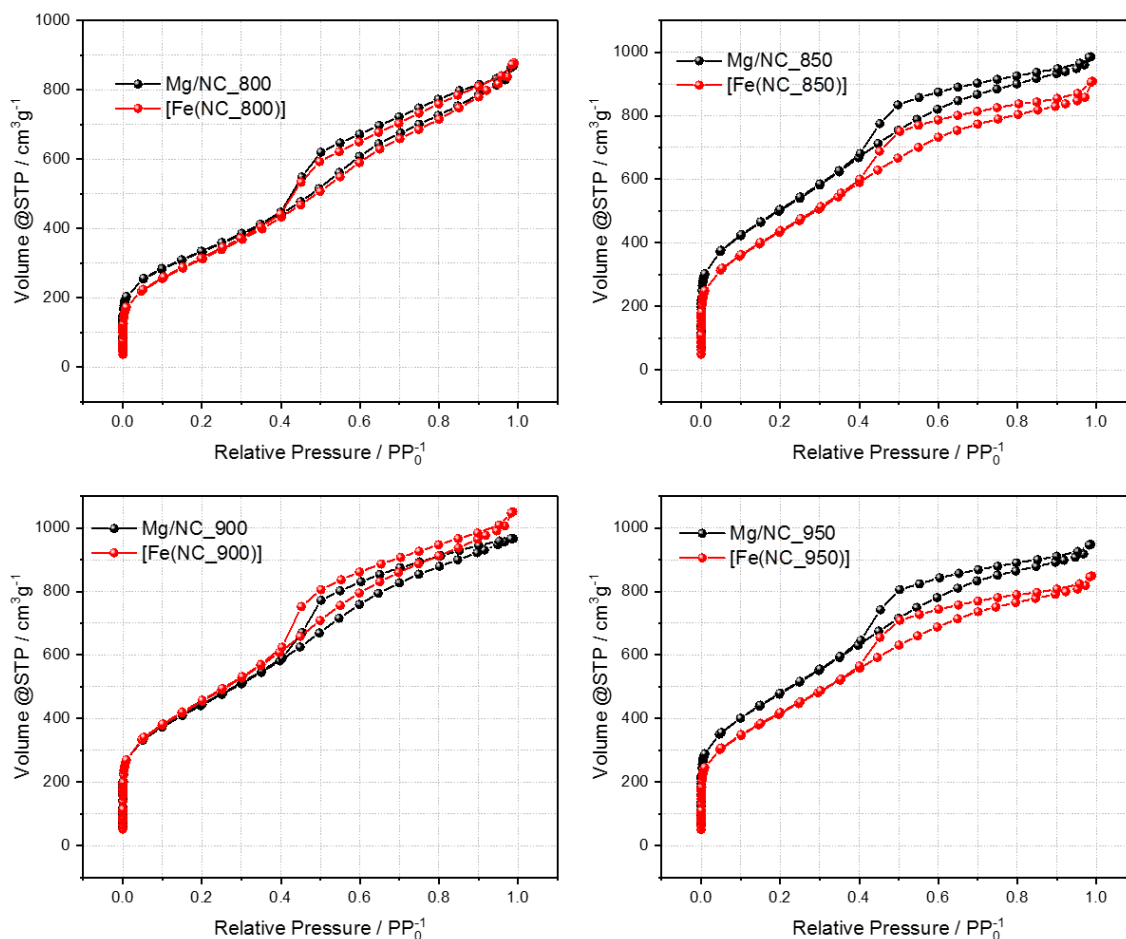


Figure 2.2.1: N₂ isotherms of Mg/NC and [Fe(N/C)] samples synthesized at; a) 800 °C, b) 850 °C, c) 900 °C, d) 950 °C.

Table 2.2.1: Pore structure of Mg/NC and [Fe(N/C)] samples.

Sample	SSA (m ² /g)	S _{micro} (m ² /g)	S _{meso} (m ² /g)	V _{micro} (cm ³ /g)	V _{Total} (cm ³ /g)
Mg/NC_800	1175	372	803	0.14	1.34
[Fe(N/C_800)]	1116	183	933	0.08	1.35
Mg/NC_850	1780	686	1094	0.27	1.52
[Fe(N/C_850)]	1569	477	1092	0.20	1.40
Mg/NC_900	1565	563	1002	0.22	1.49
[Fe(N/C_900)]	1614	471	1143	0.20	1.62
Mg/NC_950	1708	666	1042	0.25	1.46
[Fe(N/C_950)]	1496	505	991	0.20	1.31

SEM reveals the porous morphology of the carbon, in accordance with the porosimetry analysis, mesopores are clearly seen while micropores are hardly visible due to the dense structure of the samples. In addition to N_2 sorption porosimetry, big pores (> 200 nm) are also seen in HRSEM images with concave surface which might be formed as a result of the removal of magnesium oxide phases. The images also show that there is no major morphology change after transmetallation process (Figure 2.2.2).

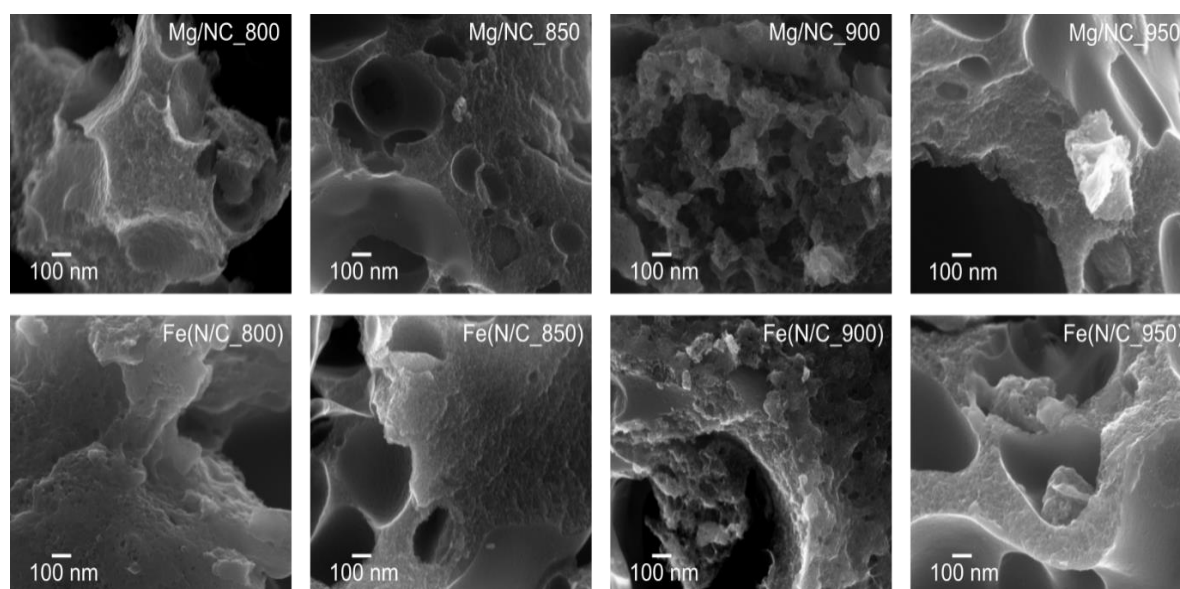


Figure 2.2.2: SEM of the carbon samples before transmetallation (top row) and after transmetallation (bottom row).

The investigation of the surface moieties provides an information about the activity-structure relationship in PGM-free catalysts. Particularly, N 1s spectra are effective for qualitative and quantitative analysis of different nitrogen types in the graphene-like carbon matrix. Therefore, N 1s spectra are useful for comparison and optimization of the samples synthesized at different temperatures. In this study, the surface functionalities of the samples were investigated using X-ray photoelectron spectroscopy (XPS). It is well known phenomenon that the absolute

amount of nitrogen is a function of temperature especially after 800 °C and the conversion of certain nitrogen species is expected with increasing temperature.^{10,58} Moreover, the assignment of the nitrogen helps to identify the nitrogen atoms that are bound to metal or in pyridinic, pyrrolic, graphitic or oxide forms. The temperature dependency of nitrogen species can be seen in N1s spectra of Mg/NC samples (Figure 2.2.3).

The N 1s spectra of nitrogen-doped carbons are typically deconvoluted into five different types of nitrogen namely pyridinic (~398.2 eV), metal-bonded (~399.5 eV), pyrrolic (~400.5 eV), graphitic (~401-402 eV) and oxidized nitrogen species (~402-403 eV).⁵⁹ The binding energies show consistency with the literature works. Also, Table 2.2.2 reveals that the temperature has effect on quantities of the surface nitrogen atoms as well as carbon and oxygen. The relative percentage of total nitrogen content is stable between 800 °C and 900 °C, then decreases at higher temperature. Similarly, the percentage of Me-N peaks at 900 °C reach to a maximum value creating possibility of higher number of active sites.

Table 2.2.2: The elemental composition and relative abundance of different nitrogen species in the Mg/NC samples.

Sample	at% Total			Relative % Nitrogen				
	C	N	O	Pyridinic	Pyrrolic	Me-N	Graphitic	N-O
Mg/NC _800	87.9	6.61	5.49	35.92	30.38	18.17	11.85	3.69
Mg/NC _850	88.20	6.29	5.51	34.39	29.44	21.47	11.01	3.69
Mg/NC _900	89.44	6.78	3.77	31.95	24.53	23.63	14.50	5.39
Mg/NC _950	91.11	5.02	3.87	28.57	26.43	18.56	17.13	9.31

The surface functionalities changed upon synthesis temperature. For instance, the temperature increase leads to increased concentration of graphitic N as well as conductivity. However, the

metal-N bond content decreases with increasing temperature. This alteration of surface was studied by thermogravimetric analysis coupled by mass spectrometer (TG-MS). Mg/NC_800 was subjected to a heat treatment in inert atmosphere from room temperature to 950 °C with the same heating ramp that was used in the synthesis. A drying/degassing step was implemented at 100 °C for 1 hour followed by ramping the temperature up to 950 °C at which the last sample was synthesized. A steep decrease in the relative weight indicates the desorption of physisorbed species (H₂O, CO₂, N₂ etc.) at room temperature (Figure S2.2.2). MS signals of CO₂ (m/z=44, 45, 22) show a peak around 200 °C pointing to decarboxylation and follow a steady trend until the structural decomposition temperature (650 °C) starts. At higher temperatures stronger evolution of NO (m/z=30) and CO₂ (m/z=44, 45, 22) is observed, which can explain the reduced content of those heteroatoms with increasing temperature. Interestingly, the formation of NO reaches a maximum at ~800 °C and in addition, no pronounced formation of N₂ gas is observed over the whole reaction range. This can explain the moderate total loss of nitrogen dopants throughout carbonization (Table 2.2.2) and may be an indication for stable Mg-imprinted N sites.

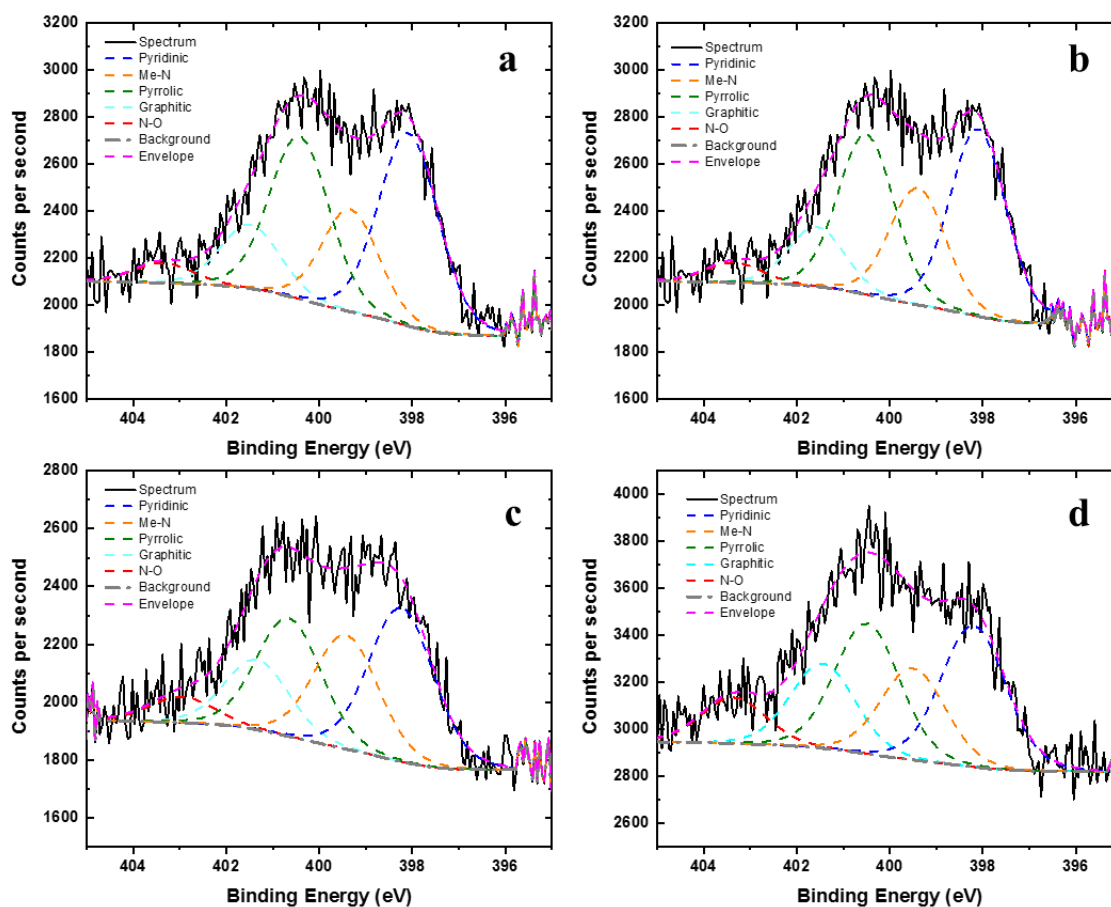


Figure 2.2.3: N1s spectra of; a) Mg/NC_800, b) Mg/NC_850, c) Mg/NC_900, d) Mg/NC_950.

The transmethylated samples exhibit similar N1s spectra (Figure S2.2.3) but altered quantities. Table 2.2.3 reveals that the relative graphitic nitrogen content remains intact after introducing Fe to the structure, as expected. However, the effect of Fe can be clearly seen in Me-N, pyridinic and pyrrolic nitrogen percentages that change for each sample after transmetalation. Metal bonded nitrogen content increases at each temperature after transmetalation due to both Mg exchange and coordination of Fe. The total nitrogen and carbon content (at%) decrease possibly due to the formation of small oxidic iron cluster beside the coordination of iron with nitrogen

like in the case of Menga et al.²⁰ As Me-N bond and nitrogen contents are important for transmetallation step, Mg_IDA-900 sample show high potential for *Active Site Imprinting*. Therefore, Mg_IDA_900_TM was studied for further analysis and tests.

Table 2.2.3: The elemental composition of [Fe(NCs)].

	at% Total			Relative % Nitrogen				
	C	N	O	Pyridinic	Pyrrolic	Me-N	Graphitic	N-O
[Fe(NCs)]_800	87.76	6.60	5.64	31.51	32.73	21.36	11.60	2.80
[Fe(NCs)]_850	87.16	6.04	6.81	31.11	28.05	25.95	10.60	4.28
[Fe(NCs)]_900	88.93	5.63	5.44	32.97	22.30	24.40	14.16	6.18
[Fe(NCs)]_950	90.06	4.81	5.12	30.00	23.28	23.73	17.10	5.89

The synthesis temperature selected for the further analysis is the best among the temperature range selected for the formation of ORR active sites on porous structure. Highly micro- and mesoporous structure of platform material (Figure 2.2.5a) facilitates the exchange of Fe with Mg atoms (formation of FeN₄) on its large surface. Transmission Electron Microscopy (TEM) provides information about the carbon structure (porosity, particle size etc.) employing electron beams and using different modes, even single atoms can be monitored with high resolution. Therefore, the porosity and distribution of Fe atoms were monitored with TEM with High Angle Annular Dark Field (HAADF) detector. The micrographs reveal highly porous carbons both before and after transmetallation (Figure S2.2.4). The HAADF contrasts between light and heavy atoms - thus the lightweight carbon and magnesium are dark, and the heavy iron is bright. These images and mapping show atomically dispersed Fe atoms (Figure 2.2.5b) despite the acidic work-up (0.1 M HCl) indicating the successful transmetallation process. Also, some clusters (2-4 nm) were observed due to the formation of iron oxide (Figure S2.2.5). However, Powder X-ray Diffraction (XRD) patterns (Figure S2.2.6 and S2.2.7) do not provide much information to resolve these species due to either small or very few relatively big crystalline

species. STEM EDX measurements revealed the presence of oxygen. Furthermore, Mg atoms detected in EDX point out some Mg left after transmetallation.

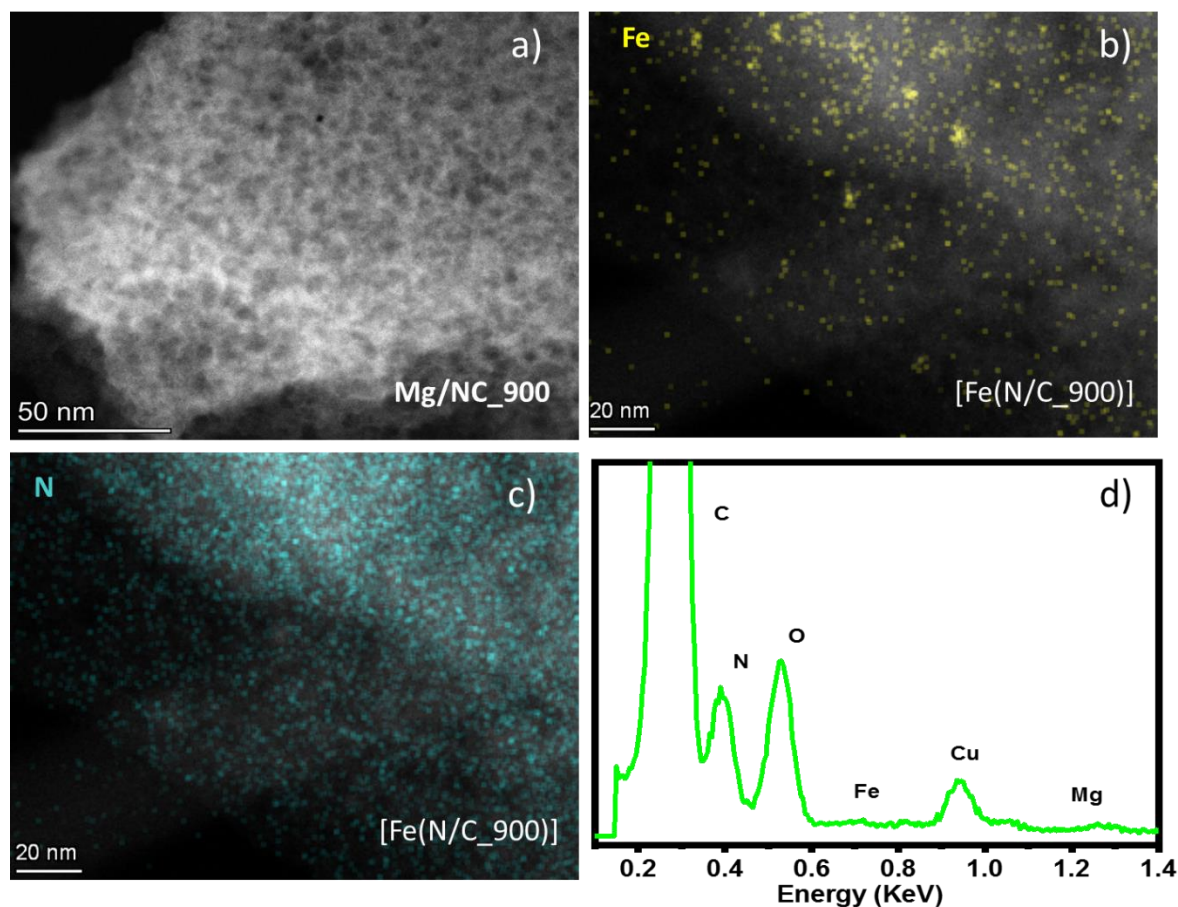


Figure 2.2.5: TEM images of the carbon samples synthesized at 900 °C; a) Mg/NC, b) Fe mapping of [Fe(N/C)], c) N mapping of [Fe(N/C)], d) EDX spectrum of [Fe(N/C)].

Mössbauer spectroscopy is often used for the analysis of the chemical environment of the active sites in FeNC materials. Unlike XPS, Mössbauer spectroscopy is bulk technique which helps understand the chemistry deeper. Therefore, the chemical structure of [Fe(NC)] catalyst was further analyzed by Mössbauer spectroscopy. Room temperature measurements were recently shown to potentially cause overestimation of FeN₄ active sites species. This is since small oxidic iron clusters/nanoparticles may appear as doublets at room temperature and only magnetize at very low temperature, requiring e.g. cooling with liquid helium at 4.2 K.^{20, 60} The

low temperature provides hyperfine splitting and prevents the random alignment of the spins. Thus, the singlet that is related to the super-paramagnetic iron does not appear in the spectrum.⁶¹ The measurements at 4.2 K is, therefore, a helpful choice to distinguish the iron species more accurately.

The spectrum acquired for [Fe(NC_900)] exhibits a sextet and two doublets at 4.2 K (Figure 2.2.6). The sextet is assigned to small oxidic clusters/nanoparticles (< 3nm) that are formed throughout coordination with iron or the aqueous work-up and apparently withstand the acidic work-up. Different doublets (D1, D2 and D3) for FeNC catalysts are mostly attributed to FeN₄ sites with different electronic surroundings of Fe. The determined main parameters (Table S2.2.1) for our fitting (quadrapole splitting and isomer shift) are in good agreement with the doublets denoted as D1 and D3 in the respective literature.²⁰ Among these doublets, the D1 content was previously correlated to the ORR kinetic current and it was identified as located on surface, thus main contributor of ORR.⁶²⁻⁶⁴ D3 is typically assigned to high spin Fe²⁺.²⁰ Although, the room temperature measurements show no correlation between D3 content and ORR activity, the effect of this site on ORR is still unclear. For [Fe(NC_900)], D1 contributes 42.9% to the total iron content, which is amongst the highest fractions reported in the literature to date (Table S2.2.2) as transmetallation is effective on the surface, rendering the synthesis as very promising towards selective tailoring of the active sites. Furthermore, the iron content is calculated as 0.78 wt% from Mössbauer spectroscopy.

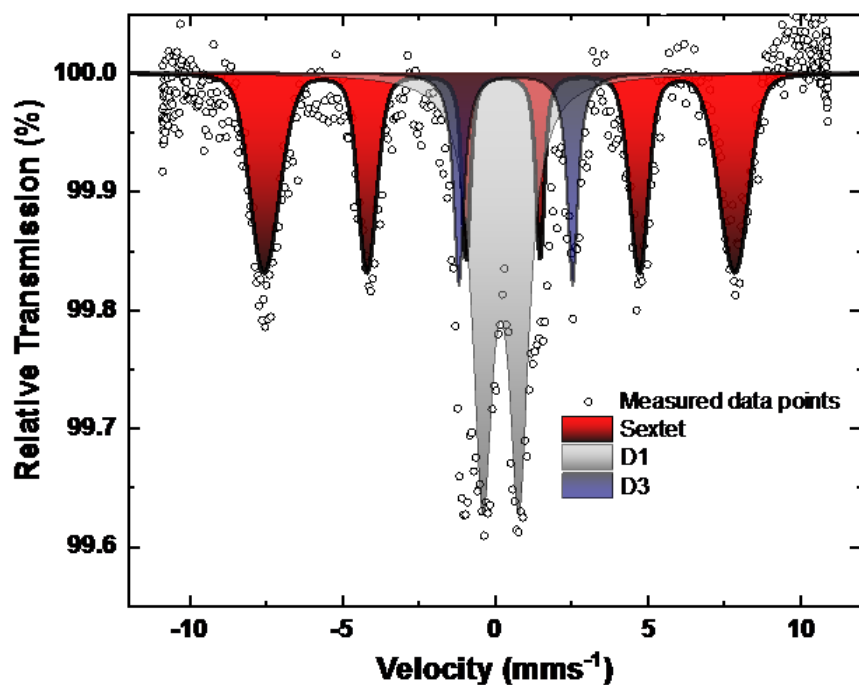


Figure 2.2.6: Mössbauer spectrum of [Fe(N/C_900)].

The ORR activities of the samples were measured using RDE set-up in 0.1 M HClO₄ with 200 $\mu\text{g}/\text{cm}^2$ and 500 $\mu\text{g}/\text{cm}^2$ loadings. Mg-IDA samples exhibit onset potential of 0.7 V with poor ORR activities even at low potentials. Iron coordination improves the activity by more than 300 mV for each sample resulting in onset potentials of 0.85 V. Half wave potentials ($E_{1/2}$) are commonly used activity descriptors and are determined as 0.63, 0.68, 0.69 and 0.7 V for [Fe(NC_800)], Fe(NC_850)], Fe(NC_900)] and Fe(NC_950)], respectively (Figure 2.2.7). Furthermore, the mass activities calculated at 0.8 V (Table 4) are found to be similar to the commercial catalyst Pajarito Powder (Table S2.2.3).

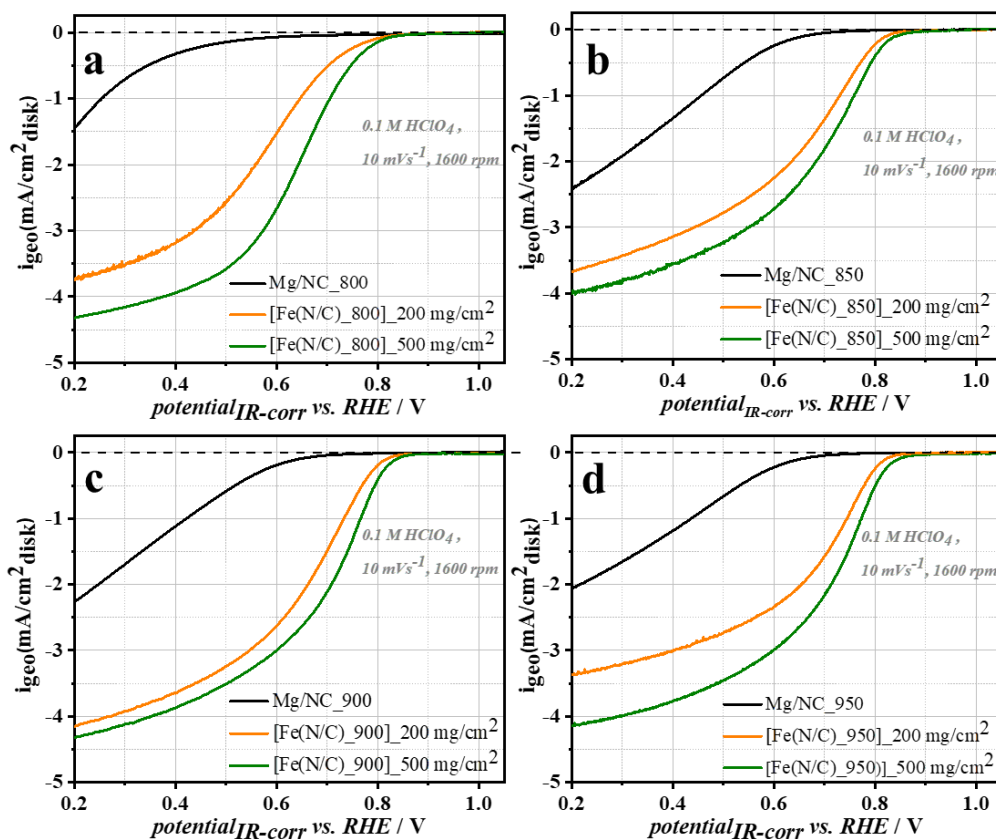


Figure 2.2.7: ORR activities of the samples in RDE set-up; a) 800 °C, b) 850 °C, c) 900 °C, d) 950 °C; Mg/NC (200 $\mu\text{g}/\text{cm}^2$) (black), [Fe(N/C)] (200 $\mu\text{g}/\text{cm}^2$) (orange), [Fe(N/C)] (500 $\mu\text{g}/\text{cm}^2$) (green).

Table 2.2.4: Activity indicators of transmetallated samples.

Sample	$E_{1/2}$ (V)	I_m (A/g) _{@0.8 V⁺}
[Fe(NCs)]_800	0.63	0.36±0.10
[Fe(NCs)]_850	0.68	0.96±0.12
[Fe(NCs)]_900	0.69	0.95±0.04
[Fe(NCs)]_950	0.7	1.22±0.11

+Standard deviations were calculated from the activities of two different loadings.

The stability/durability is one of the main challenges for the applicability of PGM-free catalysts particularly in vehicles where the maintaining the activity after thousands of cycles is required.⁶⁵⁻⁶⁶ Due to the different degradation mechanisms, stability/durability becomes a

function of potential window. One important reason for activity loss is carbon corrosion, which causes poor electrical contact between active sites and carbon matrix. Although the carbon corrosion (Reaction 3) is thermodynamically possible above 0.2 V vs RHE, the carbon oxidation kinetics are slow below 0.6 V and more realistic above 0.8V and up to 1.4-1.5 V.⁶⁷ In this study, cycling experiments between open circuit voltage (OCV) and 1.4 V were performed to mimic the operational conditions caused by start-up and shut-down of fuel cells, which increase carbon corrosion at the cathode.⁶⁸ The activity in O₂-saturated solution after 1, 100, 1k and 5k cycles in N₂ between OCV and 1.4 V was monitored using RDE. The results show that the activity slightly decreases after 100 cycles whereas considerable activity drop is observed after 1k cycles (Figure 2.2.8).



Also, CVs indicate increase in the double layer capacitance and pseudo-capacitive currents showing an agreement with the literature pointing to a change in the surface roughness (Figure 2.2.8).⁶⁹ The corrosion resistance is often related to microstructure and surface properties of the carbons particularly for those synthesized without a post-heat treatment.⁶⁹ It is noteworthy that for such carbons possessing large surface area (>1100 m²/g), relatively big pore sizes (> 6nm) and high amount of surface functional groups (O content > 3.7 at%), the change in the capacitance is not significant compared to the samples prepared in a similar way (single heat treatment).⁶⁹

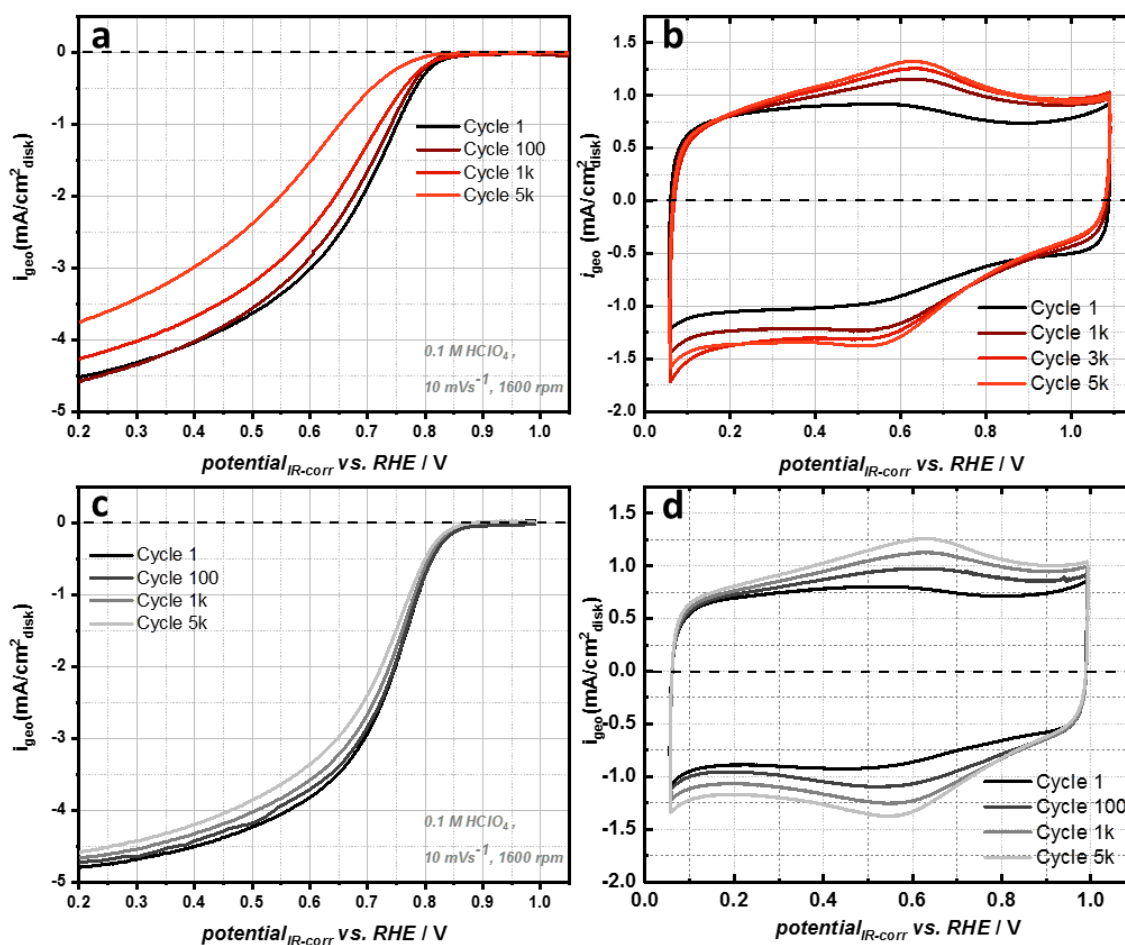


Figure 2.2.7: Carbon corrosion test results for a,b) $[\text{Fe}(\text{N}/\text{C}_{900})]$ and c,d) $[\text{Fe}(\text{N}/\text{C}_{900}_{950})]$: LSVs (a,c) were recorded in O_2 -saturated and cyclic voltammeteries (b,d) were recorded in N_2 -saturated 0.1 M HClO_4 after 1, 100, 1k and 5k cycles.

Further improvement in the activity was obtained by a post-heat treatment under inert gas (N_2). The post-heat treatment carried out in this study differs from the treatments in typical PGM-free synthesis (Figure 2.1.1) as Fe is coordinated at low temperature. $[\text{Fe}(\text{N}/\text{C}_{900})]$ was heated up to $950\text{ }^\circ\text{C}$ with a heating ramp of $10\text{ K}/\text{min}$ and held for 30 min and denoted as $[\text{Fe}(\text{N}/\text{C}_{900}_{950})]$. The treatment did not lead to formation of new crystalline species as PXRD pattern (Figure S2.2.8) does not exhibit any defined peaks similar to the ones before heat treatment.

The activity measured in RDE setup shows considerable improvement after post-heat treatment. Beside the limiting current, the mass activity increases to 1.4 A/g at 0.8 V indicating that the faster kinetics were achieved by post-heat treatment (Figure 2.2.8). Although the effect of post-heat treatment was discussed before⁶³, the cause behind the consequences of this treatment is yet unknown. A number of hypotheses was suggested such as removal of functional groups, more basic nitrogen groups etc. but it is noteworthy that the effect of this treatment must be studied taking the chemistry of the starting material into consideration. In this study, the treatment was performed on the material without any metallic iron or iron carbide.

Carbon corrosion test performed on [Fe(N/C_900_950)] sample shows higher stability compared to the one without post-heat treatment (Figure 2.2.7 c,d). Although there is still an obvious increase in capacitive current, the activity in O₂ saturated solution remains in an acceptable range even after 1k cycles. At 0.6 V, only 6% and 12% losses are observed after 1 k and 5 k cycles, respectively. The halfwave potential measured after 100, 1 k and 5 k cycles

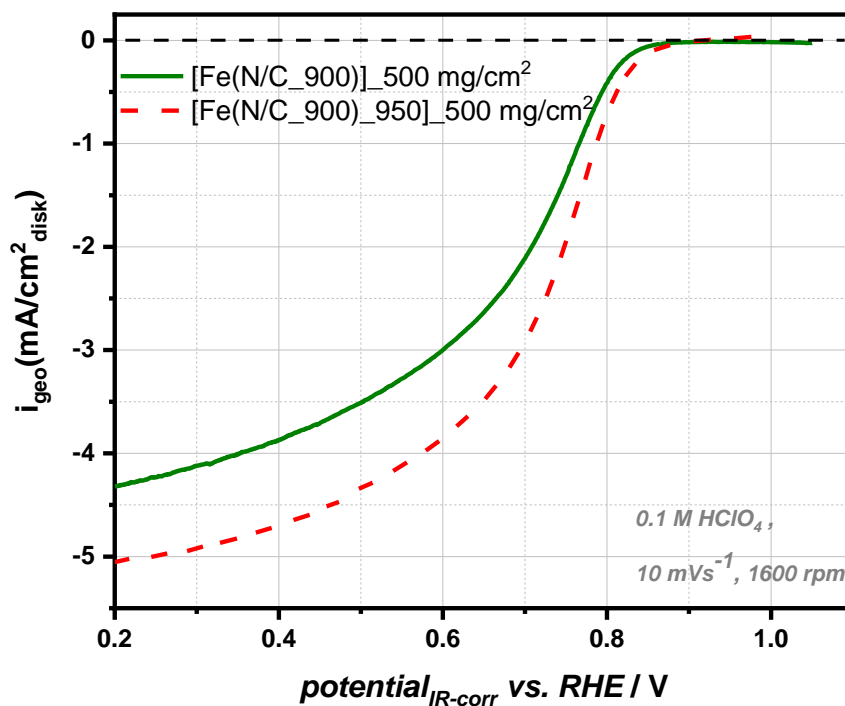


Figure 2.2.8: Activities of the samples with and without a post-heat treatment tested in RDE.

The activity was further tested in MEA scale. The electrodes were prepared by coating on PTFE (polytetrafluoroethylene) foil aiming a loading of 2 mg/cm². The preparation method is described in Chapter 4. The polarization curve obtained in O₂-H₂ with differential flow configuration shows a promising activity with an unexpected high OCV (0.93 V) despite the low Fe content. Unlike the high OCV and decent performance at low current density, a low activity is obtained at high current density. The cell voltage reaches 270 mA.cm² at 0.6 V indicating a limited activity at higher current density region.

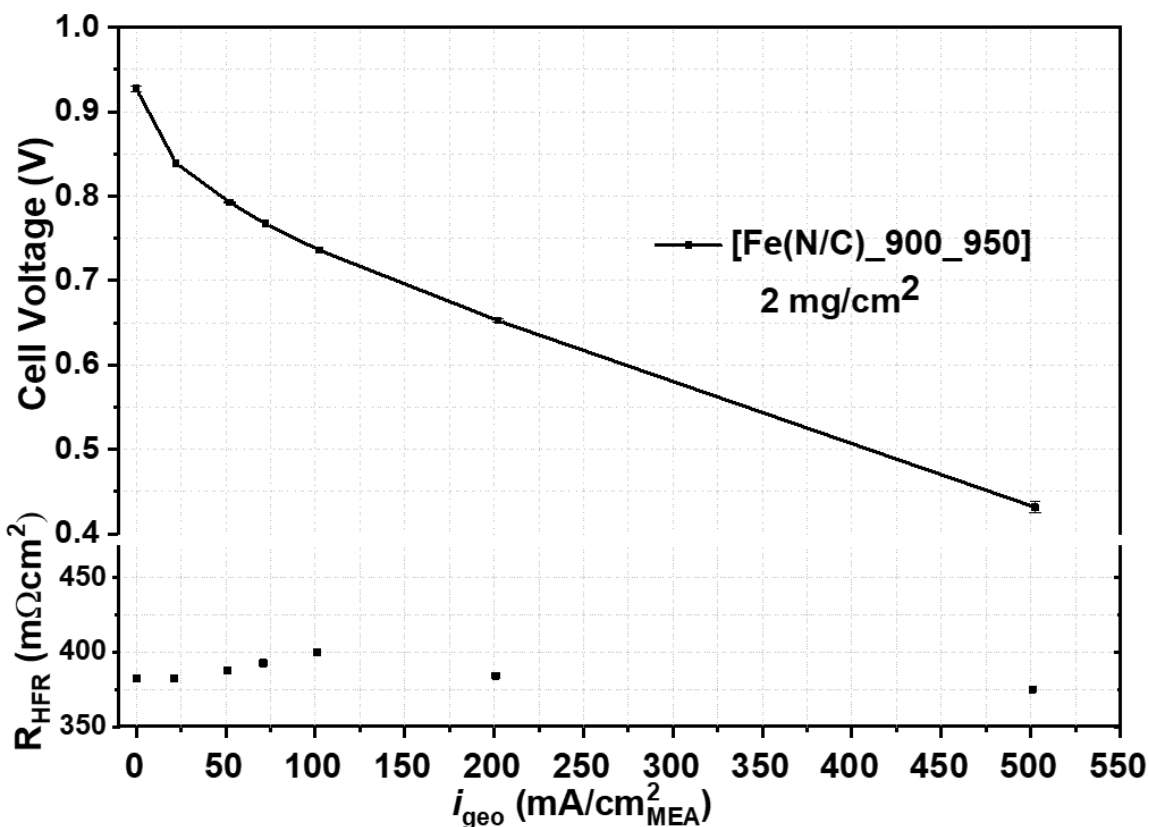


Figure 2.2.9: Single cell test results for $[\text{Fe}(\text{N}/\text{C})_{900_{950}}]$.

The comparison of the activity with Pajarito Powder is also given in Figure S2.2.9. The tests performed with the same catalyst loading and the conditions show that the performance is similar at low current density after iR loss correction however, the commercial catalyst outperforms at high current density region. It is noteworthy that high frequency resistance (HFR) obtained for $[\text{Fe}(\text{N}/\text{C})_{900_{950}}]$ is considerably high ($\sim 380 \text{ m}\Omega\text{cm}^2$) compared to the one for the commercial catalyst ($\sim 75 \text{ m}\Omega\text{cm}^2$). Moreover, the thickness of the electrodes made from these two catalysts show big differences. While the thickness of $[\text{Fe}(\text{N}/\text{C})_{900_{950}}]$ was measured as $120 \mu\text{m}$, the electrode of Pajarito Powder has half of the thickness.

Although the reasons behind the high HFR and thickness for [Fe(N/C_900_950)] need to be studied deeper, the synthesis approach shows promising results especially with low Fe content. Moreover, the optimizations for post-heat treatment as well as electrode preparation can improve the performance.

3. Heteroatom Doped Porous Carbons

3.1 Introduction

Heteroatom doping on carbon materials including graphene, graphite, carbon nanotubes, carbon clusters etc. attracted tremendous attention as doping, in most cases, improves the catalytic activity. The materials were named as 'Carbon Alloys' in Japanese research community since 1992 whereas it is known as 'Heteroatom Doped Carbons' in the international society. Paraknowitsch and Thomas reviewed the heteroatom doping on carbon (boron, sulphur, phosphorus) and summarized the effect of each heteroatom as well as dual/co-doping on the energy applications such as supercapacitors, Li-ion batteries and fuel cells.⁷⁰ Choi et al. specifically studied the binary and ternary doping and the ORR activities.⁷¹ They concluded that additional phosphorus doping increases the ORR activity by 100-108 % compared to solely nitrogen doping.

Porosity development is one of the most important steps for the synthesis of heteroatom doped carbon-based catalysts. Design of nanostructure of porous carbon materials can be made by various techniques such as activation, templating (hard/soft), activation and sol-gel methods.⁷² Especially in the field of catalysis, the small pores ($d < 100$ nm) and structure are often of interest in mass transport, thus control on the structure parameters during the pore formation is significant for rational design of such porous carbons.⁷³ State-of-the-art synthesis methods for heteroatom doping involve metal chlorides as porogen which leave metal traces in the structure after washing step. The presence of these metal traces even in ppm level leads to increased

activity, the understanding of the roles of heteroatoms in the carbon matrix becomes complicated, thus there is still lack of systematical investigation of doping process.

In this context, using a non-metallic porogen will help understand the effect of P-N doping on the ORR activity. Chemical activation with Brønsted acids is a promising approach for metal free synthesis and despite the pore generation without metal trace, heteroatom doping is possible at the same time with chemical activating agents such as phosphoric acid with high yields.⁷⁴⁻⁷⁵

However, the activation mechanism with Brønsted acids is often considered as leaching in the literature and the pore development is limited with some factors such as synthesis temperature and impregnation ratio. In this Chapter, the hypotheses given in Chapter 1.2 will be tested with first; from the mechanistic aspect and second; application on conductive carbon synthesis at high temperature.

3.1.1 Sol-Gel Process

Sol-gel method was first used in mid-1800 for the synthesis of inorganic ceramic and glass materials which then used also for organic material synthesis and well-studied over 200 years. The main advantages of sol-gel process are high-level homogeneity and size control of the primary particles which help tailor the nano-structure of the final material.⁷⁶ Later, the basic principle of sol-gel process was used in the synthesis of nanoporous carbons. Richard W. Pekala reported the synthesis of organic aerogels from the polycondensation of resorcinol with formaldehyde.⁷⁷ This reaction was investigated via different analytical techniques and the polymerization mechanism, structure and properties were found similar to sol-gel process.

Another analogous was reported for the synthesis of nanoporous carbons with inorganic salt melts (ionothermal methods) where the molten salts were used as solvent at high temperature.⁷² The carbons synthesized with sol-gel process possess a morphology similar to the commercial carbon supports that are used in the fuel cell application (Figure 3.1.1).

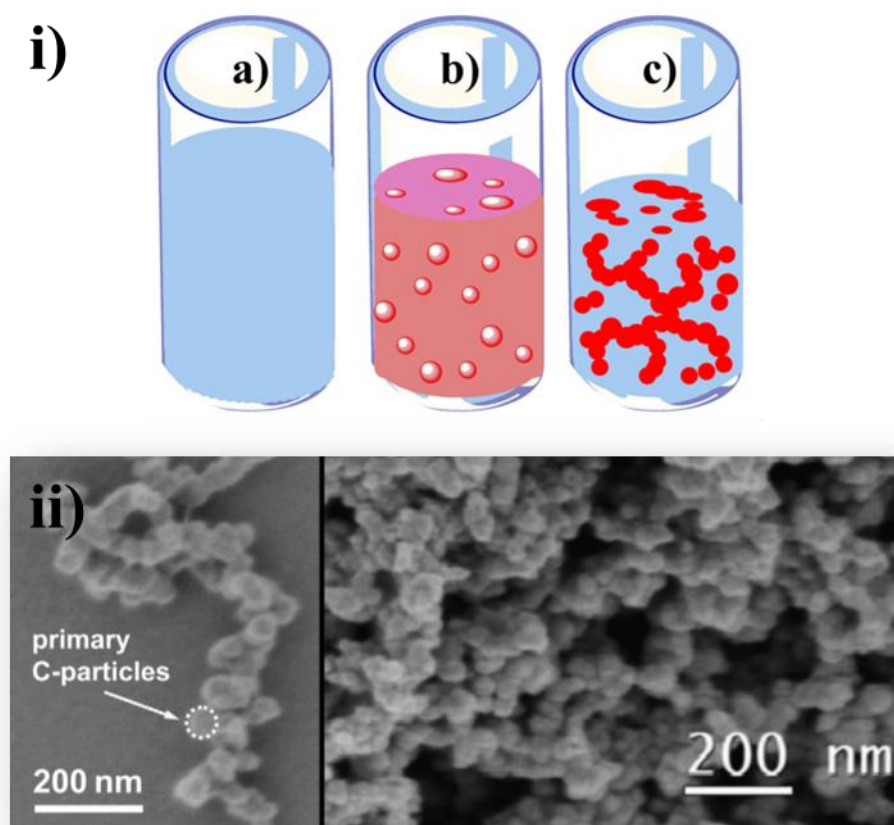


Figure 3.1.1: i) Steps of Sol-gel process⁷² and ii) the morphology of carbon black support
Republished with permission of IOP Publishing, Ltd, from ref 78; permission conveyed through
Copyright Clearance Center, Inc.

Although sol-gel provides numerous advantages, it is important to understand the fundamental mechanism of whole process. As depicted in Figure 3.1.1, sol-gel process proceeds with the dissolution of precursors in a solvent, polymerization/cross-linking, and carbonization followed by phase separation. In sol-gel process, the solvents act as porogen which are removed

subsequently and result in the formation of porosity. The most significant advantage of this method is porosity-controlled homogenous synthesis, thereby rational design of the materials. One simple way to tailor the porosity is altering the precursor-to-solvent ratio. Sols are defined as the dispersion of colloidal particles in a liquid/solvent and colloids are the solid particles with diameters of below 100 nm. A gel is disordered interconnected network formed as a result of cross linked/polymerized particles.

3.2 Results

3.2.1. Porosity Development with Brønsted acids

The use of phosphoric acid in the synthesis of porous carbon has been considered as chemical activation in the activation studies in which only a limited amount of phosphoric acid was used. The studies conducted on the development of porosity were based on the variation of H_3PO_4 concentration (or impregnation ratio) and synthesis temperature. These studies mostly focused on treatment of solid carbonaceous precursors (some lignocellulosic biomass like coconut, wood, peach stones *etc.*) due to the remarkable advantage of this industry on sustainable and renewable chemistry.²⁶

The main conclusion was similar for all the works and as conclusion, the excessive H_3PO_4 was reported to be ineffective for further development of the porosity, indeed decreasing the surface area and pore volume.^{28, 79-80} The reason was speculated as the formation of an insulating layer on the activated carbon with excessive amount of H_3PO_4 , thus preventing further porosity development.

The studies based on the limited H_3PO_4 concentration is denoted as a conventional synthesis in this thesis and represented in Figure 3.2.1a. Low impregnation ratio is illustrated as dispersion of acid in the carbon phase and subsequent washing step leads to typically micropore formation. Furthermore, the conventional H_3PO_4 activation was reported to proceed in the different chemical transformation steps: i) depolymerization, ii) dehydration, iii) redistribution (cross-linking/polymerization).^{29, 81-82} The impregnation of activating agent into the carbon precursor is the first step and mostly carried out at relatively low temperatures and the acid attacks to the precursor (depolymerization). Subsequently, elimination of water (dehydration) is observed at slightly elevated temperatures followed by cross-linking (redistribution) by means of ether, phosphate or polyphosphate groups.⁸²⁻⁸⁴

The pore formation steps reported in the literature for conventional chemical activation are based on the low impregnation ratio of chemical activating agent. Herein we investigate the mechanism of H_3PO_4 activation process developing hypotheses and employing Brønsted acids as high temperature solvents as well as varying the precursor-to-solvent ratio. According to our hypothesis, carbon becomes the dispersed phase with excess amount of acid used in the synthesis (Figure 3.2.1.b). Furthermore, our hypothesis addresses the temperature and porosity relationship. In our assumption, the temperature limitation often reported in the literature is related to the evaporation of the acid, as the removal of the porogen causes the contraction of the pores.

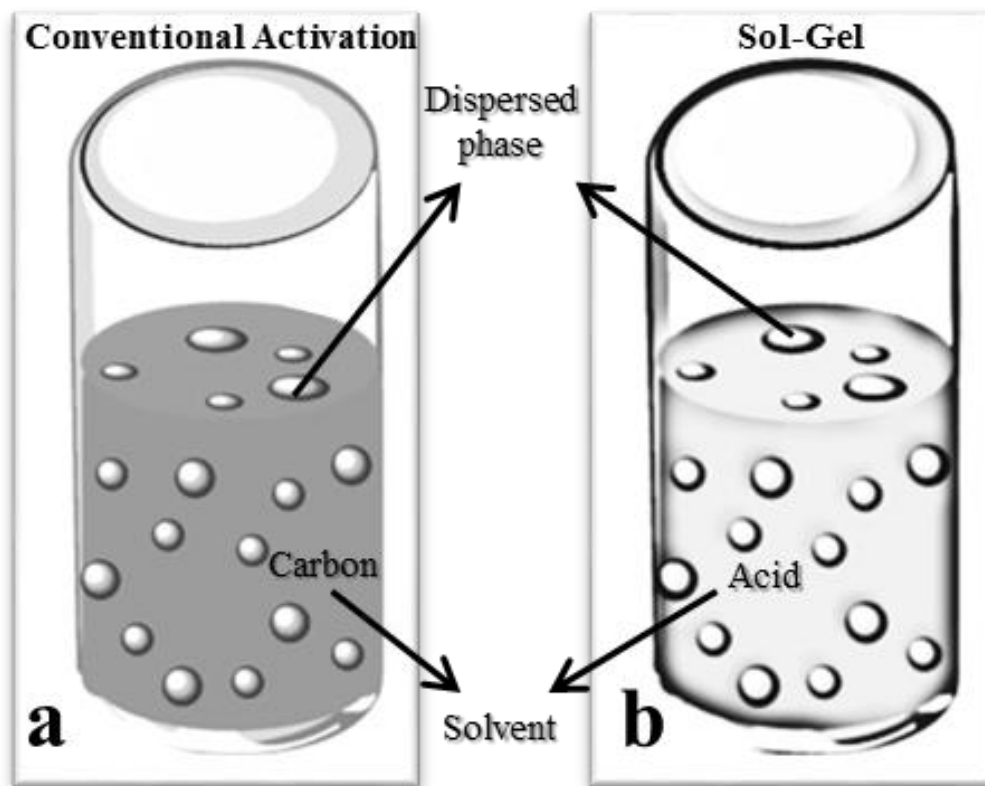


Figure 3.2.1: Illustration of; a) Conventional Activation, b) Sol-Gel Method.

As the boiling point/evaporation of solvent is the limiting factor for the activation in our hypothesis, water-free solvents were selected with different types of precursors: molecular, polymeric and lignocellulosic. We aim to elucidate the role of solvent-precursor pair together with the dehydration step during the pore formation by selection of the oxygen free polymeric precursor. Therefore, we test our hypotheses, first on the molecular precursor (glucose), then oxygen free polymeric precursor (polyaniline) and finally on lignocellulosic biomass.

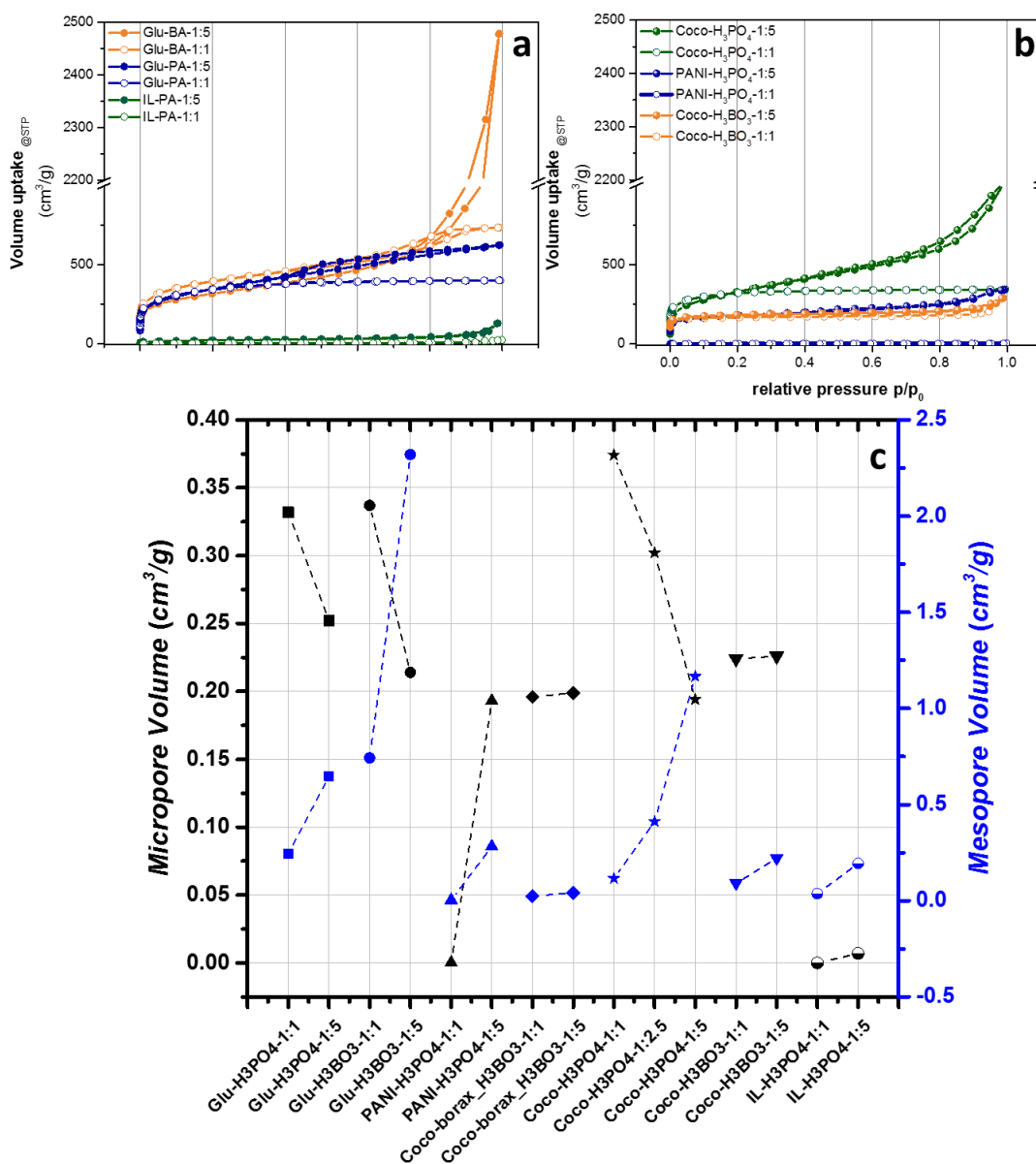


Figure 3.2.2: N₂ sorption isotherms of molecular precursors (a) and polymeric precursors (b) and the change in the micropore and mesopore volumes with solvent amount (c).

N₂ sorption isotherms shown in Figure 3.2.2 indicate different types of porosity for each pair of solvent-precursor and ratio. Among the molecular precursors (Table 4.1.1), glucose exhibits decent porosity and a clear trend between the shape of isotherm and precursor-to-solvent ratio. Glu-PA-1:1 has a type I isotherm with late completion of monolayer (point B)⁵⁶ indicating a

microporous structure that has a major contribution of supermicropores (0.7-2 nm).⁵⁷ Increasing the solvent-precursor ratio from 1:1 to 1:5 yields to a change in the type of isotherm from type I to mixed type I and type IV isotherm. This change is originated mainly from the formation of mesopores with higher solvent amount. Similar fashion was observed for Glu-BA and IL-PA but in a different scale. For some precursors, 1:1 ratio was not enough for dissolution of precursor in the solvent, thus insufficient porosity was obtained (IL-PA-1:1, PANI-H₃PO₄), yet the remarkable increase in the porosity was achieved using 1:5 ratio. The solvent-precursor interaction effects the final pore structure and results in distinct micro- and mesopore distribution (Figure 3.2.2c). Nevertheless, increasing solvent amount leads to development of mesopores and reduction of micropores. The pore size distribution (Figure 3.2.3) and textural properties of the carbons (Table 3.2.1) also demonstrate these changes together with the other pore properties such as total pore volume.

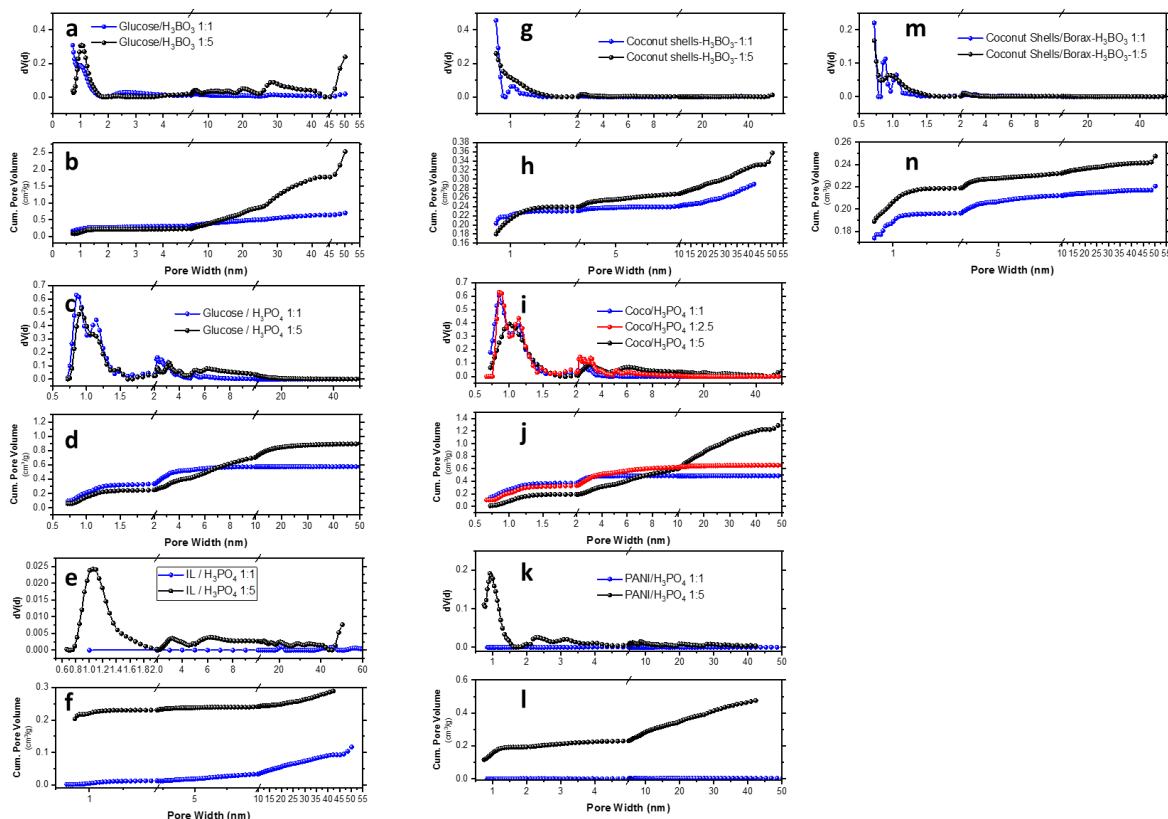


Figure 3.2.3: N₂ sorption derived pore size distributions and cumulative pore volumes of molecular precursor derived carbons: a,b) Glu-H₃BO₃; c,d) Glu-H₃PO₄; e,f) IL-H₃PO₄. Pore size distributions and cumulative pore volumes of polymeric precursor derived carbons: g,h) Coco-H₃BO₃; i,j) Coco-H₃BO₃; k,l) PANI-H₃PO₄; m,n)) Coco-borax_H₃BO₃.

The morphology and porosity were further studied with transmission electron microscopy (TEM) and scanning electron microscopy (SEM). TEM and SEM images (Figure 3.2.4) depict the presence of meso and macropores in the structure of the carbons synthesized with high solvent-to-precursors ratio (1:5). Furthermore, the images confirm the trend observed in N₂ isotherms in such way that the higher solvent content leads to formation of bigger pores. The findings are pointing out an unusual mechanism compared to the conventional chemical activation process. The pore formation with high solvent amount is no longer an impregnation process but dispersion of the precursors in the molten acid. The TEM and SEM images also reveals the interstitial porosity between aggregated primary carbon particles rather than simple

impregnation. This unusual mechanism for chemical activation indeed resembles to sol-gel process which starts with dissolution of the precursor in the solvent and ends with phase separation after carbonization. The pore volumes extracted from N_2 isotherms also increase with higher solvent amount indicating the further phase separation with the solvent.

The utilization of molecular precursors (glucose and ionic liquid) for pore formation shows the dissolution of the precursors in the solvent followed by carbonization and phase separation. However, as expected, different precursors lead to varied porosity due to distinct solubility of each precursors in each solvent. In the case of glucose, although the surface area of the carbons obtained by using H_3PO_4 and H_3BO_3 are similar, the total pore volume and the mesopore volume that is the bigger contributor of the total pore volume are altering strongly. The most obvious difference of these Brønsted acids is the boiling point which significantly affect the final porosity. The lower boiling point of H_3PO_4 causes higher losses due to the evaporation at high temperature despite the chemical transformation and subsequently less porosity. The other factor might be the difference in the density of two acids. Since the lower density is expected to create bigger void volumes H_3BO_3 results in the pore volume of $2.534 \text{ cm}^3/\text{g}$ which is 2.8 times higher than Glu- H_3PO_4 synthesized with the same solvent amount (Table 3.2.1).

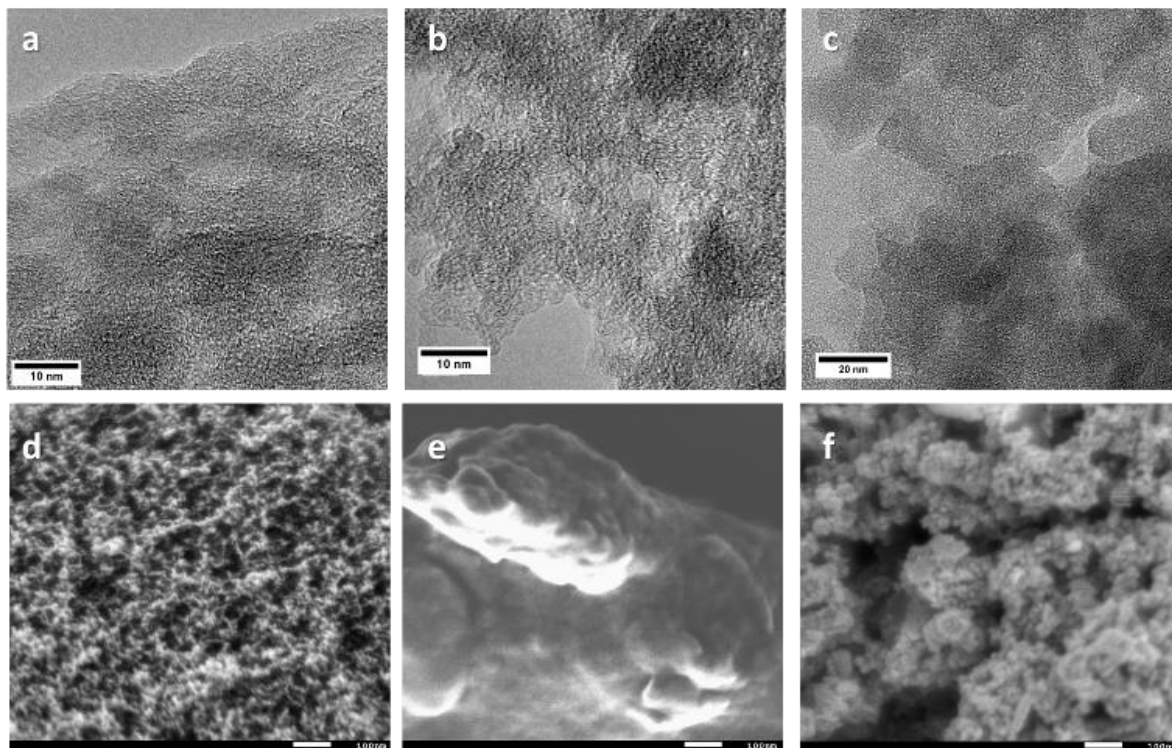


Figure 3.2.4: TEM (a-c) and SEM images (d-f) of the carbons synthesized with high solvent amounts from molecular precursors; a, d) Glu- H_3BO_3 -1:5; b, e) Glu- H_3PO_4 -1:5; c, f) IL- H_3PO_4 -1:5. The scale bar for SEM images is 100 nm.

The dehydration step reported in traditional activation mechanism was investigated by selection of oxygen-free precursors such as ionic liquid (IL) (EMIM-dca) and polyaniline (PANI). IL and PANI precursors also represent molecular and polymeric precursors, respectively. The low solvent amount results in non-porous carbon (Figure 3.2.2 a,b) for both precursors. The specific surface areas (SSAs) obtained with 1:1 precursor-to-solvent ratio are 7 and 2 m^2/g for IL and PANI samples and there is no micropore volume detected using N_2 sorption. Therefore, CO_2 sorption technique was used to probe ultramicropores (<0.7 nm) which are not accessible to N_2 molecules at very low temperature (77 K). CO_2 sorption at 273 K revealed the formation of small pores even with low precursor-to-solvent ratio (Figure 3.2.5). However, increased solvent amount brings more porosity to both IL and PANI samples despite the absence of oxygen in

the structure of precursors, thus no dehydration involving in the mechanism. Furthermore, the yields obtained for PANI-H₃PO₄ samples (Table S3.2.1) show unusual trend for traditional activation (Figure 3.2.1), namely increasing yield with more porosity and precursor amount. This finding points to a catalytic effect of H₃PO₄ on carbonization, which is the opposite of leaching. Similar to the previous findings, the amount of solvent required for the formation of pores varies depending on the precursor-solvent pair. TEM images (Figure 3.2.6) depict the sol-gel-type structure of aggregated primary particles forming interstitial pores. The porosity development with the precursors that do not have ether bonds points out a physical process (swelling) rather than a chemical process (hydrolysis). The absence of the dehydration step during the pore formation indicates a different mechanism than conventional impregnation method (Figure 3.2.1).

We further tested our hypothesis and findings on coconut shells which is a type of lignocellulosic biomass and composed of one third of lignin and two thirds of polysaccharides.⁸⁵ Two types of solvents were used in order to elucidate the solvent-precursor effect and porosity development. N₂ isotherms of the carbons reveal different porosity developments for each solvent-precursors pair which is again originated from different solubilities of coconut shells in H₃PO₄ and Borax_H₃BO₃. Better solubility of coconut shells in H₃PO₄ results in 5.6 times higher total pore volume for the same precursor-to-solvent ratio (1:5). Furthermore, a clear trend is again observed between the solvent amount and porosity. Coco-H₃PO₄-1:1 exhibits a Type I isotherm indicating the microporous structure and changes with the solvent amount. Micropore volume decreases to 0.302 and 0.194 with 1:2.5 and 1:5 precursor-to-solvent ratio from 0.374 cm³/g (1:1).

Table 3.2.1: Textural properties of molten acid derived carbons.

Sample Name	SSA (m²/g)	MiPV (cm³/g)	MePV (cm³/g)	TPV (cm³/g)	Average PS (nm)
Glu-H₃PO₄ - 1:1	1171	0.332	0.243	0.575	0.85
Glu-H₃PO₄ - 1:5	1141	0.252	0.648	0.900	0.93
Glu-H₃BO₃ - 1:1	1350	0.337	0.743	1.080	0.93
Glu-H₃BO₃ - 1:5	1134	0.214	2.320	2.534	1.05
IL-H₃PO₄ -1:1	7	-	0.037	0.037	-
IL-H₃PO₄ -1:5	72	0.007	0.194	0.201	1.05
Coco-H₃PO₄ - 1:1	1199	0.374	0.116	0.490	0.85
Coco-H₃PO₄ - 1:2.5	1275	0.302	0.412	0.714	0.85
Coco-H₃PO₄ - 1:5	990	0.194	1.166	1.360	1.00
Coco-H₃BO₃ - 1:1	655	0.224	0.091	0.315	0.79
Coco-H₃BO₃ - 1:5	700	0.226	0.221	0.447	0.79
PANI-H₃PO₄ - 1:1	2	0.000	0.004	0.004	-
PANI-H₃PO₄ - 1:5	733	0.193	0.282	0.475	0.93
Coco-borax_H₃BO₃- 1:1	724	0.196	0.024	0.220	0.72
Coco-borax_H₃BO₃- 1:5	758	0.199	0.041	0.240	0.72

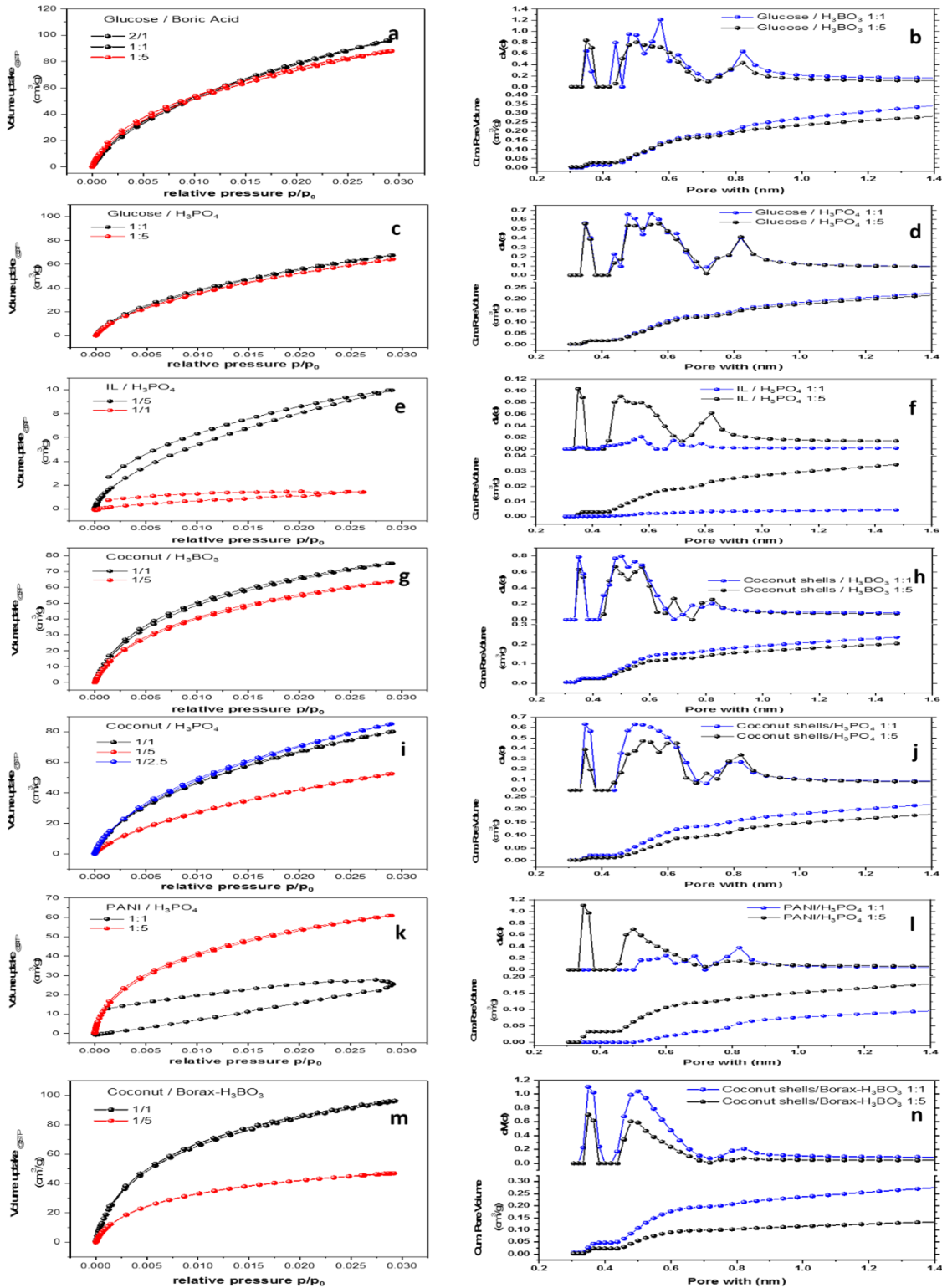


Figure 3.2.5: CO₂ sorption isotherms, pore size distributions and cumulative pore volumes of molecular precursor derived carbons: a,b) Glu-H₃BO₃; c,d) Glu-H₃PO₄; e,f) IL-H₃PO₄. Pore size distributions and cumulative pore volumes of polymeric precursor derived carbons: g,h) Coco-H₃BO₃; i,j) Coco-H₃BO₃; k,l) PANI-H₃PO₄; m,n) Coco-borax_H₃BO₃.

The mechanistic study reveals that the utilization of excess amount of Brønsted acids act as solvent rather than a chemical leaching agent which is often defined in conventional chemical activation. We tested our hypothesis using various carbon precursors, namely molecular, polymeric and biomass like precursors, and Brønsted acids solvents. Porosity measurements showed that increasing the amount of Brønsted acids resulted in more mesoporous/macroporous structure due to the better dissolution of the carbon precursors in the acids. Unlike the traditional chemical activation process where the chemical agent is impregnated into the precursors, excess amount of acid acts as solvent. Furthermore, we investigated the mechanism using oxygen free precursors (IL and PANI) and again excess amount of solvents, and elucidated a different mechanism than a conventional chemical in which dehydration takes place. In addition, the yields obtained from our synthetic approach do not fit to the porosity-yield relation that is usually reported in the literature with impregnation method as H_3PO_4 has a catalytic effect on carbonization, thus increasing amount results in higher yields. According to our results, the pore formation using excess amount of Brønsted acids deviates from a simple chemical activation and resembles to sol-gel method. These findings do not only show a new mechanism but also provides a high control on porosity.

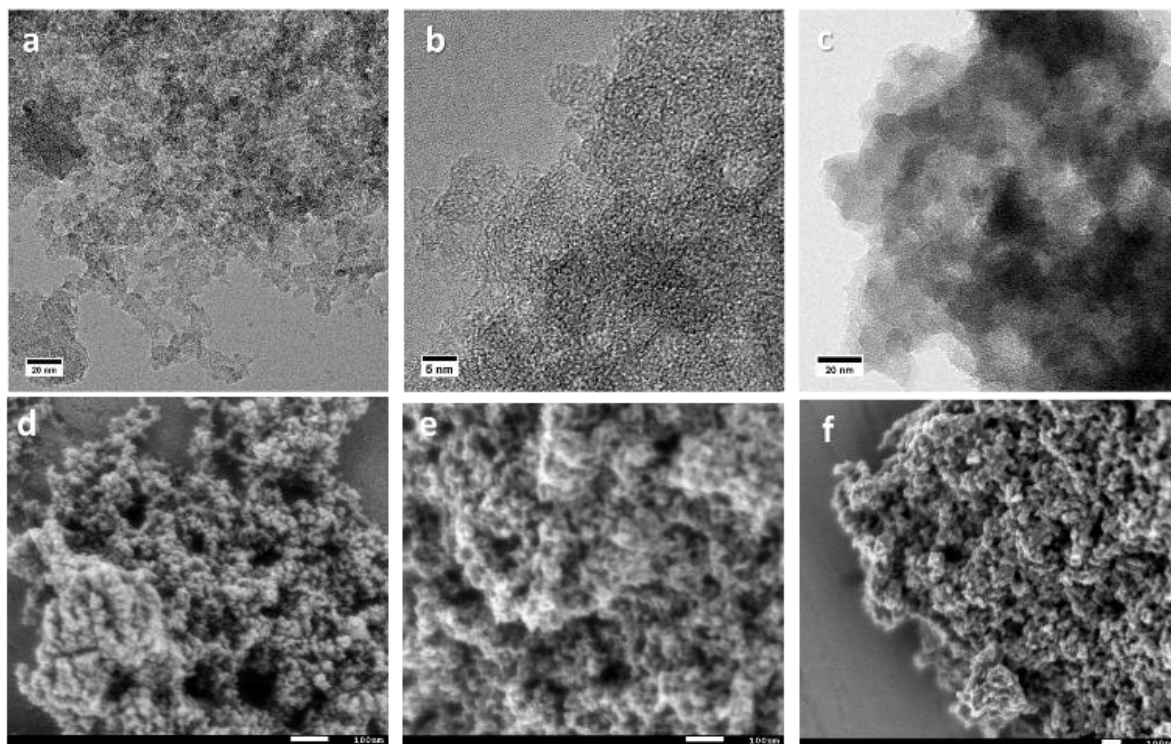


Figure 3.2.6: TEM (a-c) and SEM images (d-f) of the carbons synthesized with high solvent amounts from polymeric precursors; a, d) Coco-H₃BO₃-1:5; b,e) Coco-H₃PO₄-1:5; c,f) PANI-H₃PO₄-1:5. The scale bar for SEM images is 100 nm.

3.2.2. High Temperature Synthesis

The study on pore formation mechanism provides a deeper understanding for activation process and opportunity for tunable porosity in the synthesis of porous carbons. As market volume of activated carbons was estimated as 4.73 billion USD for 2018 and an increase was expected within next years (5.12 billion USD by 2022), certain technical developments in terms of synthesis and application are required. Facile synthesis methods as well as task specific products are becoming more interesting especially for certain fields such as gas storage/separation, catalysis.

In electrochemistry, conductive porous carbons play important role as either support materials or even catalysts. The synthesis of electrically conductive carbon materials require high temperature treatment. However, the porosity formation and the heat treatment are two competing processes as high temperature causes the collapse of the pores, particularly in the absence of porogen or throughout evaporation/boiling of porogen. Although chemical activation is a suitable process for the synthesis of porous carbons with well-established industry, temperature limitation of certain chemical activating agents hamper the synthesis of conductive carbons.

Apart from the pore formation, heteroatom doping plays important role in the electrochemistry as mentioned in Chapter 3. Heteroatom doped carbons have been widely studied as alternative catalyst for ORR in fuel cell since tuning the electronic structure of carbon gives rise to the higher activity/durability.⁸⁶ Although nitrogen was the first candidate due to its ability of charge redistribution and the chemical convenience of doping, various heteroatoms such as boron, phosphorus and sulfur were studied in the literature. While each single heteroatom has different

chemical effects on the carbon matrix, recent studies focused on binary and ternary doping with nitrogen.⁷⁰ Among the others, phosphorus has the makings of an alternative for nitrogen or heteroatom for dual doping with nitrogen due to the same number of valence electron. In acidic medium, the study by Choi et al. revealed that the additional P-doping increases the ORR activity by 100-108 % in binary and ternary doped carbons. They concluded that P doping increases the charge delocalization of the carbon atoms and leads to open edge sites.⁷¹ Despite the considerable activity increase, heteroatom doped metal free catalysts are not comparable to Pt yet in acidic medium. However, Zhang et al. calculated the activation energy for rate-limiting step for ORR in alkaline and reported that P,N doped carbons could show electrochemical activities comparable to Pt.⁸⁷ Also, it was reported that the incorporation of phosphorus into the network of graphene sheets led to higher onset potential than Pt/C and better stability in alkaline medium.⁸⁸

H₃PO₄ is one of the chemical agents that has been extensively studied in the literature yet with biomass-like precursors such as peanut hulls, almond shells, pecan shells, corncob, coconut shells, bamboo waste, date stone.⁸⁹⁻⁹¹ However, the temperature limitation of conventional H₃PO₄ activation that is mostly reported as 350-450 °C prevents the preparation of conductive carbons.^{30, 81-82} Although H₃PO₄ is a unique porogen and chemical for P-doping into carbon matrix, high temperature utilization and tailorable porosity at elevated temperatures are the obstacles for heteroatom doped carbon synthesis for electrochemical applications.

Introducing phosphorus in the carbon matrix by preserving the conductivity and controlling the porosity at the same time is a challenging process. In the literature, often pyhtic acid is used as phosphorus dopant. Li et al. synthesized a P-N doped carbon using pyhtic acid as both phosphorus dopant and gelation agent during polymerization. Polymerization of aniline in the

presence of phytic acid and subsequent carbonization resulted in mainly microporous structure, therefore graphene oxide was used as structure-directing agent.⁹² In a similar work, Zhang et al. employed phytic acid and obtained the catalysts with in situ polymerization.⁸⁷ Also, in situ activation of PANI with H₃PO₄ resulted in limited temperature as 800 °C and decent porosity.⁹³

In our mechanistic study, we provided a route to tailor the porosity similar to sol-gel process. Moreover, we achieved decent porosity at relatively high temperature compared to conventional activation. However, conductive carbon synthesis requires higher temperatures. In this chapter, extension of this study to higher temperature for conductive carbon synthesis and electrochemical application will be covered.

The investigation of the active sites formation for ORR at elevated temperatures was historically started with heat treatment of phtalocyanine/porphyrin type macrocycles and in 1989 Gupta et al. reported that the heat treatment of polyacrylonitrile results in formation of active sites as well.³⁸ Since then, numerous publications reported that the high temperature heat treatment of metal, carbon and nitrogen precursors leads to formation of MeN₄ motifs similar to pophyrin/phtalocyanine.⁹⁴ This square planar motif can be obtained by certain metals such as Mg, Fe, Co, Mn and also nonmetal such as phosphorus. Indeed, phosphorus is the first nonmetal that occupies the porphyrin ring.⁹⁵ However, the presence of this motif with phosphorus at high temperature was never reported.

The synthesis was carried out as explained in Chapter 6. The high temperature synthesis was aimed by utilization of water-free H₃PO₄ to minimize loss of H₃PO₄ during the pore formation as water content facilitates the volatilization of the acid, thus limits the temperature of pore formation. Also the formation of *meta*-phosphoric acid (HPO₃) and glassy polyphosphoric acid (H_{n+2}P_nO_{3n+1}) at high temperatures slows down the evaporation.⁹⁶ Additionally, we employed

water free polymeric and molecular carbon and nitrogen precursors, PANI and IL (EMIM DCA). In the light of our previous results, the precursor-to-solvent ratios of 1:5 and 1:10 were used for PANI_ H₃PO₄ and IL_ H₃PO₄, respectively. As a results of delayed evaporation, the heat treatments at 800 °C and 1000 °C lead to highly porous structure despite the long dwelling time (3 h).

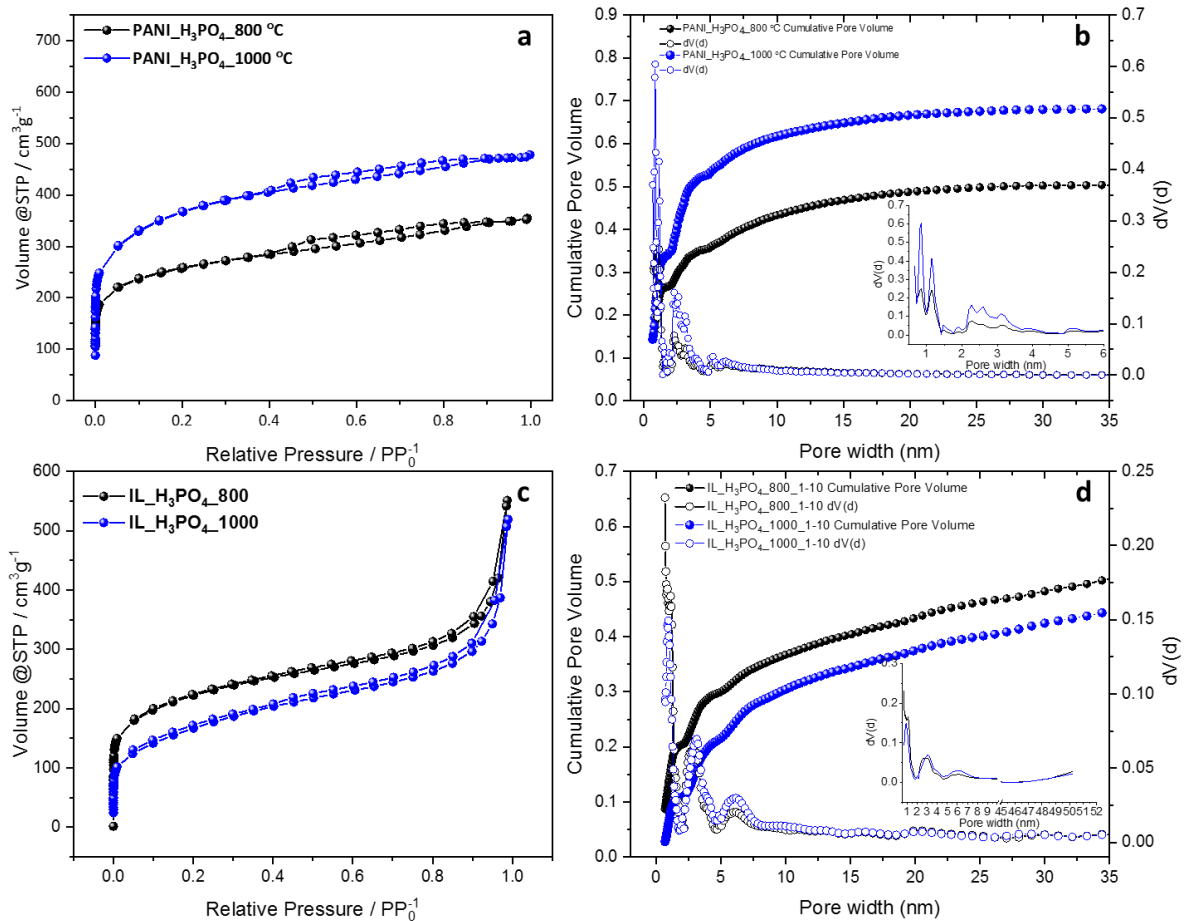


Figure 3.2.7: N₂ Isotherms and pore size distribution of PANI_H₃PO₄ (a, b) and IL_H₃PO₄ samples (c, d): 800°C (black), 1000°C (blue).

Table 3.2.2: Textural properties of the samples.

Sample	SSA (m ² /g)	S _{micro} (m ² /g)	V _{micro} (cm ³ /g)	V _{meso} (cm ³ /g)	V _{total} (cm ³ /g)
PANI_H₃PO₄_800	936	813	0.26	0.25	0.55
PANI_H₃PO₄_1000	1312	951	0.34	0.34	0.74
IL_H₃PO₄_800	789	566	0.20	0.40	0.85
IL_H₃PO₄_1000	586	268	0.10	0.43	0.80

The N₂ sorption isotherms illustrate the carbons with hierarchical pore structure (Figure 3.2.7). The steep increase at very low p/p₀ indicates the filling of micropores. The presence of micropores is expected as the conventional chemical activation causes mostly microporous materials. However, the slope at higher relative pressure range shows the development of mesopores for both precursor-solvent pairs. PANI_H₃PO₄ samples have Type IV isotherm that is characteristic for micro and mesoporous structures. The plateau at p/p₀≈1 also indicates the absence of macropore contribution. SSAs of these samples are relatively larger as the contribution of micropores are more pronounced. This is caused by probably the relatively high solubility of PANI in H₃PO₄. Increasing the temperature from 800°C to 1000°C leads to higher uptake value, thus larger SSA in PANI_H₃PO₄. Although V_{micro}, V_{meso}, and TPV increase with temperature (Table 3.2.2), the pore size qualitatively remain same. Similar behavior was observed by Kobayashi et al. in the carbonization of folic acid with phosphoric acid above 800 °C.⁹⁷

IL_H₃PO₄ show mixed type II/type IV isotherms indicating micro-, meso- and macroporous structure. The contribution of macro- and mesopores are clearly seen in TPV (Table 3.2.2). Despite the lower SSAs, TPVs are higher for IL_H₃PO₄ which might be originated from higher

solvent content (1:10). The effect of temperature on pore size distribution is similar to PANI_H₃PO₄ resulting in the same size of pores with different quantities.

CO₂ measurements were conducted to elucidate the development of ultramicropores ($d < 0.7$ nm). Both samples show remarkable CO₂ uptakes (Figure S3.2.1) and follow the trend similar to N₂ isotherms. IL_H₃PO₄_800 exhibit higher CO₂ uptake than IL_H₃PO₄_1000 whereas PANI_H₃PO₄_1000 have higher uptakes than PANI_H₃PO₄_800. It is noteworthy that IL-derived samples exhibit hysteresis in CO₂ isotherms unlike the PANI-derived samples. The hysteresis indicates higher binding energy of CO₂, indicating possibly chemisorption of CO₂ on these carbons. This distinct sorption feature might be due to the specific functionalities on the surface of IL-derived samples.

The isotherms for both type of samples point out usual sol-gel mechanism. A further morphological investigation helps to gain deeper understanding. SEM images (Figure 3.2.8) show aggregated particle for all the samples. The same behavior was observed also in mechanistic study. SEM images also reveal the different shapes of the particles, namely more spherical for PANI_H₃PO₄ and coil shaped for IL_H₃PO₄. TEM images show different interstitial pores for each type of carbons (Figure 3.2.8). PANI_H₃PO₄ samples have less interstitial pores and denser aggregation compared to IL_H₃PO₄. The macropores observed for IL_H₃PO₄ can be explained by higher amount of solvent used in the synthesis. High-resolution TEM (HRTEM) images exhibit disordered carbon sheets for both types of samples and absence of crystalline species that might be derived from phosphoric acid at high temperature. PXRD patterns (Figure S3.3.2) also confirm that the samples are amorphous and free of crystalline phases.

TG-MS experiments were designed to elucidate the porosity generation upon heat treatment. The experimental synthesis conditions were mimicked using the same heating rate, dwelling time and gas type. PANI_H₃PO₄ and IL_H₃PO₄ samples synthesized at 800 °C were subjected to heat treatment up to 1000 °C and the gas evolutions were monitored.

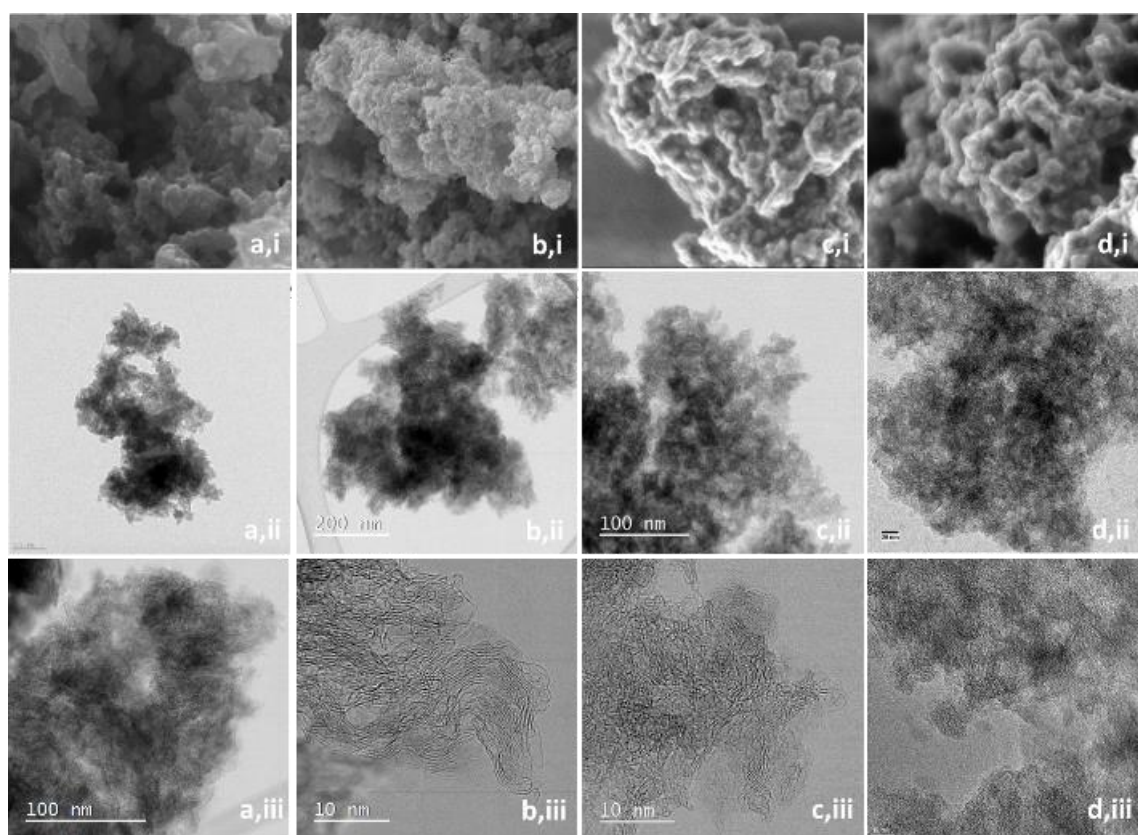


Figure 3.2.8: SEM and TEM images of a) IL_H₃PO₄_800°C, b) IL_H₃PO₄_1000°C, c) PANI_H₃PO₄_800°C, and d) PANI_H₃PO₄_1000°C.

The evolution of the physisorbed species such as O₂ (16), N₂ (28) and H₂O (18) continues even until 250 °C as a result of large surface area and high porosity of the carbons (Figure S3.3.3). The delayed desorption indicates the high affinity by the synthesized carbons towards adsorption of these gases. Heteroatom doped carbons have already reported to have high

adsorption capacities towards Lewis Acids which can also be confirmed by our CO₂ sorption measurements.⁹⁸⁻¹⁰⁰ Also, the hydrophilic character of the carbons due to the various functional groups support the H₂O adsorption. Indeed, these high affinities can be seen in MS profile (Figure S3.3.4). Although, H₂O (18) signal shows a peak around 250 °C, CO₂ and N₂ signals increase even after 800 °C where evolved gas comes from the structure rather than physisorbed gases. The MS profiles for PANI- and IL-derived carbons show similarities except a slight shift in temperature values. While the characteristic peaks for PANI-derived sample is observed at 863 °C, it is found at 890 °C for IL-derived sample. Also, the peaks assigned for PN, PC and P (m/z = 45, 43 and 31) reveal the PN-doped carbon scaffold. The profile of NO (30) is interestingly increasing even at higher temperature as an indication of removal of functional groups and increase in graphitization degree.

The graphitization degree can be monitored by Raman spectroscopy. D and G vibrational modes are used to evaluate the graphitization and disordered fraction in the carbon.¹⁰¹ We investigated the effect of carbonization on the graphitization degree by deconvoluting the peaks and evaluating D-to-G ratio (Figure S3.3.2). The D-to-G ratios go down by 19% for IL-derived carbons and 13% for PANI-derived carbons by increasing the temperature from 800 °C to 1000 °C. These results are also related to the crystallite size change by temperature.¹⁰² Our results also show that IL-derived carbons have less degree of graphitization compared to PANI-derived samples.

The surface characteristics were studied by XPS for each type of carbon. The survey spectra reveal the presence of C, O, N and P atoms (Figure S3.3.5) pointing out various functional group as well as doped N and P atoms. The concentration of these atoms are given in Table 3.2.3. Accordingly, N and P concentration decrease upon temperature increase for both PANI-

and IL-derived carbons. Interestingly, O concentrations decreases in PANI_H₃PO₄ with temperature whereas it remains same in IL_H₃PO₄.

Table 3.2.3: Surface composition (at.%) of the samples.

Sample	C	O	N	P	O/C	P/N
PANI_H ₃ PO ₄ _800	84.92	10.57	2.64	1.87	0.12	0.71
PANI_H ₃ PO ₄ _1000	88.76	8.69	1.67	0.88	0.10	0.53
IL_H ₃ PO ₄ _800	82.26	12.27	3.82	1.65	0.15	0.43
IL_H ₃ PO ₄ _1000	85.30	12.44	1.54	0.74	0.15	0.48

The high resolution spectra give insight into the chemical state of the respective atoms. Therefore, N1s and P1s spectra are deconvoluted for each species (Figure 3.2.9 and Figure S3.3.6). The peaks at binding energies of 398.3, 400.9, 402.1 and 403.5 eV are commonly assigned to pyridinic, pyrrolic, graphitic and oxidized nitrogen species, respectively.¹⁰³⁻¹⁰⁵ There is also a clear shoulder at lower binding energies for each sample which reveals another peak between pyrrolic and pyridinic. This shape was often reported in the literature for P-N doped carbons as well.^{93, 106} We assign this peak to P-N bond as a result of the comparison with the reference material (phosphorus phtalocyanine) and P₃N₅.^{107, 108} The contribution of this bond to overall N1s is more pronounced at low temperature showing a consistency with TG-MS results. The majority of the N species are pyrrolic for both PANI- and IL-derived samples and the concentration exhibits a similar trend with temperature (Table 3.2.4).

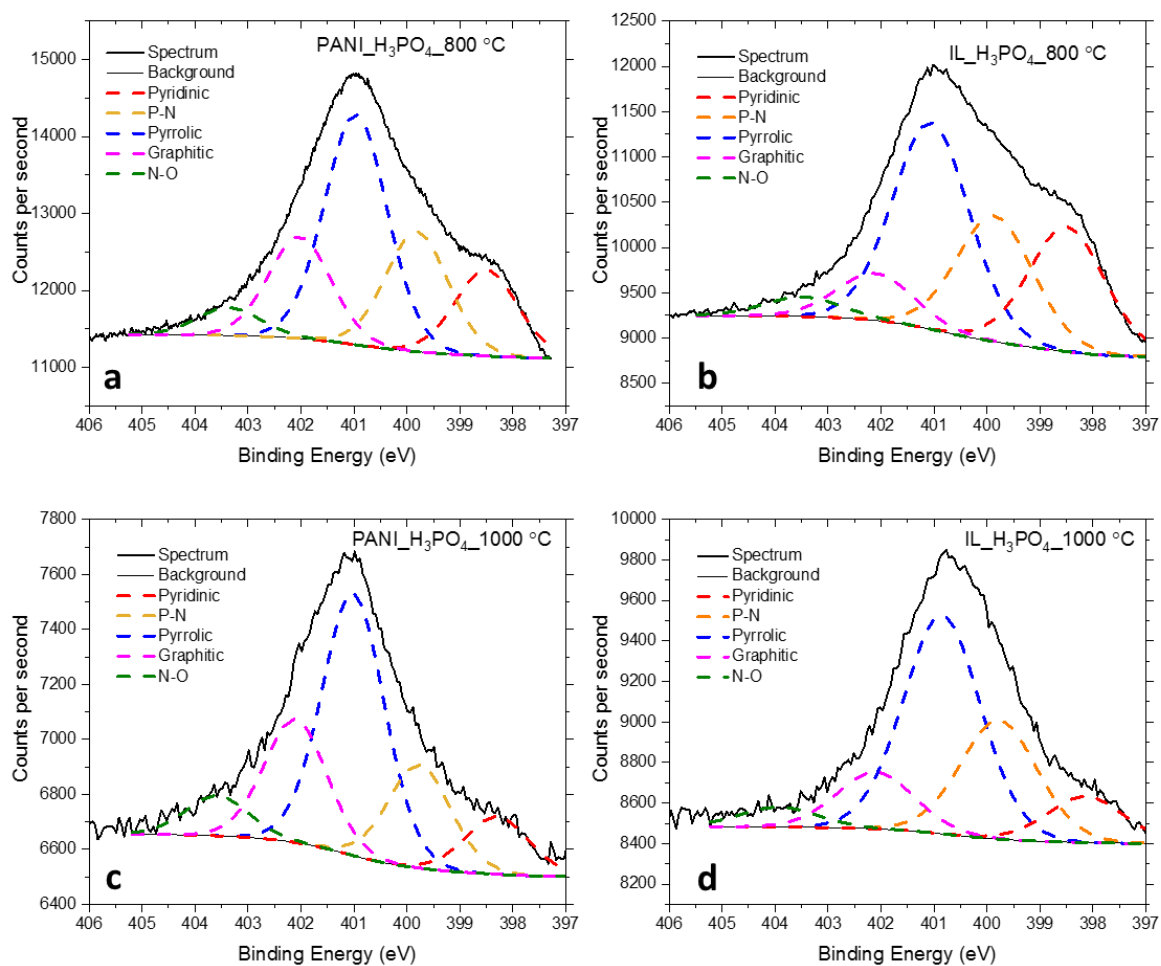


Figure 3.2.9: Deconvoluted N1s XPS spectra of a) PANI_H₃PO₄_800 b) IL_H₃PO₄_800 c) PANI_H₃PO₄_1000 and d) IL_H₃PO₄_1000.

Table 3.2.4: The concentration of Nitrogen and Phosphorus species in IL- and PANI-derived samples.

Sample	N (at.%)						P (at.%)			
	Pyridinic	N-P	Pyrrolic	Graphitic	N-O	Total	P-C	P-N	P-O	Total
PANI_H ₃ PO ₄ _800	0.54	0.74	1.43	0.63	0.17	3.51	0.84	1.17	0.41	2.42
PANI_H ₃ PO ₄ _1000	0.16	0.31	0.74	0.36	0.10	1.67	0.43	0.3	0.12	0.87
IL_H ₃ PO ₄ _800	0.85	0.94	1.63	0.43	0.15	4.00	0.73	0.81	0.25	1.79
IL_H ₃ PO ₄ _1000	0.16	0.41	0.75	0.19	0.07	1.58	0.32	0.36	0.08	0.76

The presence of various surface functional groups and evolution of different moieties point out diversified motifs as well as distinct stability range of these motifs. To elucidate these motifs and particularly the thermodynamically stable ones, DFT calculations were performed at Technical University of Berlin by Jian Liang Low as a part of master thesis in Prof. Paulus group.

The relative stability was determined by comparing binding energy of P (E_B) and the energy needed to break P-N bond (E_{sep}). E_B were calculated according to the optimized structures of dissociated (C,N)₄ clusters and free P atom. E_{sep} calculations were performed by comparison of total energy of the respective motif with a convenient combination N-doped and undoped graphene cluster.

The most stable motif was found as trans-PC₂N₂ amid different type of configurations (Table 3.2.5). E_B value for PC₂N₂ (-7.54 eV) is more negative than the other P-N and PC₄ configurations pointing out stronger binding for PC₂N₂, thus more stability. The peak temperatures (863°C and 890 °C) found in TG-MS conceivably correspond to the decomposition/desorption temperature of P-containing motifs. Furthermore, calculations for E_{sep} values give positive numbers compared to the reference (PN₄) in each combination. In addition, trans-PC₂N₂ has a square planar geometry whereas PN₄ and PCN₃ have out-of-plane with a 0.6 Å distance between P and N₄ as well as P and CN₃.

Table 3.2.5: Binding energy of P, P-N separation energy, oxidation energy with respect to free O₂ and hydration energy with respect to free H₂O of various binding motifs.

Binding Motif	E_B (P) [eV]	E_{sep} [eV]	E_{ox} [eV]	E_{hyd} [eV]
PN₄	-4.36	0 (ref)	-3.21	-0.84
PCN₃	-6.13	+0.86	-3.27	-0.61
PC₂N₂	-7.54	+0.94	-2.50	-0.59
PC₃N	-7.05	+1.55	-1.52	-0.82
PC₄	-5.77	+3.58	-1.04	-0.98

The binding strengths of these motifs with O, OH and (OH)₂ as axial ligands were determined by the binding energy calculations (E_{ox} and E_{hyd}) for P atom (Table 3.2.6). The calculations were performed with respect to the reference molecules; O₂ triplet ground state for binding of O and free OH molecules for binding of OH and (OH)₂. For oxygen, the relative values exhibit a decrease from PN₄ to PC₄ indicating high affinity for PN₄ towards oxidation. This finding correlates with the increased activities of P/N-doped carbons compared to P-doped carbons.

Adsorption of OH groups as well as hydration of PO can lead to formation axial ligands on P/N doped carbon. Trans-PC₂N₂ has the highest binding energy for single OH binding according to calculations with respect to free OH molecules. The binding energies decrease with the order of PC₂N₂ > PCN₃ > PN₄ > PC₄ (Table 3.2.6, Figure 3.2.10). However, the order changes for the binding energies of second OH. PN₄ possesses the highest energy for the second OH, which might complete the octahedral geometry. In fact, octahedral geometry is often observed for porphyrin like structures, particularly FeNC catalysts and the presence of these ligands affect the ORR activity.¹⁰⁹⁻¹¹⁰

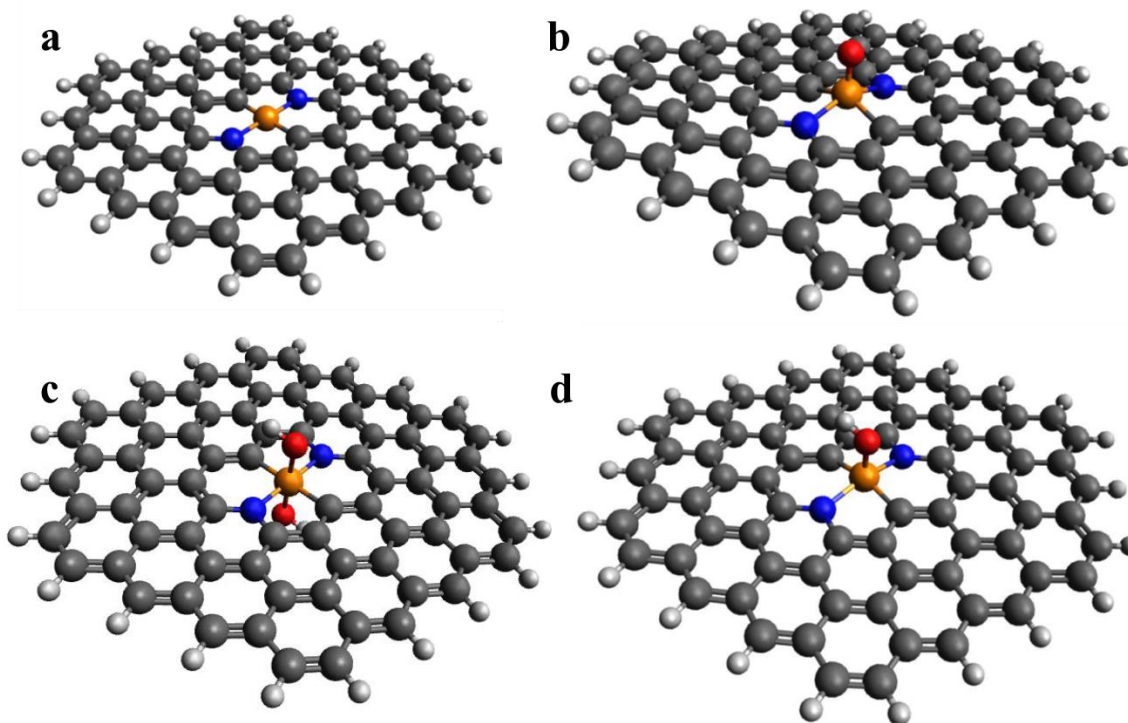


Figure 3.2.10: Optimized structures for O and OH bindings on PC_2N_2 motifs; a) PC_2N_2 (planar), b) $\text{PO-C}_2\text{N}_2$ (out-of-plane), c) $\text{P(OH)}_2\text{-C}_2\text{N}_2$ (planar), d) $\text{POH-C}_2\text{N}_2$ (out-of-plane).

Table 3.2.6: Subsequent binding energy of OH on P-bound motifs obtained with reference to free OH in the doublet state.

Binding Motif	EB (1 st OH) [eV]	EB (2 nd OH) [eV]
PN_4	-3.39	-4.40
PCN_3	-3.78	-3.86
PC_2N_2	-3.92	-2.91
PC_3N	-2.90	-3.19
PC_4	-3.31	-2.46

The doped atoms can be observed with atomic resolution scanning transmission electron microscopy (AR-STEM) when the doped atom has higher molecular weight than carbon scaffold. This technique was used in order to see the distribution and location of phosphorus atoms and the images were acquired in National Institute of Chemistry in Ljubljana. Due to the higher molecular weight of phosphorus (31) compared to carbon (12) and nitrogen (14), high

contrast was obtained. The white spots (Figure 3.2.11) show that phosphorus atoms are atomically dispersed in the amorphous carbon scaffold and polyphosphate-like structures were not observed. Despite the clear figure of single phosphorus atoms, it is not possible to detect in-plane coordination as nitrogen and carbon have similar molecular weight. However, it is noteworthy that square planar configuration is favorable according to DFT calculations.

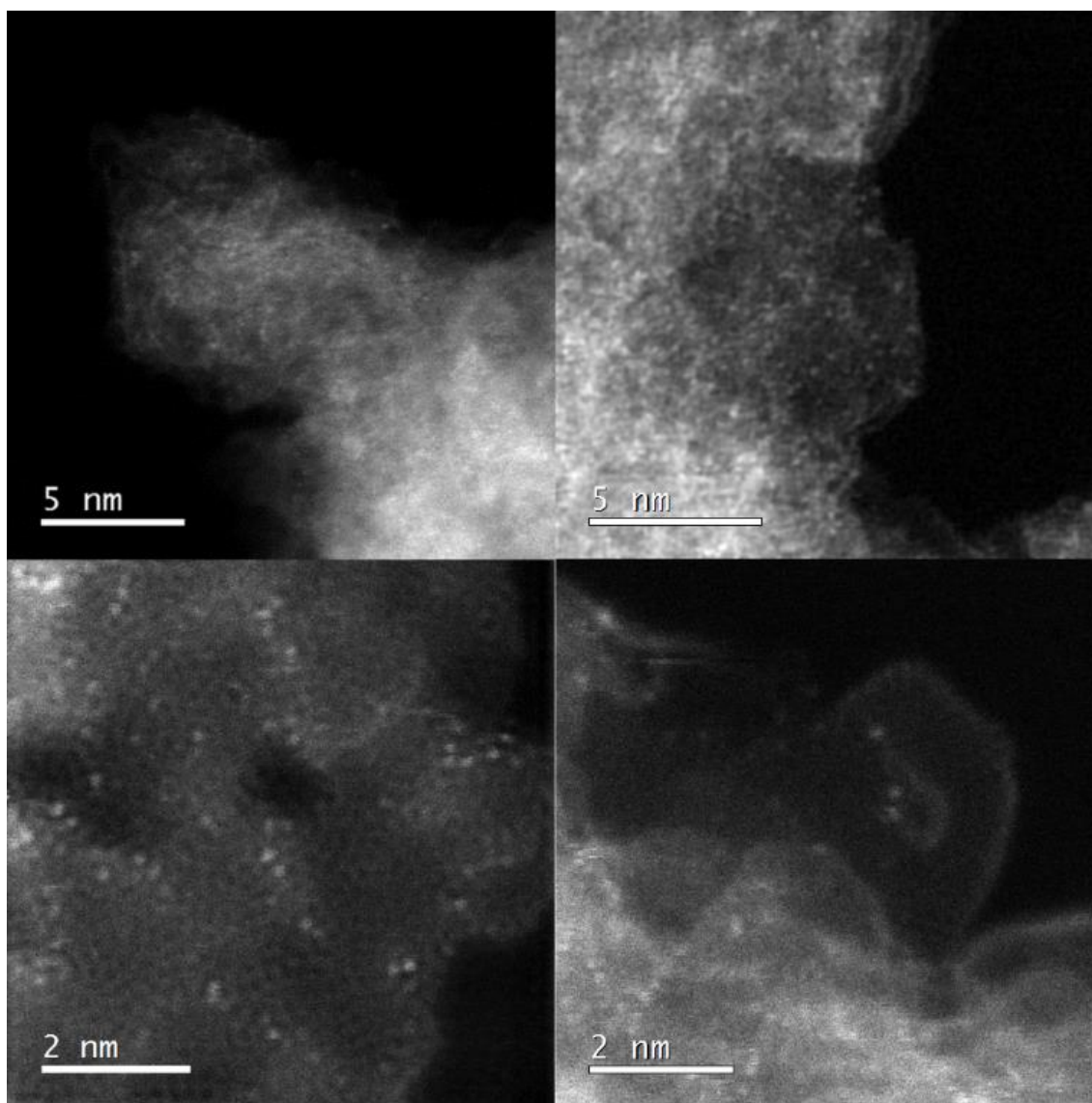


Figure 3.2.11: AR-STEM images of PANI_H₃PO₄_1000 relevant for all carbons we have measured.

The electrocatalytic activity towards ORR was tested using three electrode set-up with 0.1 M NaOH. CVs and LSVs were acquired for $200 \mu\text{g cm}^{-2}$ and $438 \mu\text{g cm}^{-2}$ loadings. In PANI_H₃PO₄, temperature effect is more pronounced at low loading (Figure 3.2.12) whereas there is less pronounced difference at high loading. The limited improvement in the activity at high loading for PANI_H₃PO₄_1000 is clearly observed in $E_{1/2}$ (~ 10 mV difference for $200 \mu\text{g cm}^{-2}$ and $438 \mu\text{g cm}^{-2}$ loadings). However, the precursor type plays a significant role on the final activity regardless of the temperature and loading. IL_H₃PO₄ samples outperform PANI_H₃PO₄ samples at each temperature and loading.

Cyclic voltammetry (CV) plots under Ar exhibit consistent feature with literature (Figure S3.3.6).⁹² Similar capacitive currents are observed for both type of samples despite the remarkable difference in SSAs (Table 3.2.2). Linear scanning voltammetry (LSV) plots disclose the activity differences towards ORR in alkaline. Accordingly, PANI_H₃PO₄ samples outperform IL_H₃PO₄ samples at low loading ($200 \mu\text{g cm}^{-2}$) particularly in kinetic region. However, increasing loading improves the activity in IL_H₃PO₄ higher degree whereas no big difference was observed for PANI_H₃PO₄. Furthermore, PANI-derived samples hardly reach to limiting current at low loading. The half wave potential $E_{1/2}$ of ~ 0.7 V vs. RHE is obtained, which is in agreement with N,P doped carbon ORR electrocatalysts in the literature, that have no active metal involved in the synthesis.¹¹¹⁻¹¹⁴ The limiting current indicates the number of electron transferred in the electrochemical reaction which can be determined by using Levich equation (Equation 4). The limiting currents for PANI_H₃PO₄ samples are close to theoretical limiting current for two electron process in which O₂ is reduced to H₂O₂. Nevertheless, the high loadings of PANI_H₃PO₄_1000 result in the onset potential of > 0.85 V (Figure 3.2.13).

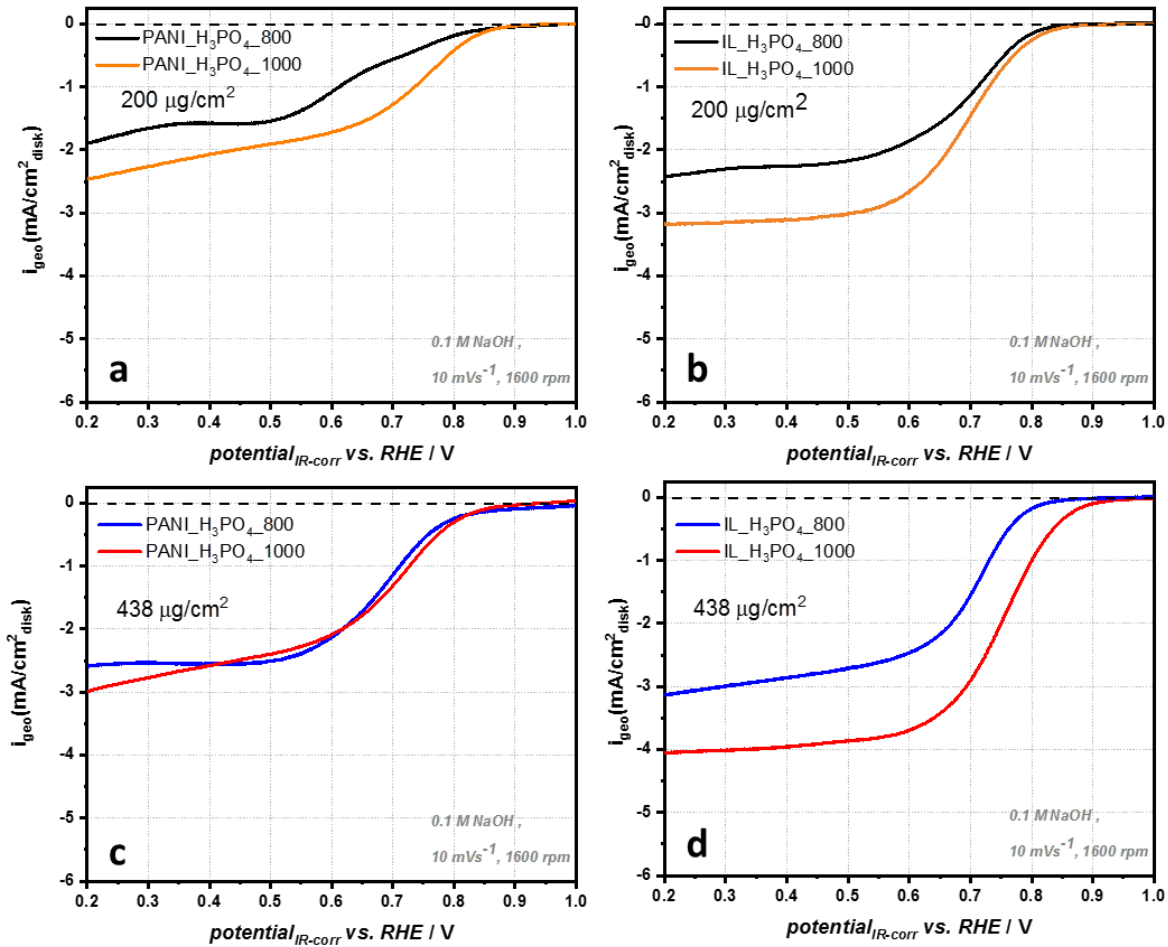


Figure 3.2.12: Temperature and loading dependency of ORR activities of: a) PANI_H₃PO₄ 200 μgcm⁻², b) IL_H₃PO₄ 200 μgcm⁻², c) PANI_H₃PO₄ 438 μgcm⁻², d) IL_H₃PO₄ 438 μgcm⁻².

$$j_L = 0.62nFC_0D_0^{2/3}v^{-\frac{1}{6}}\omega^{\frac{1}{2}} \quad \text{Equation 4}$$

IL_H₃PO₄ samples reach to the limiting current even at low loading (Figure 3.2.13). This feature might indicate the higher number of active sites in IL-derived samples. At high loading, limiting current reaches to 4 mA cm⁻² corresponding to 2.8 electron transferred in electrochemical reaction. Also, higher loading leads to halfwave potential 0.75 V and onset

potential > 0.9 V. This activity is among the best activities reported for P-N doped metal free catalysts.¹¹⁵⁻¹¹⁶

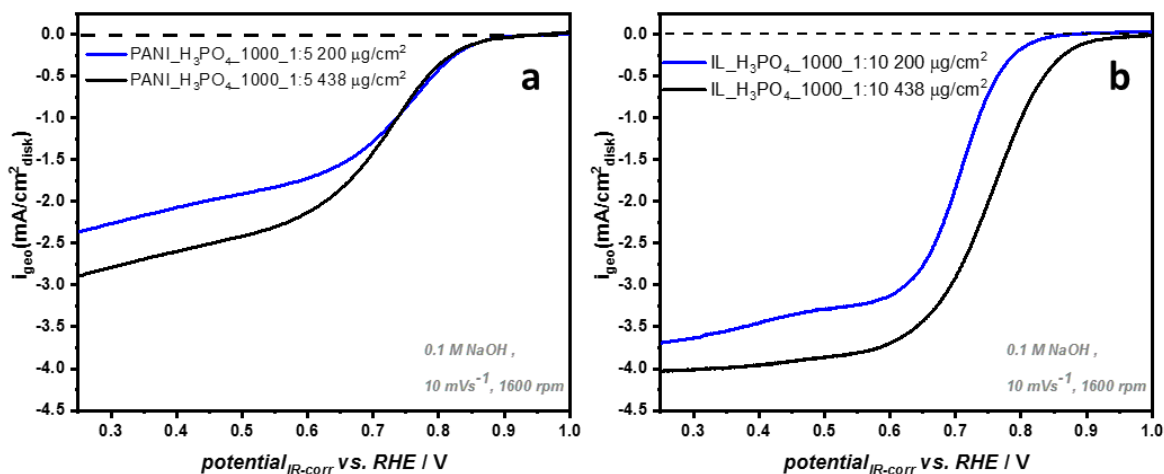


Figure 3.2.13: LSVs (1600 rpm) at two different loadings a) PANI_H₃PO₄_1000 and b) IL_H₃PO₄_1000.

In conclusion, high temperature synthesis was achieved using H₃PO₄ as porogen and phosphorus source. The carbonization of carbon and nitrogen precursors (PANI and IL) in the presence of water-free H₃PO₄ resulted in highly porous carbons with hierarchical structure. The combination of our previous results with high temperature synthesis approach gives opportunity to synthesize phosphorus and nitrogen doped conductive carbons as well as freedom to design a desired pore system. The characterization of the resulting samples revealed the presence of P and N atoms doped in graphitic rings of carbon matrix with different moieties. Among these moieties, we uncovered existence of P-N bond especially at high temperature using spectroscopic methods. The ORR activities of the synthesized samples are found to be among the highest activities for metal-free catalysts in alkaline medium. Our method for

synthesis of P/N-doped samples shows big potential for industrial scale synthesis of highly active ORR catalysts.

4. Conclusion

The synthesis of PGM-free catalysts was investigated for oxygen reduction reaction in fuel cells in acidic and alkaline media. It was aimed to meet two important criteria for commercial use of PGM-free ORR catalysts: high activity and scalability.

First, a novel synthesis method was implemented to a platform material that has hierarchical pore structure and MgN_4 moieties. The investigation of the pore structure of the materials showed extremely large surface area ($>1100 \text{ m}^2$) and the presence meso- and macropores which plays an important role in O_2 transport. The exchange of Mg with Fe increased the activity by more than 300 mV and reached to the mass activity values similar to commercial catalyst even with only single heat-treatment. Furthermore, the structural characterization revealed that despite the low Fe content in the catalysts, the relative content of active FeN_4 sites (D1) are considerably high (42.9 %) which makes these catalysts highly efficient towards ORR. Also, the stability tests showed relatively stable structure for carbon corrosion up to 100 cycles and slight degradation after 1000 cycles. Moreover, the high yields obtained from the synthesis of platform materials make this approach promising for commercial use of PGM-free catalysts in acidic medium.

The utilization of PGM-free catalysts in alkaline was also studied from industrial point of view. First, a mechanistic study was conducted on activation process with Brønsted acids and various carbon precursors. The porosity development monitored via N_2 sorption and imaging techniques pointed out that the excess amount of acid leads to formation of bigger pores and wider separation of the particles. The consistent results obtained from molecular, polymeric and biomass-based carbon precursors indicate that the chemical activation process is similar to

sol-gel process when excess amount of solvent is used. A high control on porosity development was gained as a result of mechanistic study. The findings in mechanistic study were used to synthesize highly porous conductive carbons at high temperature. The carbonization of two different precursors (PANI and IL) with H_3PO_4 led to formation of carbons with hierarchical porosity. The characterization of the structure disclosed the presence of P atoms atomically dispersed in the carbon sheets and P-N bonds on the surface. The ORR activities of these metal-free catalysts were found to be among the highest activities reported in the literature for alkaline medium.

The synthesis methods studied in this thesis possess big potential for industrial synthesis and commercial use of highly active ORR catalysts in acidic and alkaline medium. The characterization techniques and tests showed that the approaches suggested in this thesis can be used to replace the conventional catalysts.

5. Outlook

As the activity of the catalyst highly depends on the density of active sites (Chapter 2.1), synthesis of the carbons with denser Me-N₄ sites play crucial role. Porous organic polymers (POPs) and MOFs are capable of hosting denser imprinted sites owing to their tunable structures. The carbonization of POPs or MOFs will yield to higher amount of Me-N₄ sites per unit (volume/mass) of carbon. Also, salt-melt method would be effective during the porosity development to preserve/create meso- or macropores and form more Me-N₄ sites.

Additionally, a post heat treatment can be applied to P-N doped carbons. It was consistently shown that a post heat treatment boosts the activity.^{39, 63, 117} However, a number of factor such as the type of gas (Ar, NH₃), the composition of gas (%), flow of gas, heating ramp, dwelling time, cooling time etc. makes the origin of this improvement difficult to understand. Therefore, a systematic investigation including in-situ and ex-situ characterizations is required for post heat treatment. However, since high temperature increases the graphitization degree and remove functional groups, it would be useful especially for P/N-doped carbons that have oxygen content (8.69-12.44 at%).

As Chapter 3 provides a new approach for the synthesis of electrocatalysts, a wide range of precursors including various biomass types and waste materials can be employed in the synthesis of PGM-free catalysts. A number of precursors can be used to synthesize conductive porous carbon with our high temperature H₃PO₄ approach with a desired porosity. The nitrogen incorporation can be achieved by either employing the nitrogen containing precursors or post-mortem ammonolysis process.¹¹⁸⁻¹¹⁹

Taking the advantage of the active site imprinting method, the effect of the side phases on the activity can be studied. The systematical investigation of the contribution of iron carbide or metallic iron to ORR can be accomplished by adding these species sequentially to the active site imprinted catalysts.

The quantification of the active sites is a challenging process in PGM-free catalysts compared to Pt-based catalysts. The precise quantification can lead to deeper understanding of kinetics as well as degradation mechanisms. Recent publications showed that electrochemical determination is possible by probe molecules. However, further investigation and establishment of a general quantification method will be crucial in the future. In this context, more uniform samples such as active site imprinted catalysts will be useful.

6. Experimental Methods

6.1 Synthesis of the Materials

The samples used for mechanistic investigation were synthesized using different carbon precursors and solvents. Table 2.1 shows the carbon precursors and solvents. Prior to mixing of solvent and precursors, cryogenic grinding was carried out for coconut shells in order to decrease the particle size. Afterwards, ground shells were transferred to jar and ball milled with liquid nitrogen in FRITSCH Planetary Micro Mill Pulverisette 7 with 200 rpm for 2 min. The entire process was repeated several times until fine powders were obtained.

As porogen, the solvents given in Table 6.1.1 were used with different weight ratio. As an example, roughly 0.5 g of coconut shells was mixed with 0.5 g of H_3PO_4 and transferred with Schlenk tube to a Gerhardt ACIDORAPID oven and treated at 560 °C for 3 hours under argon flow. The same procedure was applied to all solvent-precursor pairs except H_3PO_4 and ionic liquid (1-Ethyl-3-methylimidazolium dicyanamide). Ionic liquid (IL) and H_3PO_4 mixture was prepared in Ar-filled glovebox due to hygroscopic properties. The samples were washed with 1 L of milliQ-water and 0.1 M HCl and dried at 70 °C overnight.

Table 6.1.1: List of precursors and solvents used in mechanistic study.

Solvent	Precursors
H_3PO_4 , H_3BO_3 , Borax/ H_3BO_3	Glucose Ionic Liquid (EMIM DCA) PANI Coconut shells

The samples used in the high temperature section were synthesized in a similar fashion as in mechanistic study. Polyaniline (Emeraldine base) and ortho-phosphoric acid (99%, cryst.

for analysis) were purchased from Sigma Aldrich and stored in Ar-filled glovebox. Ionic liquid (1-Ethyl-3-methylimidazolium dicyanamide) was purchased from Solvionic. NaOH.H₂O (99.996%) was purchased from Alfa Aesar.

In the synthesis, 1:5 and 1:10 precursor-to-solvent ratios were used for PANI_H₃PO₄ and IL_H₃PO₄ samples, respectively. The mixture of precursor and solvent was ground using mortar and pestle in Ar-filled glovebox. The mixture was transferred to a tube furnace (HTM Reetz GmbH) in a silicon carbide crucible and heated up to 800, 900 and 1000 °C the heating ramp of 10 K/min and kept at final temperature for 3 hours under Ar atmosphere. Resulting samples were washed with water and 0.1 M HCl overnight followed by filtration.

Magnesium iminodiacetic acid metal organic coordination polymer (Mg-IDA MOCP) was prepared according to the literature work.¹²⁰ In a typical synthesis, 15.97 g of iminodiacetic acid (0.12 mol) were added to 300 mL DI preheated to 85 °C in a 2L beaker and stirred until the IDA dissolved entirely. Then 11.66 g of basic magnesium carbonate (0.096 mol) were added and a white material precipitated. The solution was allowed to stir for 15 minutes, and subsequently transferred to an ice bath and 1.5 L of ethanol were added. The precipitate was allowed to settle overnight, then the liquid decanted and the beaker put into an oven at 50 °C to dry for 3 days.

Mg-IDA was put into a quartz boat and loaded into a tube furnace. The material was heated to 70 °C for 1 hour under a flow of argon, and then to temperature T (800, 850, 900, 950 °C) for 1 hour, then allowed to cool down to room temperature. The carbon was put into 150 mL of 1 M HCl overnight (to remove the MgO which formed during the synthesis), then filtered, washed with copious amounts of DI and dried overnight at a 50 °C oven.

Fe transmetallation was carried out in 50 mM FeCl₂ solution with reflux in methanol at 80 °C followed by an acidic work-up with 0.1 M HCl overnight and deionized water. Transmetallated samples were dried in the oven at 80 °C.

6.2 Characterization Techniques

Porosity measurements for all the samples were conducted with Quantachrome Autosorb iQ. The samples were outgassed approximately 12 hours at 150 °C prior to the measurements. For N₂ sorption measurements, isotherms were acquired between p/p₀ of 10⁻⁵ and 1 p/p₀. BET surface areas were calculated according to BET theory¹²¹ using the BET micropore assistant module in ASiQwin software provided by Quantachrome. The pore size distribution, micropore volume and micropore surface area were determined by slit/cylindrical/sphere pore model of Quenched Solid Density Functional Theory (QSDFT) method. Total pore volume was calculated from the uptake at p/p₀ ~ 1. CO₂ (99.999%) sorption was performed with the same instrument at 273 K between 10⁻⁴ and 0.03 p p₀⁻¹. Pore size distributions were calculated using ASiQwin software using the NLDFT model for carbons.

Kratos Axis Supra spectrometer with monochromated Al K_α radiation was used for the surface investigation of the samples synthesized for mechanistic study and high temperature P-N doped carbons. Spectra were collected with step size of 0.1 eV in the corresponding binding energy range and charge correction was carried out taking the C1s peak (284.7 eV) as reference. The deconvolutions were done with ESCAA software. (Mg/NCs) and [Fe(NCs)] samples were prepared by depositing a sample on copper tape, and the spectra was collected on a PHI VersaProbe III scanning microprobe supplied from Physical Instruments at UHV ~ 10⁻¹⁰ torr

with step size of 0.05 eV. The charge correction was applied using the C 1s position (284.7 eV) and deconvolution was performed in CasaXPS software.

Mössbauer spectra were recorded with a sinusoidal velocity waveform at room temperature and at 4.2 K on powder samples enclosed in lucite holders. For the low-temperature measurements, both the absorber and the ^{57}Co in rhodium source were cooled in a liquid helium bath cryostat. The fitting of the spectrum was carried out with MOS90 software (version 2.2). Isomer shifts were measured with respect to the source having the same temperature as the absorber. In order to refer the shifts to $\alpha\text{-Fe}$ at room temperature, 0.115 mm s^{-1} was added to the shifts measured at room temperature and 0.245 mm s^{-1} to those measured at 4.2 K.

Mass spectrometry-coupled thermogravimetric analysis (TG-MS) for the samples in Chapter 2 and Chapter 3 was carried out TGA/DSC 1 and the THERMO Star Gas analysis system (Pfeiffer Vacuum) instruments, equipped with a gas controller (GC 200, Mettler Toledo Corp., Switzerland). The samples were heated up to $100 \text{ }^\circ\text{C}$ (Chapter 2) and $150 \text{ }^\circ\text{C}$ (Chapter 3) and kept for 1 h for drying step followed by heating up to $950 \text{ }^\circ\text{C}$ (Chapter 2) and $1000 \text{ }^\circ\text{C}$ (Chapter 3).

Transmission Electron Microscopy (TEM) images for samples synthesized in Chapter 3 were acquired using a conventional TECNAI G²20 S-TWIN (FEI company, Oregon, USA) with LaB₆-emitter. The microscope equipped with an EDX r-TEM SUTW detector (EDAX Inc., New Jersey, USA), 1024x1024 pixel MS794 P CCD Camera (GATAN Inc., California, USA) was operated at 200 kV. The powders were dispersed in ethanol and sonicated for 10 minutes. Then 3 μl of the suspension was dropcasted on a Cu 300 mesh holey-carbon TEM grid. The grids were dried on air at ca. 50°C for another 10 minutes.

Electrochemical characterizations and activity measurements were conducted employing three electrode set-up (RDE) and an automated test station (G60, Greenlight Innovation, Canada). In RDE, Platinum wire was used as reference electrode (RE) and gold wire was used as counter electrode (CE) in 0.1 M HClO₄ (Chapter 2) and 0.1 M NaOH (Chapter 3) electrolyte. The catalyst ink was prepared dispersing the catalyst powder in dimethylformamide (DMF) and adding ionomer (Nafion © 5 wt% in mixture of aliphatic alcohols and water) followed by 20 min sonication. In a typical ink preparation, 2 mg sample and 47.2 µl ionomer were dispersed in 652 µl DMF and after 20 min sonication, 13.7 µl ink was dropcasted on glassy carbon (working electrode) aiming at 200 µg/cm² catalyst loading. A gold disk electrode was used as working electrode (WE) for the stability measurements (Chapter 2).

The fuel cell tests were performed in a 5 cm² single cell in differential conditions with counter flow configuration. The inks were prepared by dispersing the catalyst in 1-propanol and the addition of ionomer followed by mixing process. In a typical preparation, 0.2 g catalyst was used and dispersed in 1-propanol (2.27 mL) in 12 mL container with 5.5 g ZrO₂ beads (diameter: 2 mm). 0.53 g ionomer (700 EW, Asahi Kasei, Japan) was added and mixed in Thinky planetary mixer for 10 min with 500 rpm. After mixing, the ink was coated on PTFE foil (50 µm thick) and dried at room temperature. The MEAs were prepared by hot pressing the anode (0.1 mg_{Pt}/cm²), the membrane (Gore and Nafion 212 for [Fe(N/C_900_950)] and Pajarito Powder, respectively) and the cathode at 165 °C for 15 min. The cell was assembled using gas diffusion layer (H14C10) with the compression of 20%. The tests were performed with H₂ in anode (2000 ncm) and O₂ (100 kPa partial pressure) in cathode (5000 ncm) at 80 °C and in 100% relative humidity. The polarization curves were recorded by holding 5 min in each point followed by impedance measurement for determination of high frequency resistance. The

proton sheet resistance was measured in H₂ (anode) and N₂ (cathode) configuration at 80 °C and in 100 relative humidity.

7. Bibliography

1. Winter, C.-J., Hydrogen energy—Abundant, efficient, clean: A debate over the energy-system-of-change. *International journal of hydrogen energy* **2009**, *34* (14), S1-S52.
2. Ritchie, H.; Roser, M., CO₂ and Greenhouse Gas Emissions. *Our world in data* **2017**.
3. Pollet, B. G.; Kocha, S. S.; Staffell, I., Current status of automotive fuel cells for sustainable transport. *Current Opinion in Electrochemistry* **2019**.
4. <https://carsalesbase.com/us-toyota-mirai/>.
5. Fuel cell zero-emission buses for the city of London. https://www.ballard.com/docs/default-source/motive-modules-documents/transport-for-london-case-study-website.pdf?sfvrsn=9f51c280_2.
6. Thompson, S. T.; James, B. D.; Huya-Kouadio, J. M.; Houchins, C.; DeSantis, D. A.; Ahluwalia, R.; Wilson, A. R.; Kleen, G.; Papageorgopoulos, D., Direct hydrogen fuel cell electric vehicle cost analysis: System and high-volume manufacturing description, validation, and outlook. *Journal of Power Sources* **2018**, *399*, 304-313.
7. Krewitt, W.; Heck, T.; Trukenmüller, A.; Friedrich, R., Environmental damage costs from fossil electricity generation in Germany and Europe. *Energy Policy* **1999**, *27* (3), 173-183.
8. Schmid, E.; Pahle, M.; Knopf, B., Renewable electricity generation in Germany: a meta-analysis of mitigation scenarios. *Energy Policy* **2013**, *61*, 1151-1163.
9. Cifrain, M.; Kordesch, K., Hydrogen/oxygen (air) fuel cells with alkaline electrolytes. *Handbook of fuel cells* **2010**.
10. Mehmood, A.; Pampel, J.; Ali, G.; Ha, H. Y.; Ruiz-Zepeda, F.; Fellingner, T. P., Facile Metal Coordination of Active Site Imprinted Nitrogen Doped Carbons for the Conservative Preparation of Non-Noble Metal Oxygen Reduction Electrocatalysts. *Advanced Energy Materials* **2018**, *8* (9), 1701771.
11. Harzer, G. S. Boosting High Current Density Performance of Durable, Low Pt-Loaded PEM Fuel Cells. Technische Universität München, 2018.
12. Neyerlin, K.; Gu, W.; Jorne, J.; Clark, A.; Gasteiger, H. A., Cathode catalyst utilization for the ORR in a PEMFC analytical model and experimental validation. *Journal of The Electrochemical Society* **2007**, *154* (2), B279-B287.

13. Appleby, A., Electrocatalysis and fuel cells. *Catalysis Reviews* **1971**, 4 (1), 221-244.
14. James, B., Fuel Cell Systems Analysis. *US Department of Energy, Washington, DC* **2017**.
15. Imashiro, Y.; Kishimoto, T.; Tetsutaro, S.; Ozaki, J.-i.; Takuya, M.; Kusadokoro, S., Carbon catalyst, electrode, and battery. Google Patents: 2019.
16. Banham, D.; Choi, J. Y.; Kishimoto, T.; Ye, S., Integrating PGM-Free Catalysts into Catalyst Layers and Proton Exchange Membrane Fuel Cell Devices. *Advanced Materials* **2019**, 31 (31), 1804846.
17. Kendall, M., Fuel cell development for New Energy Vehicles (NEVs) and clean air in China. *Progress in Natural Science: Materials International* **2018**, 28 (2), 113-120.
18. Du, L.; Xing, L.; Zhang, G.; Dubois, M.; Sun, S., Strategies for Engineering High-Performance PGM-Free Catalysts toward Oxygen Reduction and Evolution Reactions. *Small Methods* **2020**, 2000016.
19. Thompson, S. T.; Wilson, A. R.; Zelenay, P.; Myers, D. J.; More, K. L.; Neyerlin, K.; Papageorgopoulos, D., ElectroCat: DOE's approach to PGM-free catalyst and electrode R&D. *Solid State Ionics* **2018**, 319, 68-76.
20. Menga, D.; Ruiz-Zepeda, F.; Moriau, L.; Šála, M.; Wagner, F.; Koyutürk, B.; Bele, M.; Petek, U.; Hodnik, N.; Gaberšček, M., Active-Site Imprinting: Preparation of Fe–N–C Catalysts from Zinc Ion–Templated Ionothermal Nitrogen-Doped Carbons. *Advanced Energy Materials* **2019**, 9 (43), 1902412.
21. Ukanwa, K. S.; Patchigolla, K.; Sakrabani, R.; Anthony, E.; Mandavgane, S., A Review of Chemicals to Produce Activated Carbon from Agricultural Waste Biomass. *Sustainability* **2019**, 11 (22), 6204.
22. Gupta, T., Historical Production and Use of Carbon Materials: The Activated Carbon. In *Carbon*, Springer: 2018; pp 47-70.
23. Kyaw, H. H.; Myint, M. T. Z.; Al-Harhi, S.; Al-Abri, M., Removal of heavy metal ions by capacitive deionization: Effect of surface modification on ions adsorption. *Journal of hazardous materials* **2020**, 385, 121565.
24. Shafeeyan, M. S.; Daud, W. M. A. W.; Houshmand, A.; Shamiri, A., A review on surface modification of activated carbon for carbon dioxide adsorption. *Journal of Analytical and Applied Pyrolysis* **2010**, 89 (2), 143-151.

25. Yan, X.; Jia, Y.; Odedairo, T.; Zhao, X.; Jin, Z.; Zhu, Z.; Yao, X., Activated carbon becomes active for oxygen reduction and hydrogen evolution reactions. *Chemical Communications* **2016**, 52 (52), 8156-8159.
26. Heidarinejad, Z.; Dehghani, M. H.; Heidari, M.; Javedan, G.; Ali, I.; Sillanpää, M., Methods for preparation and activation of activated carbon: a review. *Environmental Chemistry Letters* **2020**, 1-23.
27. Diao, Y.; Walawender, W.; Fan, L., Activated carbons prepared from phosphoric acid activation of grain sorghum. *Bioresource technology* **2002**, 81 (1), 45-52.
28. Liu, Q.-S.; Zheng, T.; Wang, P.; Guo, L., Preparation and characterization of activated carbon from bamboo by microwave-induced phosphoric acid activation. *Industrial Crops and Products* **2010**, 31 (2), 233-238.
29. de Yuso, A. M.; Rubio, B.; Izquierdo, M. T., Influence of activation atmosphere used in the chemical activation of almond shell on the characteristics and adsorption performance of activated carbons. *Fuel processing technology* **2014**, 119, 74-80.
30. Molina-Sabio, M.; Rodríguez-Reinoso, F., Role of chemical activation in the development of carbon porosity. *Colloids and Surfaces A: Physicochemical and Engineering Aspects* **2004**, 241 (1-3), 15-25.
31. Porada, S.; Schipper, F.; Aslan, M.; Antonietti, M.; Presser, V.; Fellingner, T.-P., Capacitive deionization using biomass-based microporous salt-templated heteroatom-doped carbons. **2015**.
32. World production of platinum group metals, 2009–2018 <https://www.nrcan.gc.ca/our-natural-resources/minerals-mining/minerals-metals-facts/platinum-facts/20520#L2>.
33. Price Charts. <http://www.platinum.matthey.com/prices/price-charts#>.
34. Jacoby, M., Fuel-cell cars finally drive off the lot. *Chem. Eng. News Arch* **2017**, 95, 28.
35. DOE Technical Targets for Polymer Electrolyte Membrane Fuel Cell Components. <https://www.energy.gov/eere/fuelcells/doe-technical-targets-polymer-electrolyte-membrane-fuel-cell-components>.
36. Jasinski, R., A new fuel cell cathode catalyst. *Nature* **1964**, 201 (4925), 1212-1213.
37. Jahnke, H.; Schönborn, M.; Zimmermann, G., Organic dyestuffs as catalysts for fuel cells. In *Physical and chemical applications of dyestuffs*, Springer: 1976; pp 133-181.

38. Gupta, S.; Tryk, D.; Bae, I.; Aldred, W.; Yeager, E., Heat-treated polyacrylonitrile-based catalysts for oxygen electroreduction. *Journal of applied electrochemistry* **1989**, *19* (1), 19-27.
39. Lefèvre, M.; Proietti, E.; Jaouen, F.; Dodelet, J.-P., Iron-based catalysts with improved oxygen reduction activity in polymer electrolyte fuel cells. *science* **2009**, *324* (5923), 71-74.
40. Mathias, M. F.; Makharia, R.; Gasteiger, H. A.; Conley, J. J.; Fuller, T. J.; Gittleman, C. J.; Kocha, S. S.; Miller, D. P.; Mittelsteadt, C. K.; Xie, T., Two fuel cell cars in every garage? *Interface-Electrochemical Society* **2005**, *14* (3), 24-36.
41. Gasteiger, H. A.; Kocha, S. S.; Sompalli, B.; Wagner, F. T., Activity benchmarks and requirements for Pt, Pt-alloy, and non-Pt oxygen reduction catalysts for PEMFCs. *Applied Catalysis B: Environmental* **2005**, *56* (1-2), 9-35.
42. Gasteiger, H. A.; Marković, N. M., Just a dream—or future reality? *science* **2009**, *324* (5923), 48-49.
43. Wu, G.; More, K. L.; Johnston, C. M.; Zelenay, P., High-performance electrocatalysts for oxygen reduction derived from polyaniline, iron, and cobalt. *Science* **2011**, *332* (6028), 443-447.
44. Li, J.; Chen, M.; Cullen, D. A.; Hwang, S.; Wang, M.; Li, B.; Liu, K.; Karakalos, S.; Lucero, M.; Zhang, H., Atomically dispersed manganese catalysts for oxygen reduction in proton-exchange membrane fuel cells. *Nature Catalysis* **2018**, *1* (12), 935-945.
45. Wan, X.; Liu, X.; Li, Y.; Yu, R.; Zheng, L.; Yan, W.; Wang, H.; Xu, M.; Shui, J., Fe–N–C electrocatalyst with dense active sites and efficient mass transport for high-performance proton exchange membrane fuel cells. *Nature Catalysis* **2019**, *2* (3), 259-268.
46. Banham, D.; Ye, S., Current status and future development of catalyst materials and catalyst layers for proton exchange membrane fuel cells: an industrial perspective. *ACS Energy Letters* **2017**, *2* (3), 629-638.
47. Scopus <https://www.scopus.com/search/form.uri?display=basic>.
48. Artyushkova, K.; Rojas-Carbonell, S.; Santoro, C.; Weiler, E.; Serov, A.; Awais, R.; Gokhale, R. R.; Atanassov, P., Correlations between Synthesis and Performance of Fe-Based PGM-Free Catalysts in Acidic and Alkaline Media: Evolution of Surface Chemistry and Morphology. *ACS Applied Energy Materials* **2019**, *2* (8), 5406-5418.

49. Pampel, J.; Fellingner, T. P., Opening of bottleneck pores for the improvement of nitrogen doped carbon electrocatalysts. *Advanced Energy Materials* **2016**, *6* (8), 1502389.
50. Serov, A.; Artyushkova, K.; Andersen, N. I.; Stariha, S.; Atanassov, P., Original mechanochemical synthesis of non-platinum group metals oxygen reduction reaction catalysts assisted by sacrificial support method. *Electrochimica Acta* **2015**, *179*, 154-160.
51. Chung, H. T.; Won, J. H.; Zelenay, P., Active and stable carbon nanotube/nanoparticle composite electrocatalyst for oxygen reduction. *Nature communications* **2013**, *4* (1), 1-5.
52. Barkholtz, H. M.; Liu, D.-J., Advancements in rationally designed PGM-free fuel cell catalysts derived from metal-organic frameworks. *Materials Horizons* **2017**, *4* (1), 20-37.
53. Ma, S.; Goenaga, G. A.; Call, A. V.; Liu, D. J., Cobalt imidazolate framework as precursor for oxygen reduction reaction electrocatalysts. *Chemistry—A European Journal* **2011**, *17* (7), 2063-2067.
54. He, Y.; Tan, Q.; Lu, L.; Sokolowski, J.; Wu, G., Metal-nitrogen-carbon catalysts for oxygen reduction in PEM fuel cells: self-template synthesis approach to enhancing catalytic activity and stability. *Electrochemical Energy Reviews* **2019**, 1-21.
55. Calle-Vallejo, F.; Martínez, J. I.; Rossmeisl, J., Density functional studies of functionalized graphitic materials with late transition metals for oxygen reduction reactions. *Physical Chemistry Chemical Physics* **2011**, *13* (34), 15639-15643.
56. Thommes, M.; Kaneko, K.; Neimark, A. V.; Olivier, J. P.; Rodriguez-Reinoso, F.; Rouquerol, J.; Sing, K. S., Physisorption of gases, with special reference to the evaluation of surface area and pore size distribution (IUPAC Technical Report). *Pure and Applied Chemistry* **2015**, *87* (9-10), 1051-1069.
57. Thommes, M., Physical adsorption characterization of nanoporous materials. *Chemie Ingenieur Technik* **2010**, *82* (7), 1059-1073.
58. Artyushkova, K.; Levendosky, S.; Atanassov, P.; Fulghum, J., XPS structural studies of nano-composite non-platinum electrocatalysts for polymer electrolyte fuel cells. *Topics in Catalysis* **2007**, *46* (3-4), 263-275.
59. Artyushkova, K., Misconceptions in interpretation of nitrogen chemistry from x-ray photoelectron spectra. *Journal of Vacuum Science & Technology A: Vacuum, Surfaces, and Films* **2020**, *38* (3), 031002.

60. Wagner, S.; Auerbach, H.; Tait, C. E.; Martinaiou, I.; Kumar, S. C.; Kübel, C.; Sergeev, I.; Wille, H. C.; Behrends, J.; Wolny, J. A., Elucidating the Structural Composition of an Fe–N–C Catalyst by Nuclear-and Electron-Resonance Techniques. *Angewandte Chemie International Edition* **2019**, *58* (31), 10486-10492.
61. Greenwood, N. N., *Mössbauer spectroscopy*. Springer Science & Business Media: 2012.
62. Mineva, T.; Matanovic, I.; Atanassov, P.; Sougrati, M.-T.; Stievano, L.; Clémancey, M.; Kochem, A.; Latour, J.-M.; Jaouen, F., Understanding Active Sites in Pyrolyzed Fe–N–C Catalysts for Fuel Cell Cathodes by Bridging Density Functional Theory Calculations and ⁵⁷Fe Mössbauer Spectroscopy. *ACS Catalysis* **2019**, *9* (10), 9359-9371.
63. Kramm, U. I.; Herrmann-Geppert, I.; Bogdanoff, P.; Fiechter, S., Effect of an ammonia treatment on structure, composition, and oxygen reduction reaction activity of Fe–N–C catalysts. *The Journal of Physical Chemistry C* **2011**, *115* (47), 23417-23427.
64. Koslowski, U. I.; Abs-Wurmbach, I.; Fiechter, S.; Bogdanoff, P., Nature of the catalytic centers of porphyrin-based electrocatalysts for the ORR: a correlation of kinetic current density with the site density of Fe–N₄ centers. *The Journal of Physical Chemistry C* **2008**, *112* (39), 15356-15366.
65. Shao, Y.; Dodelet, J. P.; Wu, G.; Zelenay, P., PGM-Free Cathode Catalysts for PEM Fuel Cells: A Mini-Review on Stability Challenges. *Advanced Materials* **2019**, *31* (31), 1807615.
66. Banham, D.; Ye, S.; Pei, K.; Ozaki, J.-i.; Kishimoto, T.; Imashiro, Y., A review of the stability and durability of non-precious metal catalysts for the oxygen reduction reaction in proton exchange membrane fuel cells. *Journal of Power Sources* **2015**, *285*, 334-348.
67. Roen, L.; Paik, C.; Jarvi, T., Electrocatalytic corrosion of carbon support in PEMFC cathodes. *Electrochemical and Solid-State Letters* **2004**, *7* (1), A19-A22.
68. Mittermeier, T.; Weiß, A.; Hasché, F.; Hübner, G.; Gasteiger, H. A., PEM fuel cell start-up/shut-down losses vs temperature for non-graphitized and graphitized cathode carbon supports. *Journal of The Electrochemical Society* **2017**, *164* (2), F127-F137.
69. Forouzandeh, F.; Li, X.; Banham, D. W.; Feng, F.; Ye, S.; Birss, V., Understanding the corrosion resistance of meso-and micro-porous carbons for application in PEM fuel cells. *Journal of The Electrochemical Society* **2018**, *165* (6), F3230.

-
70. Paraknowitsch, J. P.; Thomas, A., Doping carbons beyond nitrogen: an overview of advanced heteroatom doped carbons with boron, sulphur and phosphorus for energy applications. *Energy & Environmental Science* **2013**, *6* (10), 2839-2855.
71. Choi, C. H.; Park, S. H.; Woo, S. I., Binary and ternary doping of nitrogen, boron, and phosphorus into carbon for enhancing electrochemical oxygen reduction activity. *ACS nano* **2012**, *6* (8), 7084-7091.
72. Fellingner, T.-P., Sol-gel carbons from ionothermal syntheses. *Journal of Sol-Gel Science and Technology* **2017**, *81* (1), 52-58.
73. Uchida, M.; Fukuoka, Y.; Sugawara, Y.; Eda, N.; Ohta, A., Effects of microstructure of carbon support in the catalyst layer on the performance of polymer-electrolyte fuel cells. *Journal of the Electrochemical Society* **1996**, *143* (7), 2245.
74. Puziy, A.; Poddubnaya, O.; Socha, R.; Gurgul, J.; Wisniewski, M., XPS and NMR studies of phosphoric acid activated carbons. *Carbon* **2008**, *46* (15), 2113-2123.
75. Puziy, A. M.; Poddubnaya, O. I.; Martínez-Alonso, A.; Suárez-García, F.; Tascón, J. M., Surface chemistry of phosphorus-containing carbons of lignocellulosic origin. *Carbon* **2005**, *43* (14), 2857-2868.
76. Hench, L. L.; West, J. K., The sol-gel process. *Chemical reviews* **1990**, *90* (1), 33-72.
77. Pekala, R., Organic aerogels from the polycondensation of resorcinol with formaldehyde. *Journal of materials science* **1989**, *24* (9), 3221-3227.
78. Liu, Y.; Ji, C.; Gu, W.; Jorne, J.; Gasteiger, H. A., Effects of catalyst carbon support on proton conduction and cathode performance in PEM fuel cells. *Journal of The Electrochemical Society* **2011**, *158* (6), B614.
79. Zhong, Z.-Y.; Yang, Q.; Li, X.-M.; Luo, K.; Liu, Y.; Zeng, G.-M., Preparation of peanut hull-based activated carbon by microwave-induced phosphoric acid activation and its application in Remazol Brilliant Blue R adsorption. *Industrial Crops and Products* **2012**, *37* (1), 178-185.
80. Girgis, B. S.; Yunis, S. S.; Soliman, A. M., Characteristics of activated carbon from peanut hulls in relation to conditions of preparation. *Materials Letters* **2002**, *57* (1), 164-172.
81. Molina-Sabio, M.; Rodriguez-Reinoso, F.; Caturla, F.; Sellés, M., Porosity in granular carbons activated with phosphoric acid. *Carbon* **1995**, *33* (8), 1105-1113.

-
82. Jagtoyen, M.; Derbyshire, F., Activated carbons from yellow poplar and white oak by H₃PO₄ activation. *Carbon* **1998**, *36* (7-8), 1085-1097.
83. Jagtoyen, M.; Thwaites, M.; Stencel, J.; McEnaney, B.; Derbyshire, F., Adsorbent carbon synthesis from coals by phosphoric acid activation. *Carbon* **1992**, *30* (7), 1089-1096.
84. Solum, M.; Pugmire, R.; Jagtoyen, M.; Derbyshire, F., Evolution of carbon structure in chemically activated wood. *Carbon* **1995**, *33* (9), 1247-1254.
85. Child, R.; Ramanathan, S., Composition of coconut shells. *Journal of the American Chemical Society* **1938**, *60* (6), 1506-1507.
86. Daems, N.; Sheng, X.; Vankelecom, I. F.; Pescarmona, P. P., Metal-free doped carbon materials as electrocatalysts for the oxygen reduction reaction. *Journal of Materials Chemistry A* **2014**, *2* (12), 4085-4110.
87. Zhang, J.; Zhao, Z.; Xia, Z.; Dai, L., A metal-free bifunctional electrocatalyst for oxygen reduction and oxygen evolution reactions. *Nature nanotechnology* **2015**, *10* (5), 444.
88. Liu, Z. W.; Peng, F.; Wang, H. J.; Yu, H.; Zheng, W. X.; Yang, J., Phosphorus-doped graphite layers with high electrocatalytic activity for the O₂ reduction in an alkaline medium. *Angewandte Chemie International Edition* **2011**, *50* (14), 3257-3261.
89. Ioannidou, O.; Zabaniotou, A., Agricultural residues as precursors for activated carbon production—a review. *Renewable and sustainable energy reviews* **2007**, *11* (9), 1966-2005.
90. Koyutürk, B.; Evans, J.; Mulhaupt, H.; Selve, S.; Simke, J. R. J.; Wark, M.; Fellinger, T.-P., Sol-gel chemistry in molten Brønsted acids towards “activated” carbons and beyond. *Nanoscale* **2019**, *11* (27), 13154-13160.
91. Alslaibi, T. M.; Abustan, I.; Ahmad, M. A.; Foul, A. A., A review: production of activated carbon from agricultural byproducts via conventional and microwave heating. *Journal of Chemical Technology & Biotechnology* **2013**, *88* (7), 1183-1190.
92. Li, R.; Wei, Z.; Gou, X., Nitrogen and phosphorus dual-doped graphene/carbon nanosheets as bifunctional electrocatalysts for oxygen reduction and evolution. *Acs Catalysis* **2015**, *5* (7), 4133-4142.
93. Wang, C.; Sun, L.; Zhou, Y.; Wan, P.; Zhang, X.; Qiu, J., P/N co-doped microporous carbons from H₃PO₄-doped polyaniline by in situ activation for supercapacitors. *Carbon* **2013**, *59*, 537-546.

-
94. Zagal, J. H.; Bedioui, F.; Dodelet, J.-P., *N4-macrocyclic metal complexes*. Springer Science & Business Media: 2007.
95. Gouterman, M.; Sayer, P.; Shankland, E.; Smith, J. P., Porphyrins. 41. Phosphorus mesoporphyrin and phthalocyanine. *Inorganic Chemistry* **1981**, *20* (1), 87-92.
96. Ropp, R. C., *Encyclopedia of the alkaline earth compounds*. Newnes: 2012.
97. Kobayashi, R.; Ishii, T.; Imashiro, Y.; Ozaki, J.-i., Synthesis of P- and N-doped carbon catalysts for the oxygen reduction reaction via controlled phosphoric acid treatment of folic acid. *Beilstein journal of nanotechnology* **2019**, *10* (1), 1497-1510.
98. Wang, L.; Yang, R. T., Significantly increased CO₂ adsorption performance of nanostructured templated carbon by tuning surface area and nitrogen doping. *The Journal of Physical Chemistry C* **2011**, *116* (1), 1099-1106.
99. Wickramaratne, N. P.; Xu, J.; Wang, M.; Zhu, L.; Dai, L.; Jaroniec, M., Nitrogen enriched porous carbon spheres: attractive materials for supercapacitor electrodes and CO₂ adsorption. *Chemistry of Materials* **2014**, *26* (9), 2820-2828.
100. Sevilla, M.; Valle-Vigón, P.; Fuertes, A. B., N-doped polypyrrole-based porous carbons for CO₂ capture. *Advanced Functional Materials* **2011**, *21* (14), 2781-2787.
101. Ferrari, A. C.; Robertson, J., Interpretation of Raman spectra of disordered and amorphous carbon. *Physical review B* **2000**, *61* (20), 14095.
102. Zickler, G. A.; Smarsly, B.; Gierlinger, N.; Peterlik, H.; Paris, O., A reconsideration of the relationship between the crystallite size L_a of carbons determined by X-ray diffraction and Raman spectroscopy. *Carbon* **2006**, *44* (15), 3239-3246.
103. Gorgulho, H. F.; Gonçalves, F.; Pereira, M. F. R.; Figueiredo, J. L., Synthesis and characterization of nitrogen-doped carbon xerogels. *Carbon* **2009**, *47* (8), 2032-2039.
104. Artyushkova, K.; Kiefer, B.; Halevi, B.; Knop-Gericke, A.; Schlogl, R.; Atanassov, P., Density functional theory calculations of XPS binding energy shift for nitrogen-containing graphene-like structures. *Chemical Communications* **2013**, *49* (25), 2539-2541.
105. Maldonado, S.; Morin, S.; Stevenson, K. J., Structure, composition, and chemical reactivity of carbon nanotubes by selective nitrogen doping. *Carbon* **2006**, *44* (8), 1429-1437.
106. Paraknowitsch, J. P.; Zhang, Y.; Wienert, B.; Thomas, A., Nitrogen- and phosphorus-co-doped carbons with tunable enhanced surface areas promoted by the doping additives. *Chemical Communications* **2013**, *49* (12), 1208-1210.

107. Gu, H.; Gu, Y.; Li, Z.; Ying, Y.; Qian, Y., Low-temperature route to nanoscale P3N5 hollow spheres. *Journal of Materials Research* **2011**, *18* (10), 2359-2363.
108. Breusova, M.; Pushkarev, V.; Tomilova, L., Synthesis of alkyl-substituted phosphorus phthalocyanines and triazatetrabenzocorroles. *Russian Chemical Bulletin* **2007**, *56* (7), 1456-1460.
109. Yang, X.; Xia, D.; Kang, Y.; Du, H.; Kang, F.; Gan, L.; Li, J., Unveiling the Axial Hydroxyl Ligand on Fe-N₄-C Electrocatalysts and Its Impact on the pH-Dependent Oxygen Reduction Activities and Poisoning Kinetics. *Advanced Science* **2020**, 2000176.
110. Wang, Y.; Tang, Y.-J.; Zhou, K., Self-Adjusting Activity Induced by Intrinsic Reaction Intermediate in Fe-N-C Single-Atom Catalysts. *Journal of the American Chemical Society* **2019**, *141* (36), 14115-14119.
111. Yang, D.-S.; Bhattacharjya, D.; Inamdar, S.; Park, J.; Yu, J.-S., Phosphorus-Doped Ordered Mesoporous Carbons with Different Lengths as Efficient Metal-Free Electrocatalysts for Oxygen Reduction Reaction in Alkaline Media. *Journal of the American Chemical Society* **2012**, *134* (39), 16127-16130.
112. Wu, J.; Yang, Z.; Li, X.; Sun, Q.; Jin, C.; Strasser, P.; Yang, R., Phosphorus-doped porous carbons as efficient electrocatalysts for oxygen reduction. *Journal of Materials Chemistry A* **2013**, *1* (34), 9889-9896.
113. Zhang, Y.; Huang, N.; Qiao, S.; Zhang, J.; Gao, Z.; Qiu, Z.; Zhou, S.; Jiang, X., Research on phosphorus-doped nano-carbon as ORR catalysts in alkaline electrolyte. *Modern Physics Letters B* **2019**, *33* (05), 1950046.
114. Borghei, M.; Laocharoen, N.; Kibena-Pöldsepp, E.; Johansson, L.-S.; Campbell, J.; Kauppinen, E.; Tammeveski, K.; Rojas, O. J., Porous N,P-doped carbon from coconut shells with high electrocatalytic activity for oxygen reduction: Alternative to Pt-C for alkaline fuel cells. *Applied Catalysis B: Environmental* **2017**, *204*, 394-402.
115. Masa, J.; Zhao, A.; Xia, W.; Sun, Z.; Mei, B.; Muhler, M.; Schuhmann, W., Trace metal residues promote the activity of supposedly metal-free nitrogen-modified carbon catalysts for the oxygen reduction reaction. *Electrochemistry Communications* **2013**, *34*, 113-116.
116. Masa, J.; Xia, W.; Muhler, M.; Schuhmann, W., On the Role of Metals in Nitrogen-Doped Carbon Electrocatalysts for Oxygen Reduction. *Angewandte Chemie International Edition* **2015**, *54* (35), 10102-10120.

117. Jaouen, F.; Dodelet, J.-P., Non-noble electrocatalysts for O₂ reduction: how does heat treatment affect their activity and structure? Part I. Model for carbon black gasification by NH₃: parametric calibration and electrochemical validation. *The Journal of Physical Chemistry C* **2007**, *111* (16), 5963-5970.
118. Ott, S.; Orfanidi, A.; Schmies, H.; Anke, B.; Nong, H. N.; Hübner, J.; Gernert, U.; Gliech, M.; Lerch, M.; Strasser, P., Ionomer distribution control in porous carbon-supported catalyst layers for high-power and low Pt-loaded proton exchange membrane fuel cells. *Nature Materials* **2020**, *19* (1), 77-85.
119. Orfanidi, A.; Madkikar, P.; El-Sayed, H.; Harzer, G.; Kratky, T.; Gasteiger, H., The key to high performance low Pt loaded electrodes. *Journal of The Electrochemical Society* **2017**, *164* (4), F418.
120. Eisenberg, D.; Stroek, W.; Geels, N. J.; Tanase, S.; Ferbinteanu, M.; Teat, S. J.; Mettraux, P.; Yan, N.; Rothenberg, G., A rational synthesis of hierarchically porous, N-doped carbon from Mg-based MOFs: understanding the link between nitrogen content and oxygen reduction electrocatalysis. *Physical Chemistry Chemical Physics* **2016**, *18* (30), 20778-20783.
121. Brunauer, S.; Emmett, P. H.; Teller, E., Adsorption of gases in multimolecular layers. *Journal of the American chemical society* **1938**, *60* (2), 309-319.
122. Li, J.; Jiao, L.; Wegener, E.; Richard, L. L.; Liu, E.; Zitolo, A.; Sougrati, M. T.; Mukerjee, S.; Zhao, Z.; Huang, Y., The evolution pathway from iron compounds to Fe^I (II)-N₄ sites through gas-phase iron during pyrolysis. *Journal of the American Chemical Society* **2019**.
123. Ratso, S.; Sougrati, M. T.; Käärik, M.; Merisalu, M.; Rähn, M.; Kisand, V.; Kikas, A.; Paiste, P. a. r.; Leis, J.; Sammelselg, V. i., Effect of Ball-Milling on the Oxygen Reduction Reaction Activity of Iron and Nitrogen Co-doped Carbide-Derived Carbon Catalysts in Acid Media. *ACS Applied Energy Materials* **2019**, *2* (11), 7952-7962.
124. Zitolo, A.; Goellner, V.; Armel, V.; Sougrati, M.-T.; Mineva, T.; Stievano, L.; Fonda, E.; Jaouen, F., Identification of catalytic sites for oxygen reduction in iron-and nitrogen-doped graphene materials. *Nature materials* **2015**, *14* (9), 937-942.
125. Choi, C. H.; Choi, W. S.; Kasian, O.; Mechler, A. K.; Sougrati, M. T.; Brüller, S.; Strickland, K.; Jia, Q.; Mukerjee, S.; Mayrhofer, K. J., Unraveling the Nature of Sites Active

toward Hydrogen Peroxide Reduction in Fe-N-C Catalysts. *Angewandte Chemie International Edition* **2017**, *56* (30), 8809-8812.

126. Goellner, V.; Armel, V.; Zitolo, A.; Fonda, E.; Jaouen, F., Degradation by hydrogen peroxide of metal-nitrogen-carbon catalysts for oxygen reduction. *Journal of the electrochemical society* **2015**, *162* (6), H403-H414.

Appendix

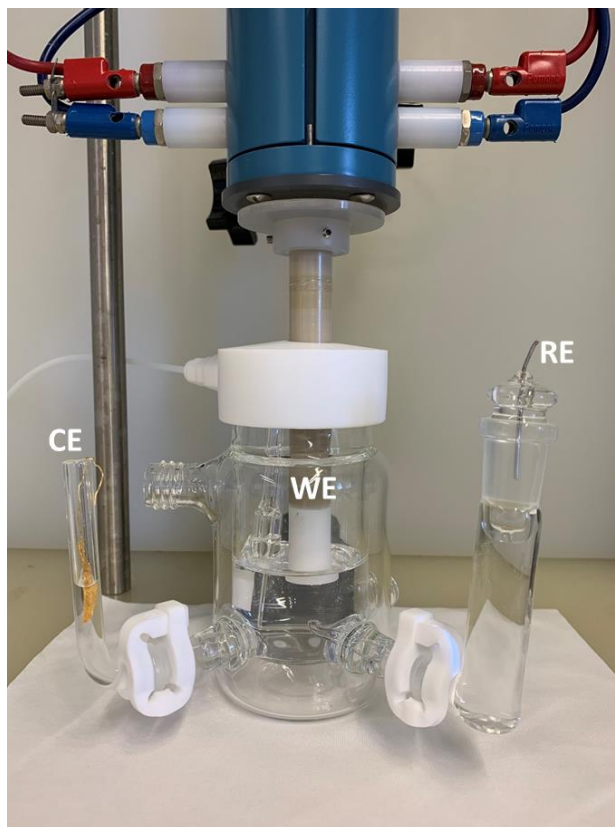


Figure 1.1.1: An example of RDE setup with components for acidic medium.

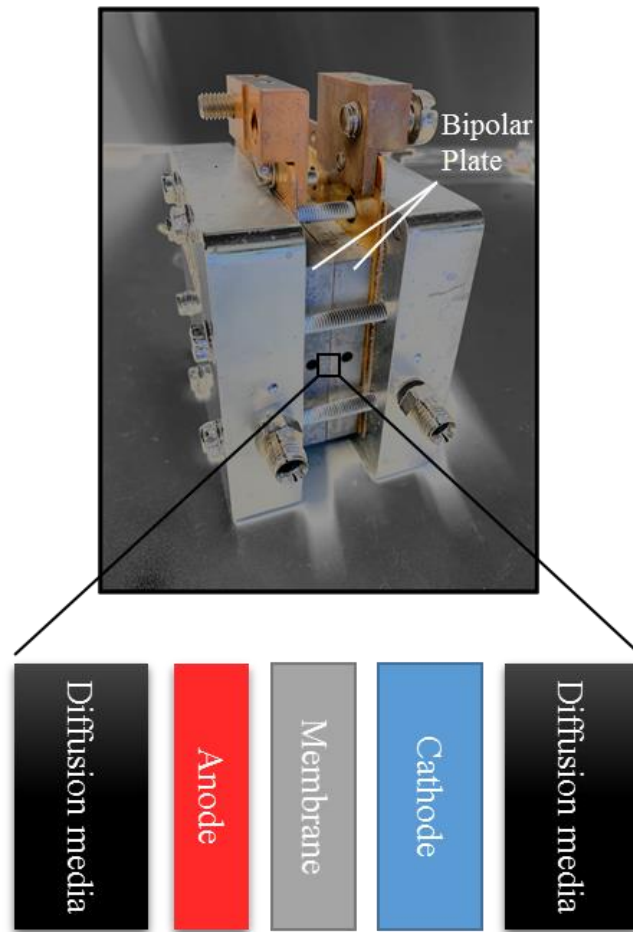


Figure 1.1.2: Illustration of a fuel cell stack.

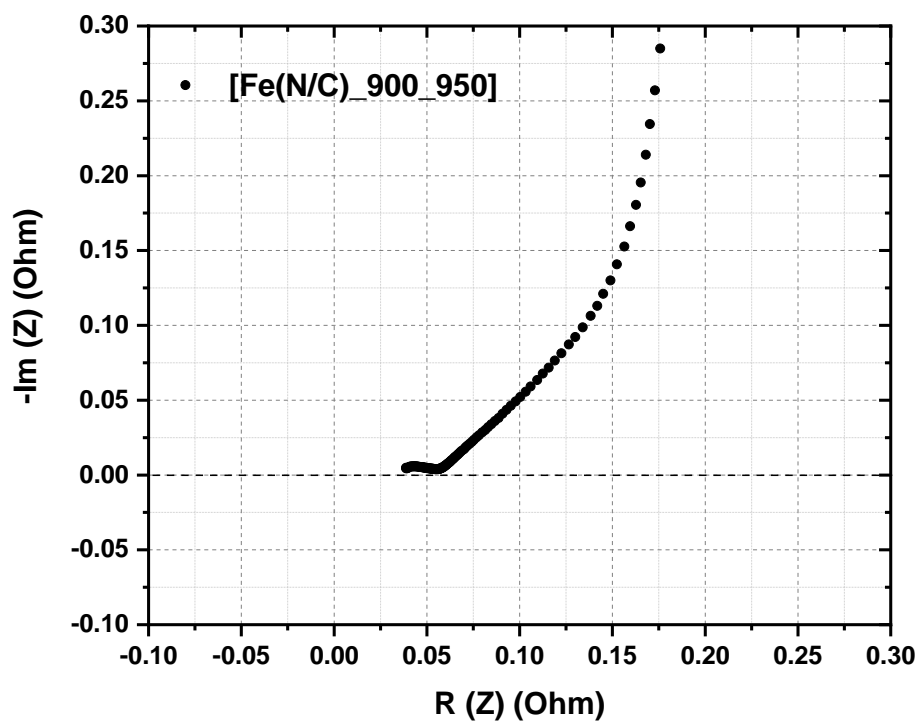


Figure S1.1.3: Nyquist plot for proton sheet resistance.

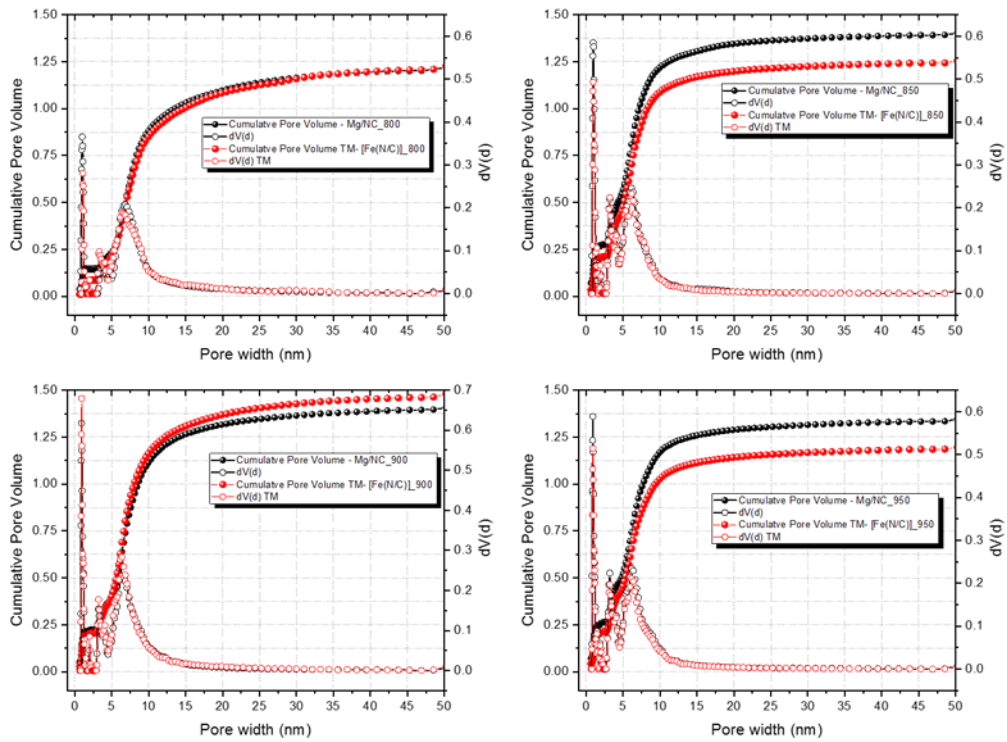


Figure S2.2.1: PSD of the samples in the range of 0-50 nm; a) 800 °C, b) 850 °C, c) 900 °C, d) 950 °C.

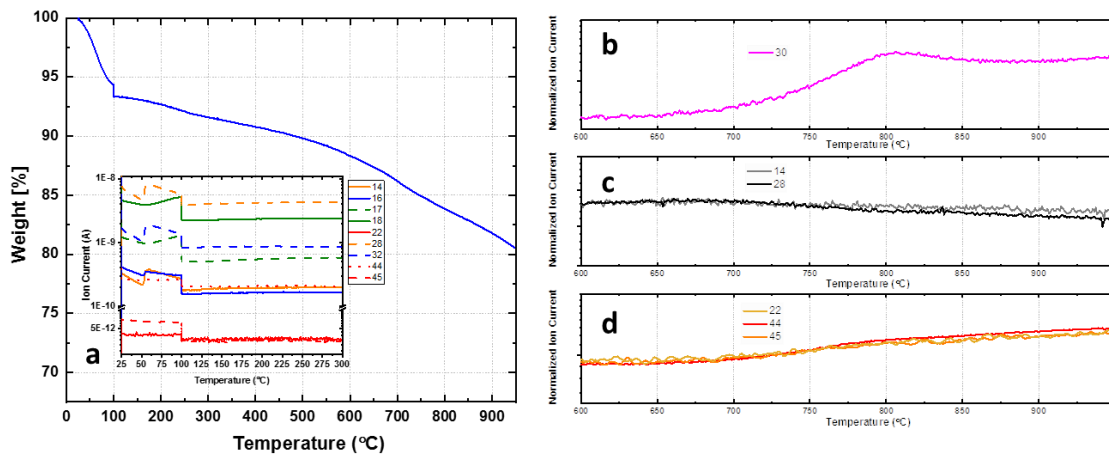


Figure S2.2.2: TG-MS signals of heat-treated Mg/NC₈₀₀.

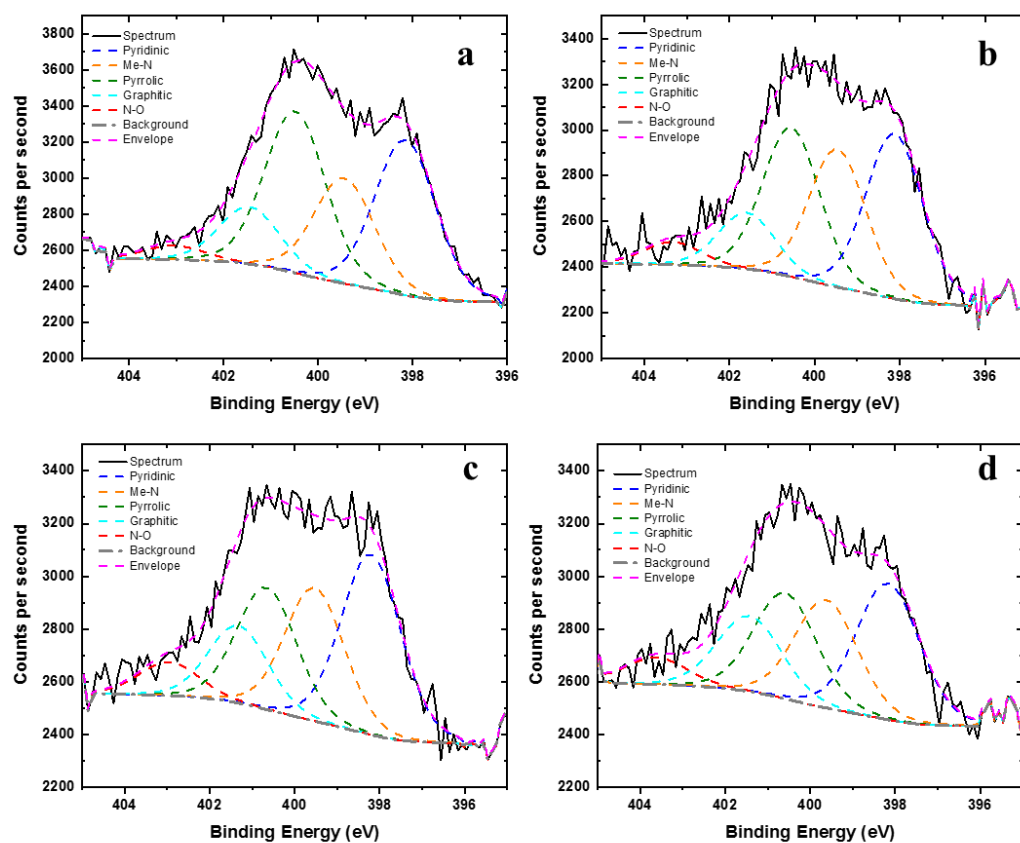


Figure S2.2.3: N1s spectra of the transmetallated samples; a) [Fe(N/C_800)], b) [Fe(N/C_850)], c) [Fe(N/C_900)], d) [Fe(N/C_950)].

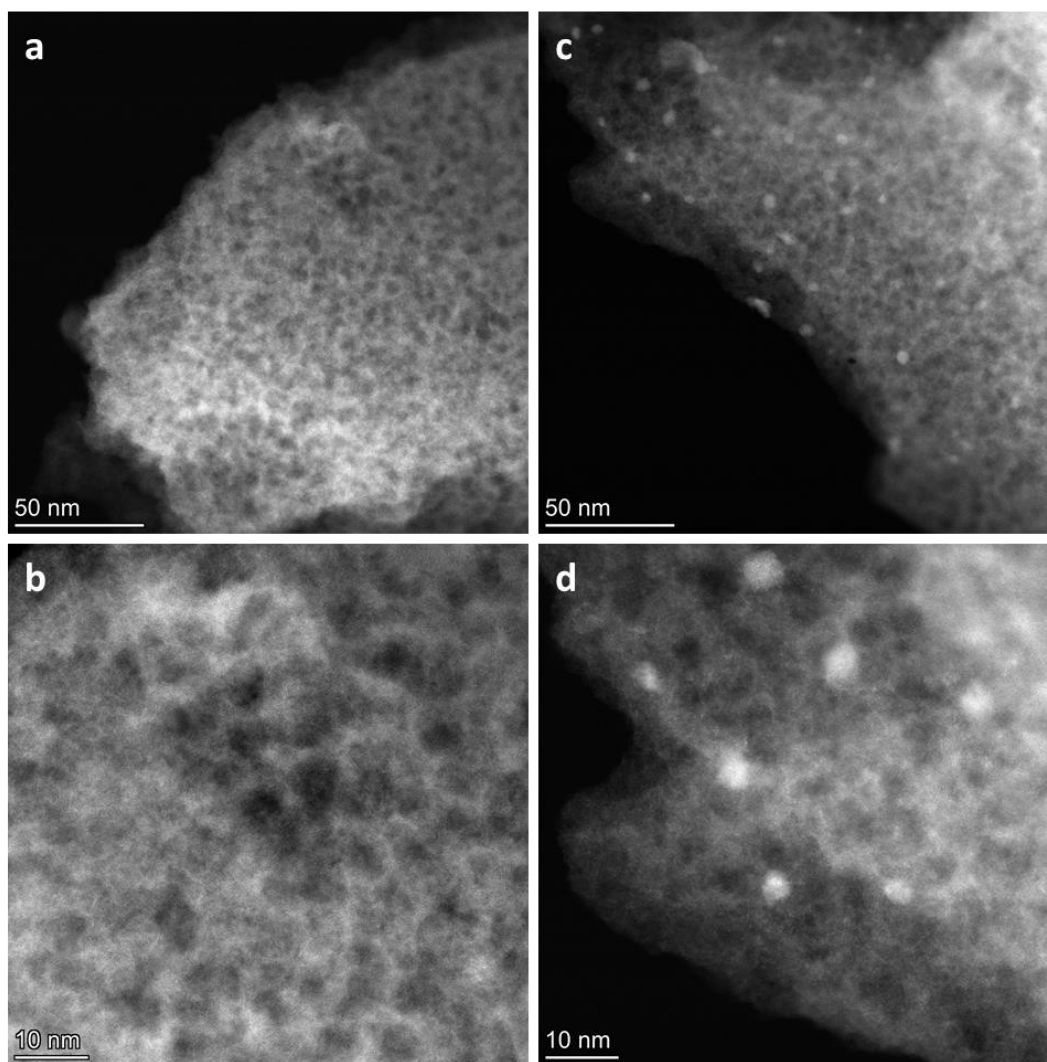


Figure S2.2.4: TEM images of a, b) Mg/NC; c,d) [Fe(N/C)].

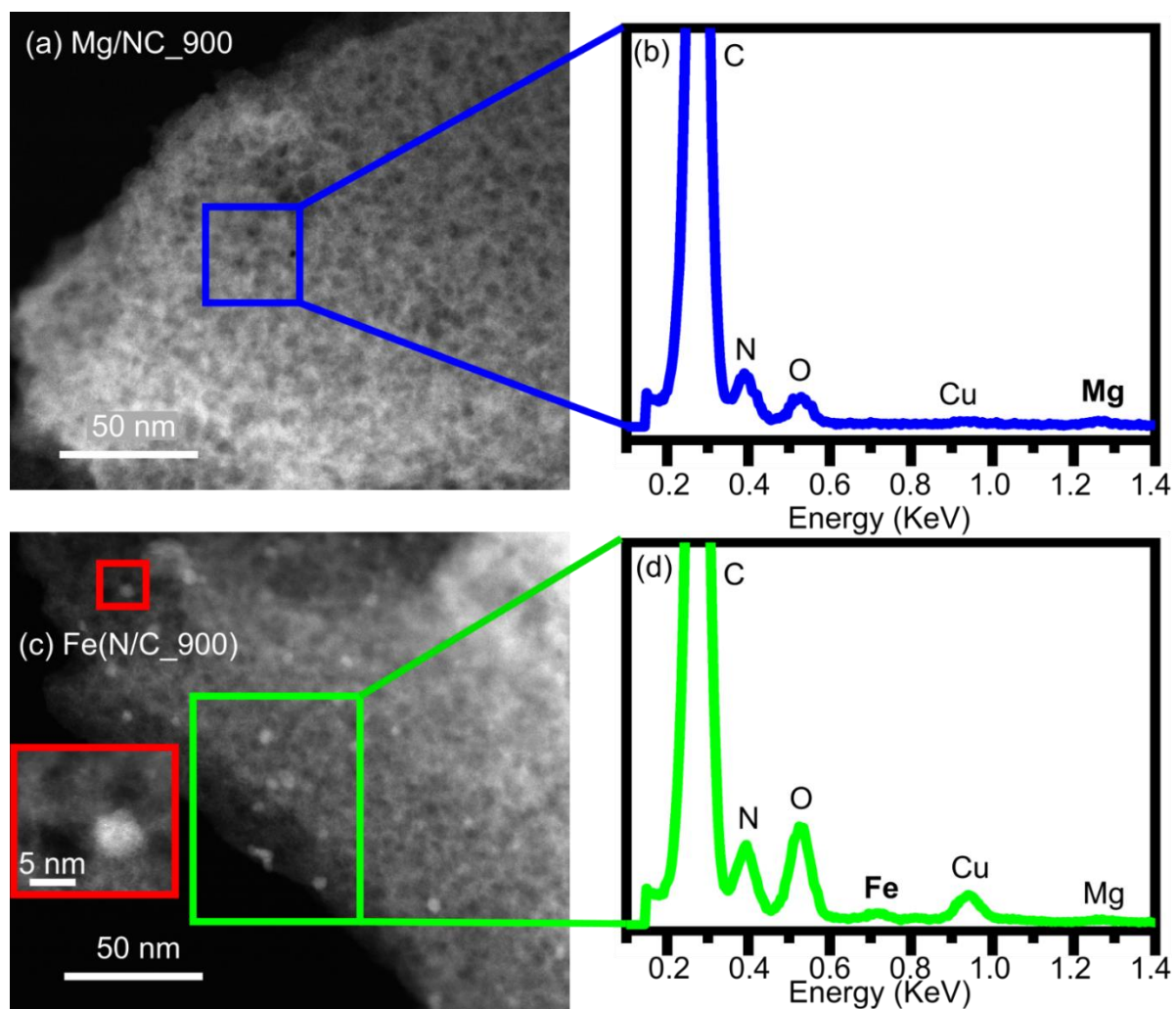


Figure S2.2.5: (a) HAADF micrograph of Mg/NC₉₀₀, (b) STEM-EDX of Mg/NC₉₀₀, (c) HAADF micrograph of Fe(NC₉₀₀), (d) STEM-EDX of Fe(NC₉₀₀).

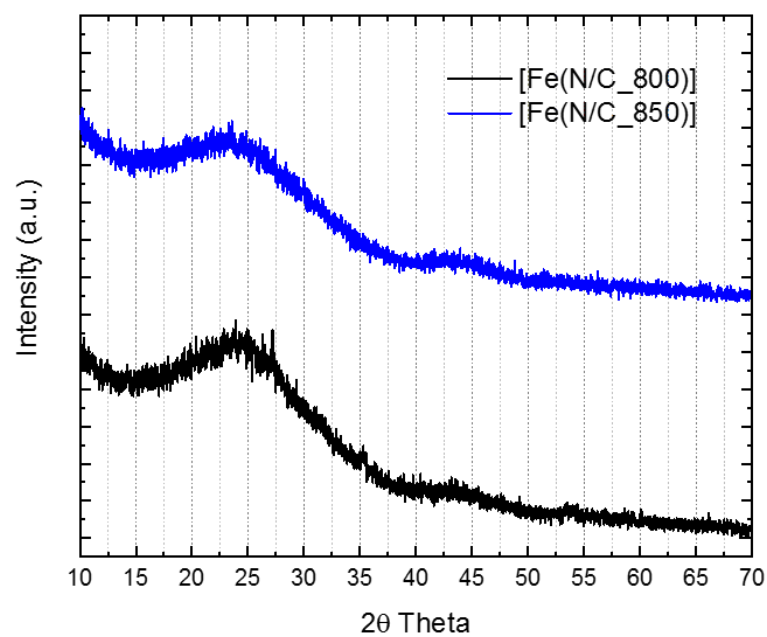


Figure S2.2.6: PXRD patterns of [Fe(NC_800)] and [Fe(NC_850)].

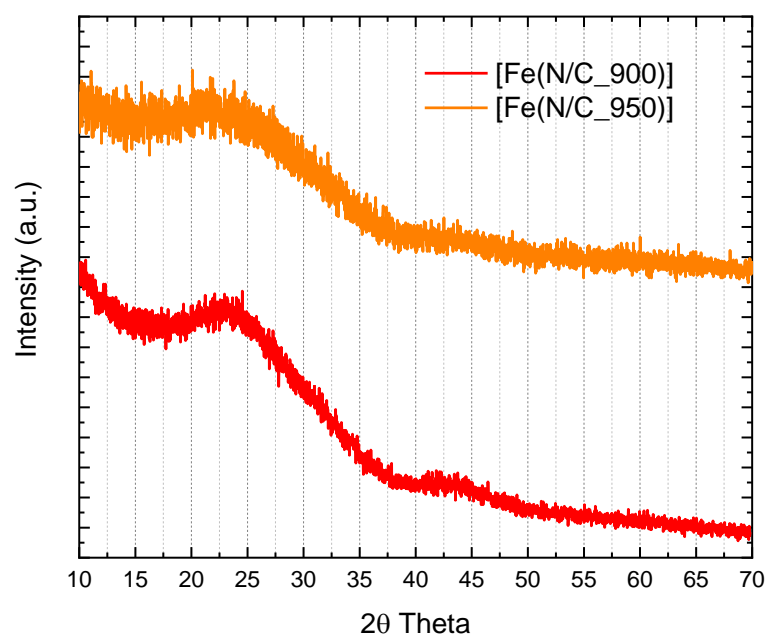


Figure S2.2.7: PXRD patterns of [Fe(NC_900)] and [Fe(NC_950)].

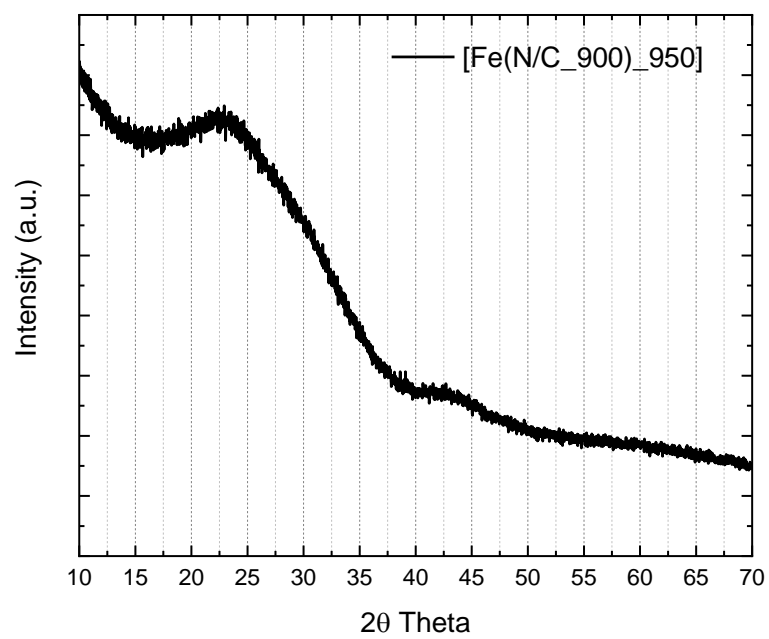


Figure S2.2.8: PXRD patterns of [Fe(NC_900_950)].

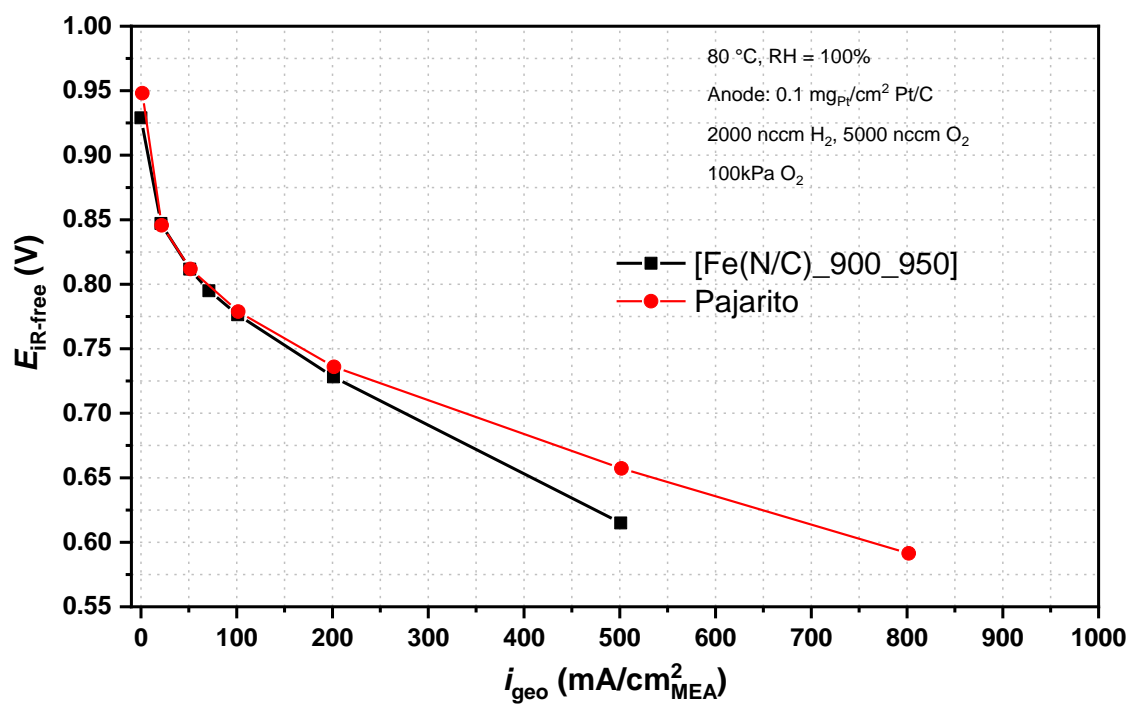


Figure S2.2.9: Comparison of polarization curves of [Fe(NC_900_950)] and Pajarito Powder acquired in fuel cell test station.

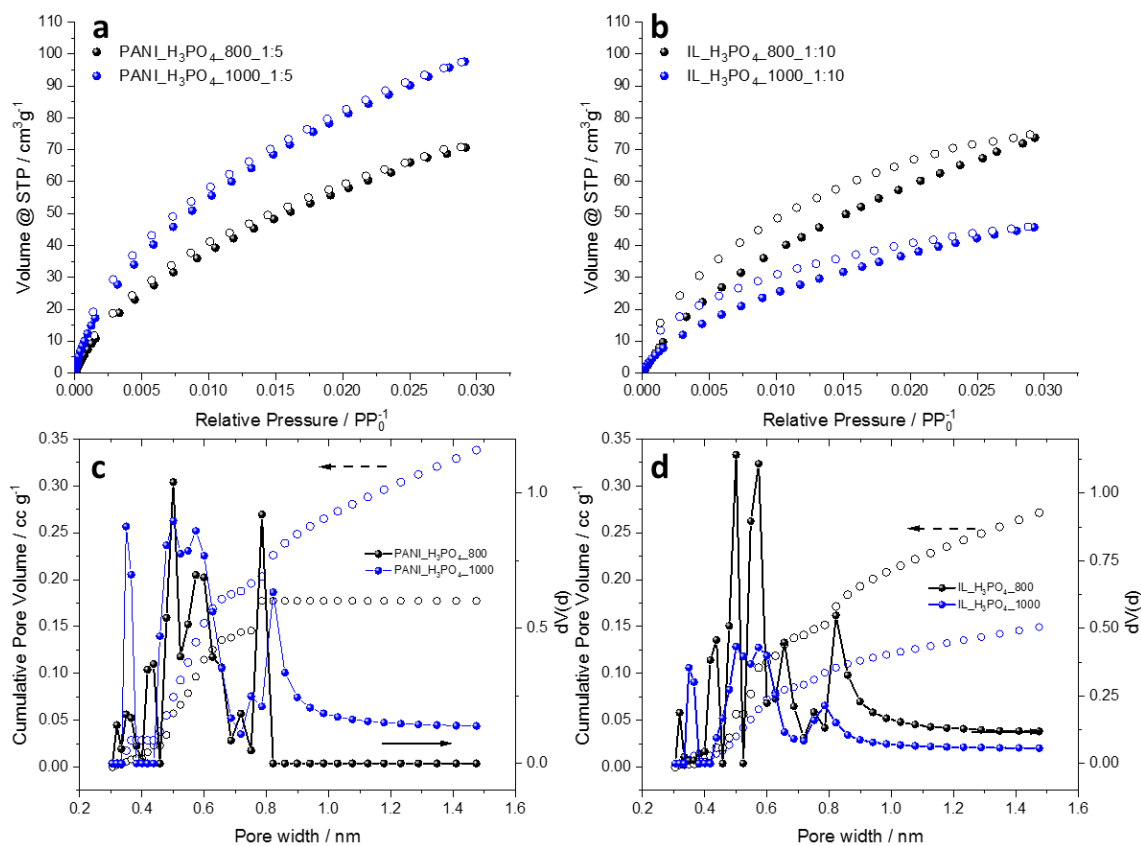


Figure S3.2.1: CO₂ sorption isotherms as well as pore size distributions and cumulative pore volume plots of PANI (a, c) and IL derived carbons (b, d).

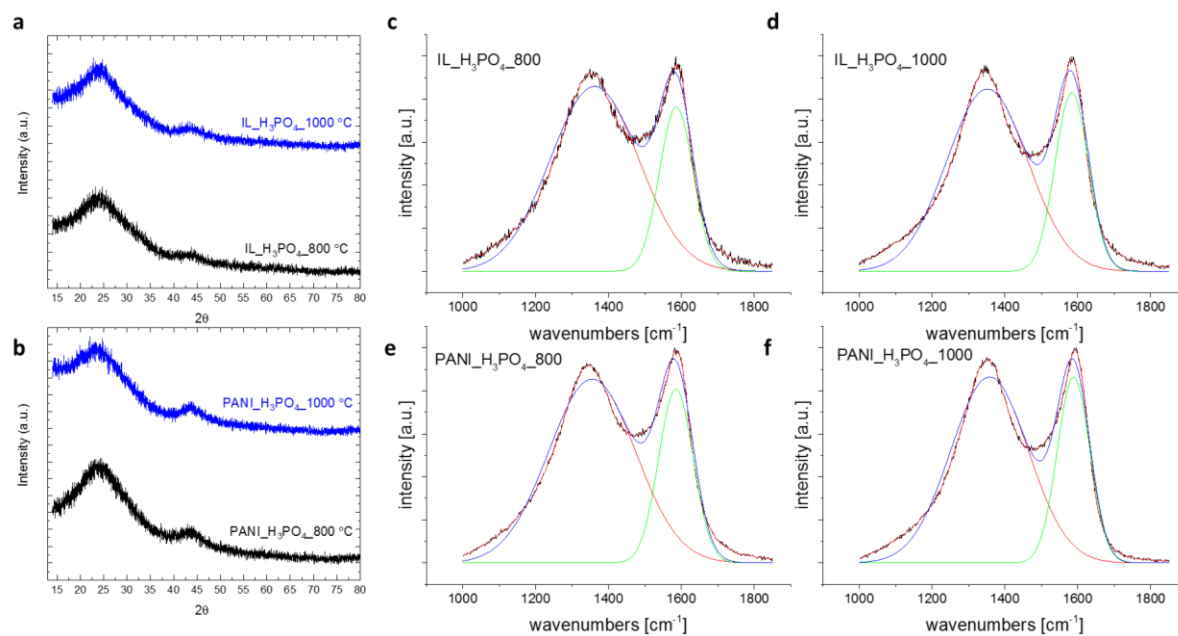


Figure S3.2.2: PXRD patterns of a) IL_H₃PO₄, b) PANI_H₃PO₄ samples and Raman spectra of c) IL_H₃PO₄_800°C, d) IL_H₃PO₄_1000°C e) PANI_H₃PO₄_800°C, and f) PANI_H₃PO₄_1000°C.

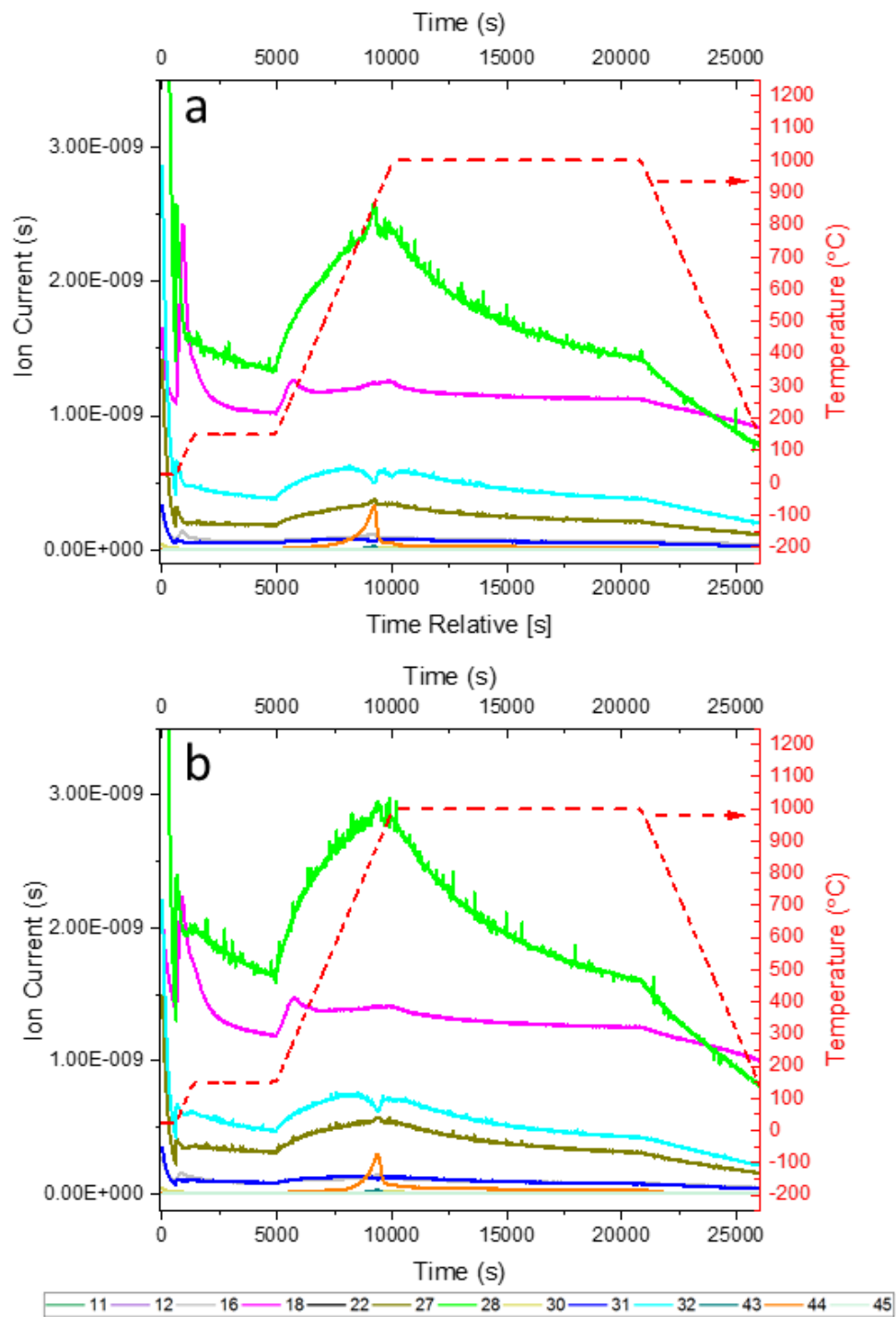


Figure S3.2.3: TG-MS profile of the samples; a) PANI_H₃PO₄_800, b) IL_H₃PO₄_800.

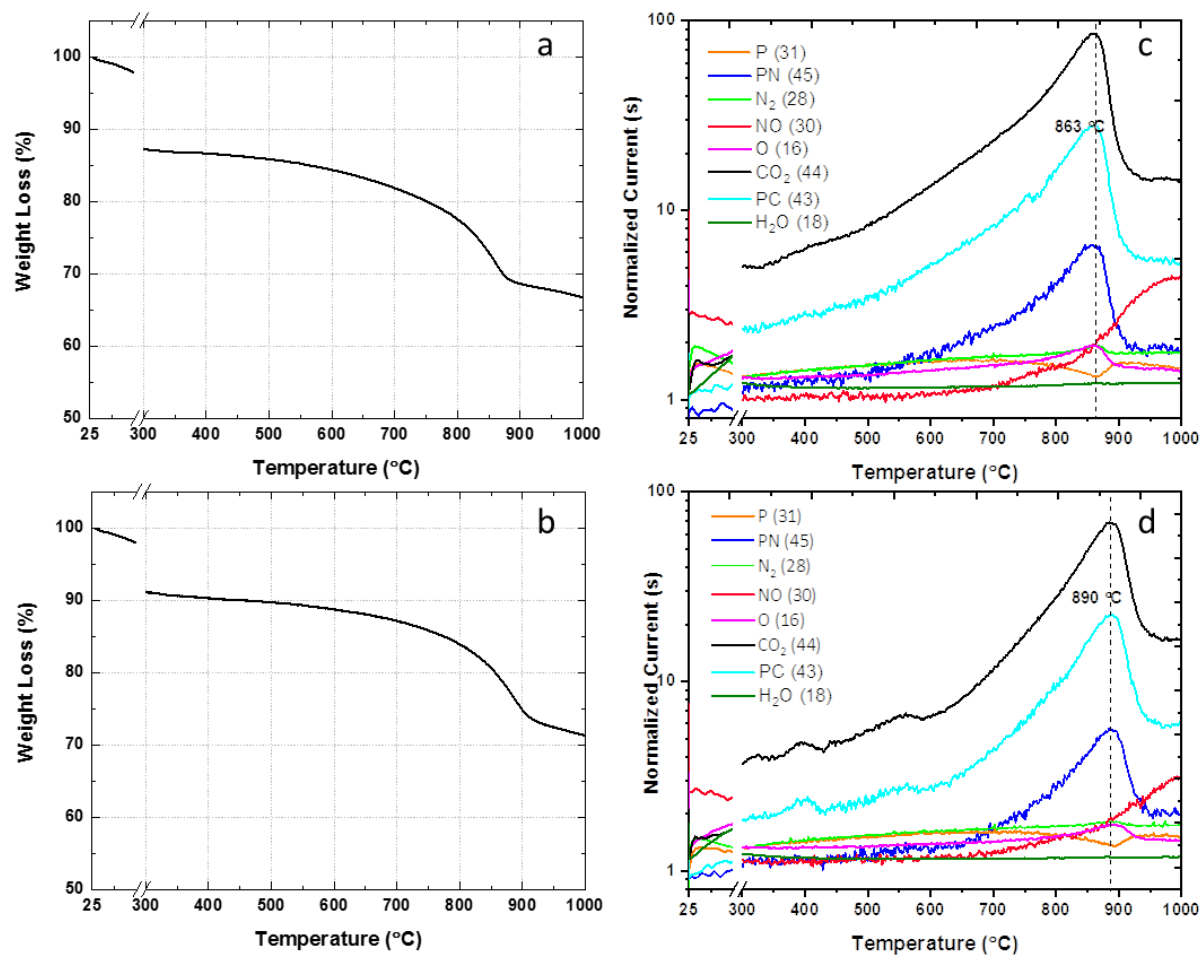


Figure 3.2.4: TG-MS data of: a,c) PANI_H₃PO₄_800°C, b,d) IL_H₃PO₄_800°C.

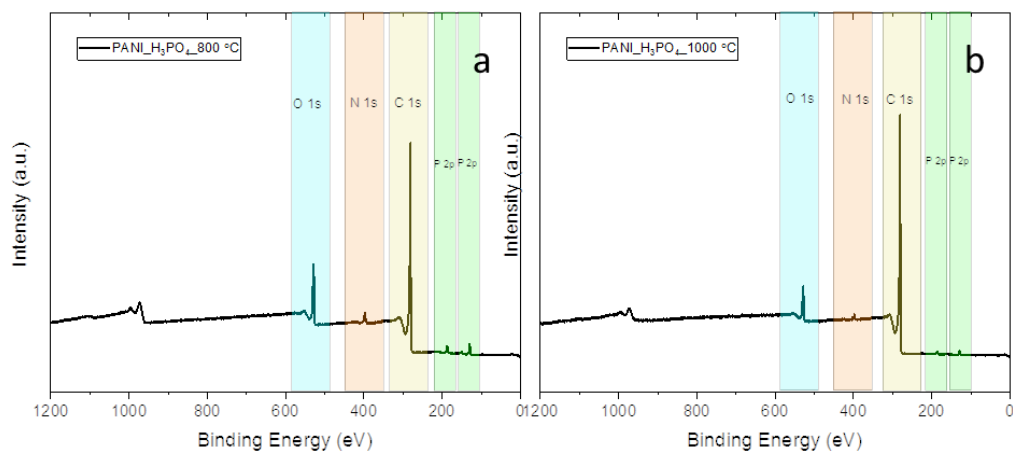


Figure S3.2.5: XPS Survey spectra of a) PANI_H₃PO₄_800°C, b) PANI_H₃PO₄_1000°C.

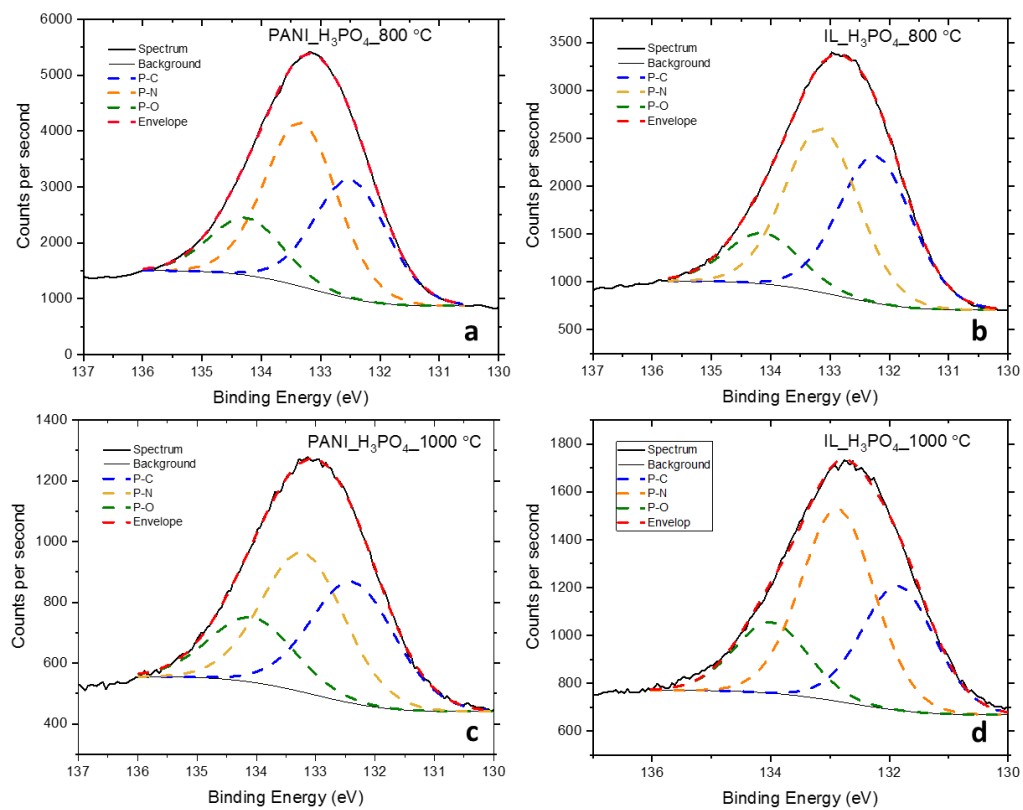


Figure S3.2.6: Deconvoluted P2p XPS spectra of a) PANI_H₃PO₄_800 b) IL_H₃PO₄_800 c) PANI_H₃PO₄_1000 and d) IL_H₃PO₄_1000.

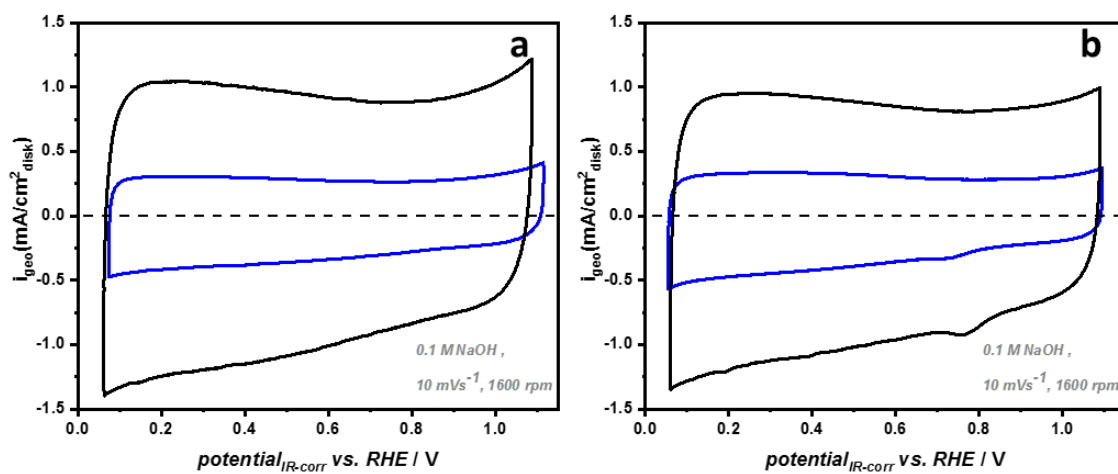


Figure S3.2.7: CVs measured at a sweep rate of 10mV s^{-1} ; a) PANI_H₃PO₄_1000 and b) IL_H₃PO₄_1000.

Table S2.2.1: Mössbauer fitting parameters for each component.

Assignment	Quadrupole Splitting (QS, mm/s)	Isomer Shift (IS, mm/s)	Hyperfine Field (HF, Tesla)	Relative Area (RA, %)
D1	1.184	0.211		0.429
D2	3.726	0.700		0.116
Sextet		0.224	47.599	0.455

Table S2.2.2: D1 relative content in literature.

D1 %	T (K)	Reference
62	5	Evolution Pathway from Iron Compounds to Fe1(II)-N4 Sites through Gas-Phase Iron during Pyrolysis ¹²²
42.9	4.2	This work
37.1	4.2	Active-Site Imprinting: Preparation of Fe-N-C Catalysts from Zinc Ion-Templated Ionothermal Nitrogen-Doped Carbons ²⁰
68.1	298	Effect of Ball-Milling on the Oxygen Reduction Reaction Activity of Iron and Nitrogen Co-doped Carbide-Derived Carbon Catalysts in Acid Media ¹²³
58	298	Identification of catalytic sites for oxygen reduction in iron- and nitrogen-doped graphene materials ¹²⁴
58	298	Fe-N-C electrocatalyst with dense active sites and efficient mass transport for high-performance proton exchange membrane fuel cells ⁴⁵
58	298	Unraveling the Nature of Sites Active toward Hydrogen Peroxide Reduction in Fe-N-C Catalysts ¹²⁵
53	298	Degradation by Hydrogen Peroxide of Metal-Nitrogen-Carbon Catalysts for Oxygen Reduction ¹²⁶

Table S2.2.3: Comparison of the mass activities of FeNC catalysts.

Catalyst	Im (A/g)@0.8 v
[Fe(N/C_900)]	0.95
[Fe(N/C_900_950)]	1.4
Pajarito	1.3-2.0

Table S3.2.1: Elemental composition and yield of the synthesized carbons.

Sample	C	H	N	N/C	Total Yield
Coconut	47.88	6.10	-	-	-
Glucose (theo.)	40.00	0.06	-	-	-
EMIM DCA (theo.)	54.00	0.06	0.40	0.01	-
PANI	72.68	5.26	14.62	0.20	-
Glu-H₃PO₄ 1-1	62.18	2.14	-	-	32.4
Glu-H₃PO₄ 1-5	63.80	1.64	-	-	27.3
Glu-H₃BO₃ 1-1	89.72	2,15	-	-	24.1
Glu-H₃BO₃ 1-5	89.24	1.88	-	-	27.4
IL-H₃PO₄ 1-1	24.23	2.85	8.49	0.35	-
IL-H₃PO₄ 1-5	24.89	1.46	3.97	0.16	-
Coco-H₃PO₄ 1-1	67.20	2.15	0.17	-	28.5
Coco-H₃PO₄ 1-2.5	72.45	1.41	0.22	-	-
Coco-H₃PO₄ 1-5	62.53	1.81	0.21	-	38.1
Coco_ H₃BO₃ 1-1	90.22	1.99	0.24	-	-
Coco-H₃BO₃ 1-5	87.13	1.99	0.26	-	32
PANI-H₃PO₄ 1-1	42.99	1.85	6.22	0.14	57
PANI-H₃PO₄ 1-5	48.22	1.66	5.20	0.11	76
Coco-borax_ H₃BO₃ 1-1	84.49	2.22	0.22	-	19.8
Coco-borax_ H₃BO₃ 1-5	86.53	2.25	0.23	-	27.5

**PERSONAL
INFORMATION****BURAK KOYUTÜRK**

Berzeliusstrasse 3, 80939, Garching, Munich

+905395888144, +49 17661280529

burak.koyutuerk@tum.de

**WORK
EXPERIENCE**

Jan 2015–Feb
2015

Internship

Seranit Granit Seramik San. Tic. A.Ş., Istanbul (Turkey)

Aug 2013–Sep
2013

Internship

Mustafa Nevzat Pharmaceuticals, Istanbul (Turkey)

**EDUCATION AND
TRAINING**

Sep 2020–June
2020

Visiting Scholar

Los Alamos National Laboratory (US)

Sep 2017–
present

PhD in Chemistry

Technical University of Munich (Germany)

Sep 2015–July
2017

MSc in Chemical and Biological Engineering

Koç University, Istanbul (Turkey)

Teaching and Research Assistant at Chemical and Biological Engineering

GPA: 3.28 / 4.00

Sep 2012–Jun
2013

Exchange Student

Bmo University of Technology, Brno (Czech Republic)

Aug 2010–Jul
2015

BSc in Chemical Engineering

Yildiz Technical Engineering, Istanbul (Turkey)

GPA: 3.34 / 4.00

PERSONAL SKILLS

Job-related skills

Command of instrument:

- Ft-IR

- Gas sorption (Kr, N₂, Ar, CO₂)
- XPS
- XRD
- SEM

ADDITIONAL INFORMATION

Scholarships

- The Scientific and Technological Research Council of Turkey (TUBITAK) Scholarship
September, 2015 –2017
- Koç University Scholarship
September, 2015 – 2017

Conferences

- **Electrolysis and Fuel Cell Discussions (EFCD), La Grande Motte, France**
September 15-18, 2019
Poster presentation: "PGM-Free Cathode Catalyst Layer Loading Impact on Mass Activity in PEMFC"
- **31. Deutsche Zeolith-Tagung**
March 6-8, 2019
Poster presentation: "Sol-Gel Chemistry in Molten Brønsted Acids: Towards Activated Carbon Electrocatalysts"
- **American Institute of Chemical Engineers (AIChE) Annual Meeting San Francisco, CA**
November 13-18, 2016
Oral presentation: "Consequences of 1-Butyl-3-Methylimidazolium Tetrafluoroborate Incorporation on Gas Separation Performance of ZIF-8"
- **12th Nanoscience and Nanotechnology Conference (NanoTR-12) Kocaeli, Turkey**
June 3-5, 2016
Oral presentation: "Investigation of gas uptake and selectivity of ionic liquid incorporated Cu-BTC"

Publications

- Kinik, F. P., Altintas, C., Balci, V., Koyutürk, B., Uzun, A., & Keskin, S. (2016). [BMIM][PF₆] incorporation doubles CO₂ selectivity of ZIF-8: elucidation of interactions and their consequences on performance. *ACS applied materials & interfaces*, 8(45), 30992-31005.
- Koyutürk, B., Altintas, C., Kinik, F. P., Keskin, S., & Uzun, A. (2017). Improving gas separation performance of ZIF-8 by [BMIM][BF₄] incorporation: Interactions and their consequences on performance. *The Journal of Physical Chemistry C*, 121(19), 10370-10381.
- Koyutürk, B., Evan, J., Mulhaupt, H., Selve, S., Simke, J. R. J., Wark, M., & Fellerger, T. P. (2019). Sol-Gel Chemistry in Molten Brønsted Acids towards "Activated" Carbons and Beyond. *Nanoscale*.
- Menga, D., Ruiz-Zepeda, F., Moriau, L., Šala, M., Wagner, F., Koyutürk, B., ... & Fellerger, T. P. (2019). Active-Site Imprinting: Preparation of Fe–N–C Catalysts from Zinc Ion–Templated Ionothermal Nitrogen-Doped Carbons. *Advanced Energy Materials*, 1902412.

Mehmood, A., Ali, G., Koyutürk, B., Pampel, J., Chung, K. Y., & Fellingner, T. P. (2020). Ion-Sieving Nanoporous Nitrogen Doped Carbons with Enhanced Capacity for Sodium Ion Battery Anodes. *Energy Storage Materials*.

Loading Impact of a PGM-Free Cathode Catalyst on the Mass Activity (in preparation)

Porous Nitrogen and Phosphorus Doped Carbon Electrocatalysts by a High Temperature H₃PO₄ Activation Process (submitted)

I hereby declare that the dissertation titled

Towards the Scalable Synthesis of PGM-free Catalysts for Oxygen Reduction Reaction

prepared under the guidance and supervision of Dr. Tim-Patrick Fellingner

in Chair of Technical Electrochemistry at Department of Chemistry

and submitted to the responsible department of TUM is my own, original work undertaken in partial fulfillment of the requirements for the doctoral degree. I have made no use of sources, materials or assistance other than those specified in § 6 (6) and (7), clause 2.

(x) I have not employed the services of an organization that provides dissertation supervisors in return for payment or that fulfills, in whole or in part, the obligations incumbent on me in connection with my dissertation.

(x) I have not submitted the dissertation, either in the present or a similar form, as part of another examination process.

() The complete dissertation was published in

The responsible department

.....

has approved prior publication of the dissertation.

() I have not yet been awarded the desired doctoral degree nor have I failed the last possible attempt to obtain the desired degree in a previous doctoral program.

() I have already applied for admission to a doctoral program at the academic department of

at (university).....by submitting a dissertation on the topic..... with the result:.....

I am familiar with the publicly available Regulations for the Award of Doctoral Degrees of TUM, in particular § 28 (Invalidation of doctoral degree) and § 29 (Revocation of doctoral degree). I am aware of the consequences of filing a false affidavit.

(x) I agree

() I do not agree

that my personal data is stored in the TUM alumni database.

Munich, 01.08.2020

Signature